

Universidad Autónoma de Querétaro
Facultad de Ingeniería
Doctorado en Mecatrónica



**Respuesta dinámica de los vehículos ferroviarios derivada del
coeficiente de fricción rueda-riel**

Opción de titulación

Tesis

Que como parte de los requisitos para obtener el título de

Doctor en Mecatrónica

Presenta:

Gerardo Hurtado Hurtado

Dirigido por:

Dr. Juan Carlos Antonio Jáuregui Correa

San Juan del Río, Querétaro, Julio de 2023



Dirección General de Bibliotecas y Servicios Digitales
de Información



Respuesta dinámica de los vehículos ferroviarios
derivada del coeficiente de fricción rueda-riel

por

Gerardo Hurtado Hurtado

se distribuye bajo una [Licencia Creative Commons
Atribución-NoComercial-SinDerivadas 4.0
Internacional](https://creativecommons.org/licenses/by-nc-nd/4.0/).

Clave RI: IGDCC-215404



Universidad Autónoma de Querétaro
Facultad de Ingeniería
Doctorado en Mecatrónica

Respuesta dinámica de los vehículos ferroviarios derivada del coeficiente de fricción rueda-riel

TESIS

Que como parte de los requisitos para obtener el grado de
Doctor en Mecatrónica

Presenta:

M. en C. Gerardo Hurtado Hurtado

Dirigido por:

Dr. Juan Carlos Antonio Jáuregui Correa

SINODALES

Dr. Juan Carlos Antonio Jáuregui Correa
Presidente

Firma

Dr. Luis Morales Velázquez
Secretario

Firma

Dr. Martín Valtierra Rodríguez
Vocal

Firma

Dr. Juan Primo Benítez Rangel
Suplente

Firma

Dr. Frank Otremba
Suplente

Firma

Dr. Manuel Toledano Ayala
Nombre y Firma
Director de la Facultad

Dr. Juan Carlos A. Jáuregui Correa
Nombre y Firma
Director de Investigación y posgrado

Dedication

To my wife and daughter who have been a constant source of support and encouragement during the challenges of graduate school and life. I am truly thankful for having you in my life.

To my parents who have always loved me unconditionally and whose good examples have taught me to work hard for the things that I aspire to achieve.

Acknowledgements

I'd like to express my gratitude to everyone I've had the honor of working with. I am extremely grateful to my advisor, Dr. Juan Carlos Jauregui, for always being supportive of my academic goals and who worked actively to provide me with the protected academic time to pursue my career goals.

Everyone on my dissertation committee has been an invaluable source of advice and encouragement, and I've learned so much from them about myself, my research, and life in general. For providing me with the technical resources I needed to complete this project, I would like to extend my deepest gratitude to Dr. Luis Morales Velázquez and Dr. Frank Otremba. I also would like to express my gratitude to Dr. Martin Valtierra Rodríguez for all the time and effort he put into assisting me in the pursuit of my PhD degree.

This work would not have been possible without the financial support of Consejo Nacional de Ciencia y Tecnología, CONACyT's scholarship 2018-000068-02NACF.

Abstract

The dynamic response of a railroad vehicle is affected by the frictional forces generated at the wheel-rail contact surface. The friction in the wheels consist of tangential collisions with the rail that affect the vehicle dynamics, which can be measured using the vehicle's vibration level. In this study, the vibrations of a scaled-down railway vehicle undertaking a braking maneuver are monitored to determine the coefficient of friction at the wheels. The 1:20-scale rail vehicle is equipped with encoders, accelerometers, and a Bluetooth control. The tests are conducted on both a clean and on a friction-modified railway. To relate the level of vibration measured in each test with high or low coefficients of friction, suitable statistical indices were selected. Furthermore, and using a correlation algorithm based upon the Continuous Wavelet Transform (CWT), it is demonstrated that frictional forces are transmitted to the vehicle body. The output data indicate that the vibrations characteristics depend on the wheels' coefficient of friction, which can be used to classify it as a high or a low friction, and that it is possible to study the tangential forces during braking using the vehicle's vibrations.

Index

Dedication	3
Acknowledgements.....	4
Abstract	5
Index.....	6
Figures index	9
Tables index.....	10
1 Introduction	11
1.1 State of the art	12
1.2 Hypothesis.....	13
1.3 Objectives.....	13
1.3.1 General objective	13
1.3.2 Specific objectives	13
1.4 Statement of the problem.....	13
1.5 Justification	14
1.5.1 Scientific relevance.....	14
1.5.2 Social relevance.....	14
2 Theoretical framework.....	15
2.1 Principal components of a train	15
2.1.1 Wagon and bogies.....	15
2.1.2 Wheelset	16
2.1.3 Rail.....	18
2.2 Wheel-rail interaction	19
2.2.1 Hertz’s contact theory.....	19
2.2.2 Forces in the contact point of a wheelset.....	21
2.2.3 Creep forces	22
2.3 Rolling friction	25
2.3.1 Wheel-rail’s friction model.....	26
2.3.2 Monitoring of the wheel’s tangential forces.....	27
2.3.3 Friction modifiers	28
3 Analytical methods for vibrations	33
3.1 Time domain analysis technics.....	33

3.1.1	Kurtosis.....	33
3.1.2	Root mean square (RMS)	34
3.1.3	Crest factor (CF).....	34
3.1.4	Variance.....	34
3.2	Frequency domain analysis technics.....	34
3.2.1	Empirical Mode Decomposition (EMD).....	34
3.2.2	Fast Fourier transform (FFT).....	37
3.2.3	Continuous wavelet transform (CWT).....	40
3.2.4	Proposed correlation method	41
4	Methodology.....	45
4.1	Test Bench Description.....	45
4.1.1	The scaled-down railway vehicle	45
4.1.2	Test bench	47
4.1.3	Data acquisition system	48
4.2	Methodology.....	52
4.2.1	Experiment overview	52
4.2.2	Braking Experiments.....	55
4.2.3	Vibration analysis	60
5	Results and discussion.....	63
5.1	Time domain analysis.....	63
5.1.1	Vibration responses over time	64
5.1.2	Descriptive statistics of the vibration’s time series.....	68
5.2	Frequency domain analysis.....	72
5.2.1	Vibration analysis before braking.....	72
5.2.2	Creep during braking.....	82
5.2.3	Frequency Analysis during braking.....	84
6	Conclusions and prospects.....	95
6.1	Conclusions	95
6.2	Prospects.....	96
7	References.....	97
	Annex A. Result Figures.....	101
	Annex B. Published papers.....	105

B.1 Frequency Analysis of the Railway Track under Loads Caused by the Hunting Phenomenon 105

B.2 Railcar Dynamic Response during Braking Maneuvers Based on Frequency Analysis 106

B.3. Method for predicting dynamic loads for a health monitoring system for subway tracks . 107

Figures index

Figure 2.1. The carbody is the principal component of the railway system.....	16
Figure 2.2. Principal parts of a railway bogie.....	16
Figure 2.3 Principal parts of a wheelset.....	17
Figure 2.4 Explanation of the differential cornering made possible by the conicity of the wheels in curves.	18
Figure 2.5 Profile and dimensions of rail 49E1	18
Figure 2.6. The contact patch between the rail and the wheel.	19
Figure 2.7 Principal wheel and rail radii (Garg, 2012).....	20
Figure 2.8 Diagram of the wheelset's free body.....	21
Figure 2.9 The development of tangential forces at the wheel-rail contact surfaces.....	26
Figure 2.10 The contact area is divided into two regions: slip region and adhesion	27
Figure 2.11 The connection between the motor and the rotary encoder.....	28
Figure 2.12 The sand ejection system.	29
Figure 2.13 Comparison of Kalker's theory and a model that fits the real measurements	30
Figure 2.14 The type of contamination on the rails affects how the tangential force behaves.....	31
Figure 3.1 Braking curve of a railway traction wheel.....	35
Figure 3.2 The 6 IMFs extracted from the encoder velocity.....	36
Figure 3.3 The sum of the first 3 IMFs of the braking curve.....	37
Figure 3.4 FFT spectrum of the IMFs 1 to 3 of the braking curve.	38
Figure 3.5 Spectrogram plot of the first three IMFs of the braking curve computed using CWT.	41
Figure 3.6 The proposed correlation method algorithm.....	42
Figure 3.7 Example of method proposed correlation method.	44
Figure 4.1 Dimensions and major components of the model vehicle used in the experiments	46
Figure 4.2 The vehicle positioned on the test bench's rails.....	46
Figure 4.3 Panoramic view of the test bench table.....	48
Figure 4.4 a) Detailed view of the test bench rails; b) track dimensions.	48
Figure 4.5 Traction bogie	50
Figure 4.6 Bottom view of the trail bogie, showing the optical sensor.....	50
Figure 4.7 The acquisition system components inside the vehicle's control box.	51
Figure 4.8 Schematic of the principal control and data acquisition modules of the vehicle.....	51
Figure 4.9 A dynamometer used to determine the coefficient of static friction resulting from the application of each friction modifier.....	53
Figure 4.10 Clean rails.....	54
Figure 4.11 Sand-scattered rails.	54
Figure 4.12 Braking zone diagram.....	56
Figure 4.13 Position of the test vehicle before the start of the experiment.	56
Figure 4.14 The area where braking experiments are conducted.....	57
Figure 4.15 Photograph of the vehicle completely stopped in the braking zone.	58
Figure 4.16 The primary procedures that were utilized throughout each experiment.	60
Figure 4.17 The process for analyzing the vibrational signals in the time domain.....	61
Figure 4.18 The process for analyzing the frequencies of vibrational signals.....	61
Figure 5.1 Time response of vehicle vibrations on greased rails in all three directions and rotations, before and during braking	65
Figure 5.2 Time response of the vehicle vibrations in all three directions and rotations, before and during braking, on clean rails.....	66
Figure 5.3 Time response of the vehicle vibrations in all three directions and rotations, before and during braking, on soap-coated rails.....	67
Figure 5.4 Time response of the vehicle vibrations in all three directions and rotations, before and during braking, on sand-scattered rails.	68
Figure 5.5 Kurtosis and crest factor indices of the vehicle's vibration data before braking.	69
Figure 5.6 Variance and RMS indices of the vehicle's vibration data before braking.....	70
Figure 5.7 Kurtosis and crest factor indices of the vehicle's vibration data during braking.	71

Figure 5.8 Variance and RMS indices of the vehicle's vibration data during braking.....	71
Figure 5.9 Frequencies obtained from the FFT analysis of the wheelset while running on greased rails.....	73
Figure 5.10 Results of the wheelset's CWT while running on greased rails.....	74
Figure 5.11 FFT spectrums of the vehicle's vibrations while running on greased rails.....	75
Figure 5.12 CWT spectrograms of the vehicle's vibrations while running on greased rails.....	76
Figure 5.13 The results of the wheel and vehicle correlation using the proposed correlation method while running on greased rails.....	77
Figure 5.14 Frequencies obtained from the FFT analysis of the wheelset while running on sand-scattered rails.....	78
<i>Figure 5.15 Results of the wheelset's CWT while running on sand-scattered rails.....</i>	79
Figure 5.16 FFT spectrums of the vehicle's vibrations while running on sand-scattered rails.....	80
Figure 5.17 CWT spectrograms of the vehicle's vibrations while running on sand-scattered rails.....	81
Figure 5.18 The results of the wheel and vehicle correlation using the proposed correlation method while running on sand-scattered rails.....	82
Figure 5.19 Behavior of vehicle and traction wheel speeds during a) greased rail test and b) sand-scattered rail test.....	83
Figure 5.20 The creep produced by braking. a) Greased rails have a creep of up to 80%, while b) sand-scattered rails have a creep of up to 60%.....	84
Figure 5.21 Frequencies obtained from the FFT analysis of the wheelset while braking on greased rails.....	85
Figure 5.22 Results of the wheelset's CWT while braking on greased rails.....	86
Figure 5.23 FFT spectrums of the vehicle's vibrations while braking on greased rails.....	87
Figure 5.24 CWT spectrograms of the vehicle's vibrations while braking on greased rails.....	88
Figure 5.25 The results of the wheel and vehicle correlation using the proposed correlation method while braking on greased rails.....	89
Figure 5.26 Frequencies obtained from the FFT analysis of the wheelset while braking on sand-scattered rails.....	90
Figure 5.27 Results of the wheelset's CWT while braking on sand-scattered rails.....	91
Figure 5.28 FFT spectrums of the vehicle's vibrations while braking on sand-scattered rails.....	92
Figure 5.29 CWT spectrograms of the vehicle's vibrations while braking on sand-scattered rails.....	93
Figure 5.30 The results of the wheel and vehicle correlation using the proposed correlation method while braking on sand-scattered rails.....	94

Tables index

Table 2.1 Commonly used parameters for simulating wet and dry rail wheel contact.....	32
Table 3.1 First rotations in the complex plane for $N = 8$	39
Table 4.1 Principal parameters of the scaled vehicle.....	47
Table 4.2 Principal technical features of the components of the acquisition system.....	49
Table 4.3 Experiment Matrix.....	55
Table 4.4 The instructions used to operate the vehicle.....	58

1 Introduction

The railway system is widely regarded as a highly efficient and safe mode of transportation. This system operates through a network of steel rails or tracks, along which a set of vehicles are propelled by a locomotive. Railway networks are prevalent in numerous countries, serving as a means of public transportation or facilitating the transportation of various products and raw materials.

Since its inception, trains have experienced derailment issues and significant infrastructure degradation, resulting in costly maintenance. The objective has consistently been to enhance the efficiency and speed of this system, owing to its significance, in order to counterbalance the substantial expenses incurred in its construction and maintenance.

For several decades, railway engineering has been dedicated to addressing issues related to the dynamics of trains and the oscillatory phenomena that arise during its operation. The forces at the interface between the wheel and rail are of significant magnitude and exhibit constant variations in both direction and amplitude. These interaction forces have a significant impact on the train's overall dynamics.

The dynamic response of a rail vehicle is directly influenced by the tangential forces generated in the wheel-rail contact area during the braking process. The coefficient of friction has an impact on the amplitude of frequency components in the dynamic

response of the vehicle. If the braking torque is not applied properly, large tangential forces may endanger the stability of rail vehicles (Zhang et al., 2009), and if applied abruptly, they may even cause damage to the train's wheels, engine, and rails. Braking can cause vibrations, and if they are severe enough, they can be transmitted to the body of the vehicle.

1.1 State of the art

The vibrations emanating from railway vehicles have the potential to cause discomfort to passengers and inflict damage on certain components of the railway infrastructure, as stated by Eroğlu et al. (2022). The issue of vibrations induced by trains passing over bridges has been addressed by Koç (2022), who has put forth a proposal for a linear actuator that can be customized for the secondary suspension system.

The vibrational features of a machine can be employed for the purpose of its condition monitoring. The aforementioned technique is similarly employed for the purpose of identifying defects in railway components. Lee et al (2011) attached accelerometers onto the bogie in order to identify lateral and vertical track anomalies. Tsunashima (2019) categorizes rail failures as vertical, lateral alignment, or level crossing using an algorithm based on machine learning. Wei et al (2016) incorporated accelerometers into the bogies to measure lateral and vertical vibrations, thereby determining track alignment. The authors Jauregui et al. (2022) employed an approach based on empirical mode decomposition (EMD) to derive a transfer function that facilitates the conversion of vehicle accelerations into track deformations. Their proposal's objective is to develop a visualization technique to depict the progression of deterioration in railway substructures, including tracks.

The tangential forces of the wheel that cause vibrations in the car are produced in a comparatively small contact area, an ellipse with a size of about 1 cm² (Iwnicki, 2006). The contact area under consideration exhibits separate areas of both traction and slip. The overall dynamic behavior of the wheel is determined by the interplay between the two regions, which is influenced by various factors such as the coefficient of friction, creep, lateral position of the wheel relative to the rail, and

presence of contaminants on the rails. The monitoring of tangential forces can be conducted through the use of vibration sensors on the vehicle body during routine maintenance, yielding highly promising outcomes. This approach has been successfully employed in the detection of polygonal wheels (Nielsen et al., 2000; Tao et al., 2019; Ye et al., 2022) and rail corrugation (Tanaka, 2016). This monitoring technique enables the identification of variations in the wheel-rail friction coefficient.

1.2 Hypothesis

The coefficient of friction has a significant impact on the acceleration of railroad vehicles. Consequently, the analysis of the vibration signal of the vehicle's body qualitatively estimates the wheel-rail friction coefficient in a railroad vehicle.

1.3 Objectives

1.3.1 General objective

Determine the wheels' coefficient of friction, as high or low, by analyzing the vibrations of a railway vehicle's body.

1.3.2 Specific objectives

- Subject the model vehicle to sudden braking having different coefficients of friction on the wheels.
- Analyze accelerometer vibration data using statistical indexes to study how the change in coefficient of friction affects the vehicle vibrations.
- Compare the analysis of the vehicle's vibration signals to that of the wheel in order to determine how the coefficient of friction affects the vehicle's dynamic response. That is, if they are similar, the vehicle's dynamic response is caused by tangential forces; if they are dissimilar, the vehicle's dynamic response is not caused by tangential forces.

1.4 Statement of the problem

There is a potential risk on rail vehicles if the brakes are not applied properly. To assist the railway vehicle's braking control system in making a decision, it must be aware of the rails on which the vehicle is braking. The coefficient of friction is a critical braking factor. For instance, excessive torque applied to rails with a low coefficient

of friction can cause the wheels to slip, resulting in unnecessary wear on the wheels and rails as well as a potential derailment risk. Conversely, if a very high torque is applied to a high coefficient of friction, there is a risk of severe damage to the traction system (shafts, gears, braking pads, etc.) and possibly the engine could be severely damaged or even burned.

For optimal braking of rail vehicles, it is critical to monitor tangential forces and coefficient of friction. Numerous modern rail vehicles have a Wheel Slip Protection System (WSP) integrated into their braking control. For optimal performance, the WSP is designed to prevent the railway wheels from locking during braking (a system very similar to automobiles' ABS). However, this system only considers variations in speed and slip when making braking control, which can be hazardous if the condition of the rails is unknown or if they are contaminated.

1.5 Justification

1.5.1 Scientific relevance

At present, there exists a lack of scholarly literature establishing a correlation between the friction coefficient of the wheels and the vibration magnitude experienced by the railway vehicles. The behavior of friction coefficient in train wheels is characterized by a high degree of nonlinearity and complexity. Therefore, the assessment of the amplitude and duration of vibrations of a vehicle's dynamic response could potentially aid in the examination of said forces.

1.5.2 Social relevance

The maintenance and upkeep of railway infrastructure holds significant societal importance as it facilitates the transportation of vital commodities such as raw materials, essential food and healthcare products, and contributes to economic development. Rail transport is a widely utilized mode of transportation in numerous countries, particularly in Europe and Eastern regions, where it serves as a primary means of commuting for thousands of individuals. Consequently, ensuring the optimal performance of rail vehicles is crucial to guarantee the safety of passengers and vital commodities.

2 Theoretical framework

This chapter presents a comprehensive overview of the interaction between a train and the rails, commencing with an exposition of the primary components of the railway system, such as bogie, wheelset and rail. A discussion of wheel-rail interaction phenomena such as creep and rolling friction is also covered. The present discussion endeavors to explain the underlying mechanics of friction in order to comprehend the formation of tangential forces within the wheel-rail contact patch.

2.1 Principal components of a train.

2.1.1 Wagon and bogies.

Wagons, such as the one depicted in Figure 2.1, comprise freight trains. Each wagon is supported by a pair of trucks known as bogies. The bogies are carriages-like structure with metal wheels that support the wagons so that they can be moved along the tracks; see Figure 2.2. Each bogie is connected to the wagon via a pivot (central plate), allowing for easy coupling to the various radii of curvature of the tracks. The bogies also feature a suspension system to absorb track irregularities and stabilize the train's overall dynamics.

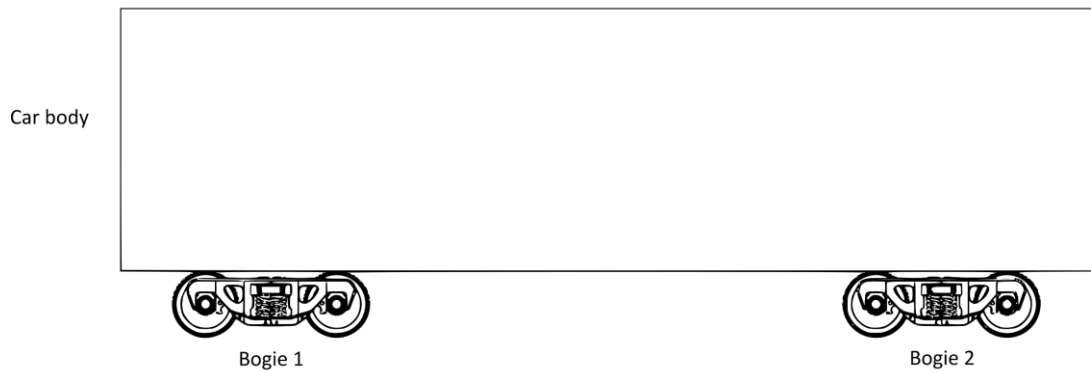


Figure 2.1. The carbody is the principal component of the railway system

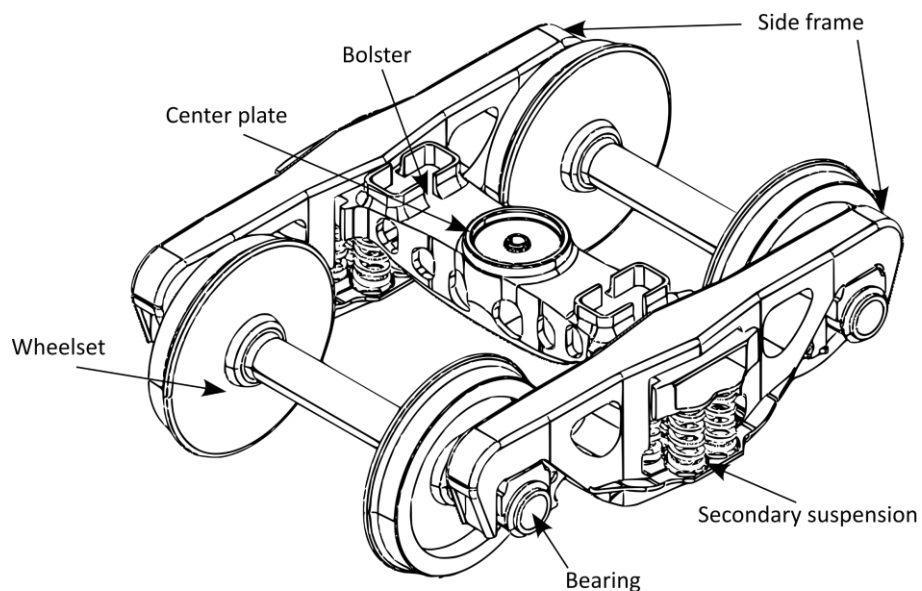


Figure 2.2. Principal parts of a railway bogie

2.1.2 Wheelset

The two wheels are rigidly attached to the axle; therefore, the two wheels and axle are a single unit known as a wheelset. A long history of incidents and field tests led to the current geometry of the wheels, which provides dynamic stability and reduces rail damage, particularly in curves, thereby reducing the possibility of derailment. Figure 2.3 depicts the primary components of a wheelset. Inside each wheel is a flange that prevents the wheel set from slipping off the tracks during lateral movement. On the inner face of each wheel is a flange that prevents the wheel set from slipping off the tracks when moving laterally.

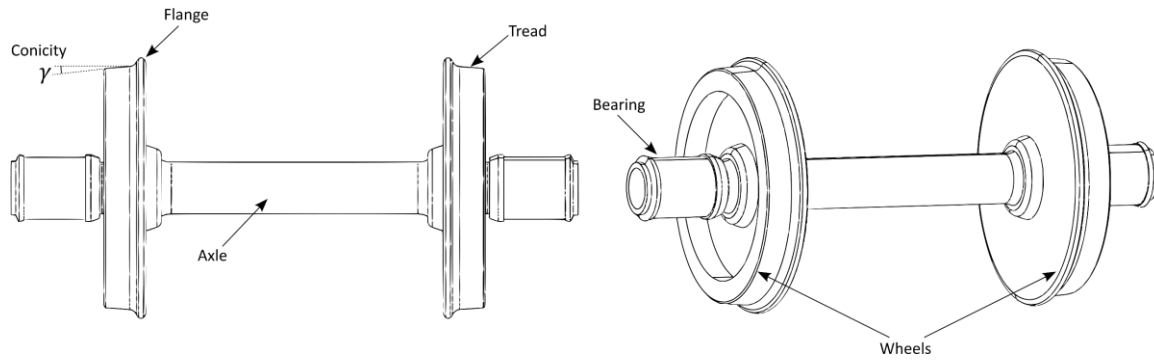


Figure 2.3 *Principal parts of a wheelset.*

The wheels have a conical profile that keeps them in the center of the track as they roll, preventing constant rubbing against the sides of the rail. This conical profile is also particularly helpful in curves because it functions as a differential, in which one wheel rotates at a faster tangential speed than the other. On a curve, the outer rail is longer than the inner rail, so the wheel on the outer rail has to roll at a greater tangential speed in order to travel a greater distance. Figure 2.4 illustrates how the wheelset's conical profile allows for differential cornering. In this image, a set of wheels rotating at an angular velocity will have the same tangential velocity V_T on both wheels if they are in the exact center of the tracks, since the left rolling radius r_i is equal to the right rolling radius r_d at the contact point. In contrast, when the set of wheels moves to the side by a distance y , the radii r_i and r_d are no longer equal. Therefore, despite having the same angular velocity, the tangential velocity of each wheel is different. When a train enters a curve, it moves to the outside of the curve, automatically activating the differential.

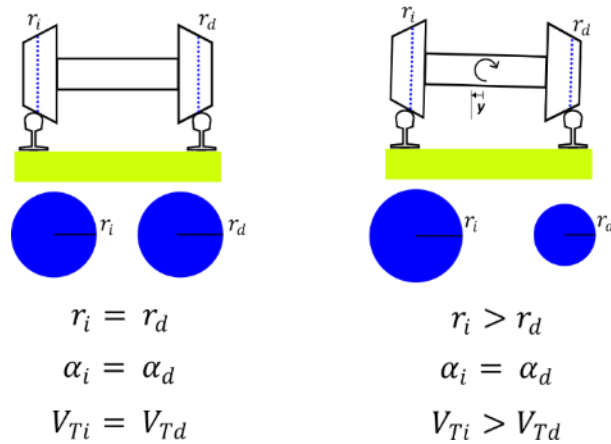


Figure 2.4 Explanation of the differential cornering made possible by the conicity of the wheels in curves. The blue circles illustrate how the radii of the wheels change when the wheelset is shifted to one side. Note that the conicity angle is exaggerated for illustration purposes.

2.1.3 Rail

The rail is one of the most important components of the railway system and receives the most maintenance attention. Its design and material allow it to withstand enormous efforts and forces in all directions. The depicted rail profile in Figure 2.5 conforms to EN 13674-1 standards, featuring a flat base and a head with multiple radii edges. The rail base is designed for convenient attachment to the sleepers, while the rail head is optimized to enhance wheel interaction and minimize stress, wear, and friction.

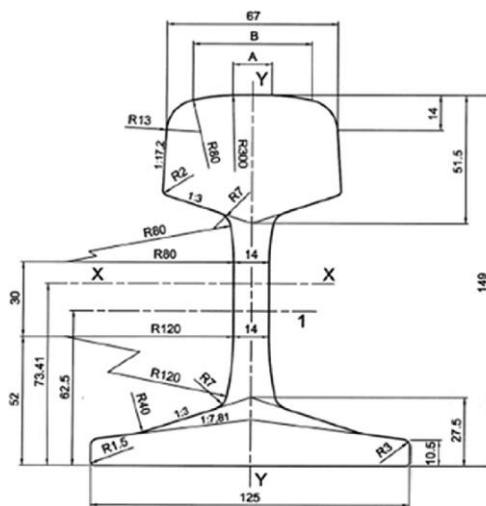


Figure 2.5 Profile and dimensions of rail 49E1 according to the EN 13674-1 standard (Yucel, 2017)

2.2 Wheel-rail interaction

The first person to show interest in researching the forces that interact between the wheel and the rail was Carter (1926). Carter employs mathematical equations to clarify the intricate non-linear nature of the tangential forces acting on the wheel. These forces are a function of the wheel-rail slippage and the position of the contact point between the wheel and the rail. Subsequently, improvements were made in the modeling of interaction forces by various researchers, such as Kalker (1979) and Johnson (1985).

2.2.1 Hertz's contact theory.

It is widely acknowledged that Hertz's contact theory can determine the pressure distribution and geometric shape of the contact area between two bodies. Figure 2.6 explains the application of Hertz's contact theory to railway wheel-rail contact. The shape and dimensions of the contact patch are determined by the surface's normal force and the elasticity of the materials in contact. In this instance, the theoretical contact area is flat and elliptical, which semi-axes are a and b , whereas the pressure distribution $p(x, y')$ is semi-ellipsoid.

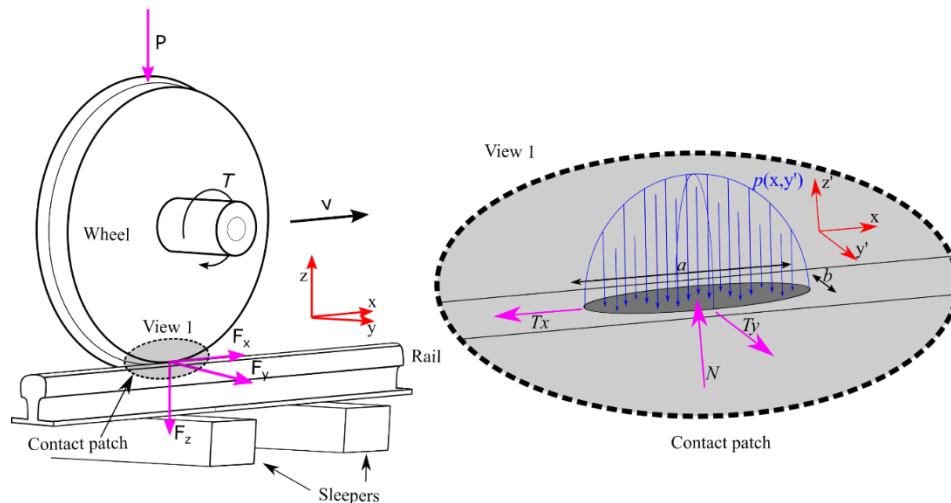


Figure 2.6. The contact patch between the rail and the wheel is an ellipse with semi-axes a and b , according to Hertz's contact theory. View 1 illustrates the forces at the contact patch in detail. The semi-axes of the contact patch are proportional to the magnitude of the vertical force P . The tangential forces T_x , T_y , and normal force N appear in the contact patch as a result of the forces applied by the wheel F_x , F_y , and F_z , which are the result of the torque T . Due to the conical profile and the oscillation of the wheelset, the reference frame of the contact patch $xy'z'$ changes during the step, so it differs slightly from the orthogonal xyz reference frame (Hurtado et al, 2022).

The semiaxes a and b of the elliptical contact patch are determined using

$$a = m[3\pi N(K_1 + K_2)/4K_3]^{1/3} \quad (2.1)$$

$$b = n[3\pi N(K_1 + K_2)/4K_3]^{1/3} \quad (2.2)$$

where N is the normal force pressing on both wheels. This particular case is applied to the contact of railway wheels and rails using the appropriate parameters:

$$K_1 = \frac{1 - \sigma_w^2}{\pi E_w}, \quad K_2 = \frac{1 - \sigma_R^2}{\pi E_R}, \quad K_3 = \frac{1}{2} \left[\frac{1}{R_1} + \frac{1}{R'_1} + \frac{1}{R_2} + \frac{1}{R'_2} \right] \quad (2.3)$$

where σ_w represents the Poisson modulus of the wheel and σ_R represents that of the rail. The radii are calculated as follows, where R'_2 is variable and dependent on the contact point:

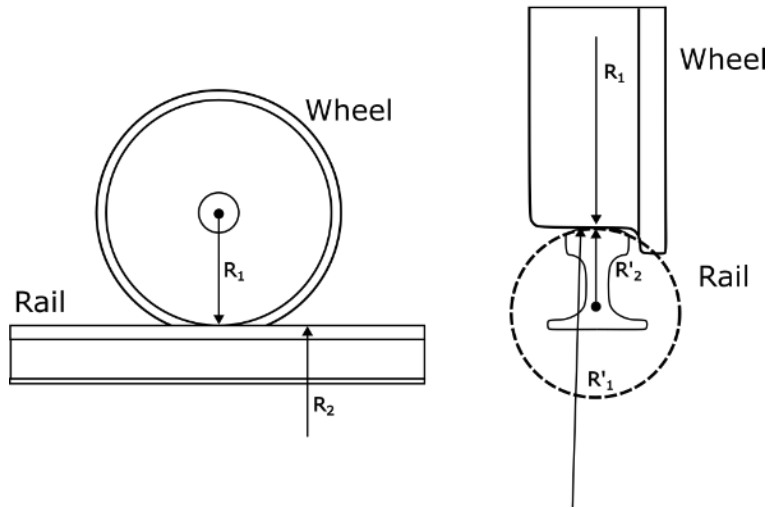


Figure 2.7 Principal wheel and rail radii (Garg, 2012)

In order to calculate m and n from equations 2.1 and 2.2, the following is defined

$$\theta = \cos^{-1} \left(\frac{K_4}{K_3} \right) \quad (2.4)$$

where

$$K_4 = \frac{1}{2} \left[\left(\frac{1}{R_1} + \frac{1}{R'_1} \right)^2 + \left(\frac{1}{R_2} + \frac{1}{R'_2} \right)^2 + 2 \left(\frac{1}{R_1} - \frac{1}{R'_1} \right) \left(\frac{1}{R_2} - \frac{1}{R'_2} \right) \cos 2\psi \right] \quad (2.5)$$

where ψ is the angle between the curvatures $\frac{1}{R_1}$ and $\frac{1}{R_2}$. Thus, the parameters m and n can be found in tables such as those published by Hertz (1895), based on the value of θ .

2.2.2 Forces in the contact point of a wheelset

The procedure for calculating the wheel-rail interaction forces, depicted in Figure 2.6, is explained below in order to comprehend how they affect the wheel's dynamics.

The wheelset's movement is not simple. Not only does the wheelset rotate along the rail, but it also rotates and moves in all directions. Typically, the longitudinal translation (x) is considered negligible, and also the vertical translation (z) and rotation around x (roll ϕ) are considered a function of lateral translation (y). Then, the principal movements are the lateral (y) and the rotation around z (yaw ψ). Figure 2.8 depicts the wheelset's free-body diagram.

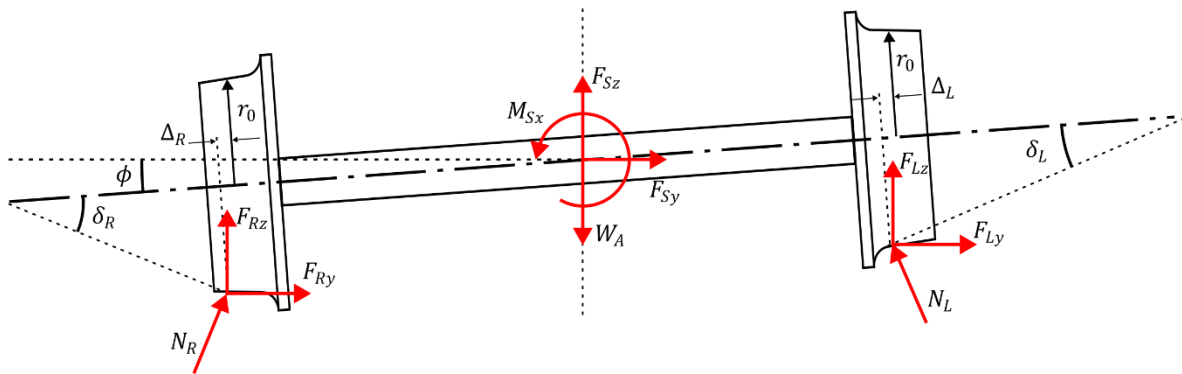


Figure 2.8 Diagram of the wheelset's free body. The direction of the forces N , F_y and F_z at the point of contact depends on the lateral position y . During lateral motion, the instantaneous radius ranges from r_0 to r . δ represents the instantaneous angle between the axis and contact point lines. Δ indicates the location of the contact point in relation to the wheel's center. The R and L subscripts represent the right and left sides, respectively (Garg, 2012)

The forces in the wheelset's free-body diagram are:

- F_L, F_R = Creep forces at the left and right contact points, respectively.
- M_L, M_R = Creep moments at the left and right contact points, respectively.
- F_S = Suspension forces.
- M_S = Suspension moments.
- W_A = Wheelset weight.
- N_L, N_R = Normal forces at the left and right contact points, respectively.

The equations of motion, based on Newton's equations, are written as:

$$m\ddot{\mathbf{r}} = \sum \mathbf{F} \quad (2.6)$$

$$d\mathbf{H}/dt = \sum \mathbf{M} \quad (2.7)$$

where H is the momentum, m is the mass of the wheelset and $\ddot{\mathbf{r}}$ is the position vector.

Equations 2.6 and 2.7 are expressed as:

$$\sum \mathbf{F} = \mathbf{F}_L + \mathbf{F}_R + \mathbf{N}_L + \mathbf{N}_R + \mathbf{F}_S + W_A \mathbf{k}''' \quad (2.8)$$

$$\sum \mathbf{M} = \mathbf{R}_R \times (\mathbf{F}_R + \mathbf{N}_R) + \mathbf{R}_L \times (\mathbf{F}_L + \mathbf{N}_L) + \mathbf{M}_L + \mathbf{M}_R + \mathbf{M}_S \quad (5.9)$$

Where \mathbf{R}_R and \mathbf{R}_L are the instantaneous contact points between the wheel and the rail, based on the geometry of both wheel and rail.

2.2.3 Creep forces

Sliding between the wheel and the rail generates creep forces, which impact the wheels at the contact point. Such forces are caused by creep (slip) in the contact area, which result in unequal deformations and surface stresses in both bodies. This phenomenon occurs when two bodies are joined by strong pressure and one rolls over the other with traction. In Hertz's contact theory, the contact region is assumed

to be elliptical, with semi-axes a and b being determined by the aforementioned equations (2.1–2.5). The size of the contact patch is thus determined by the geometry of the bodies in contact, the normal force, and the mechanical properties of the bodies. At the contact point, the tangential velocities of the rail and the wheel are not identical. Even a seemingly insignificant difference in speeds is enough to produce creep forces that excite the wheels and spread vibrations throughout the train.

Carter (1926) was the first to define creep at the contact point by using the following expressions:

$$\varepsilon'_x = \frac{(V \text{ wheel longitudinal} - V \text{ rail longitudinal})}{V \text{ vehicle nominal}} \quad (2.9)$$

$$\varepsilon'_y = \frac{(V \text{ wheel lateral} - V \text{ rail lateral})}{V \text{ vehicle nominal}} \quad (2.10)$$

$$\varepsilon'_{sp} = \frac{(V \text{ wheel angular} - V \text{ rail angular})}{V \text{ vehicle nominal}} \quad (2.11)$$

Assuming small contact angles and ignoring vertical translation and roll, the creep can be calculated for both wheels using:

Left wheel:

$$\varepsilon'_{xL} = \frac{V(1 - r_L/r_0) - a\dot{\psi}}{V} \quad (2.12)$$

$$\varepsilon'_{yL} = \frac{\dot{y} + r_L\dot{\phi} - V\dot{\psi}}{V} \quad (2.13)$$

$$\varepsilon'_{spL} = \frac{\dot{\psi} - \Omega\delta_L}{V} \quad (2.14)$$

Right wheel:

$$\mathcal{E}'_{xR} = \frac{V(1 - r_L/r_0) + a\dot{\psi}}{V} \quad (2.15)$$

$$\mathcal{E}'_{yR} = \frac{\dot{y} + r_R\dot{\phi} - V\psi}{V} \quad (2.16)$$

$$\mathcal{E}'_{spR} = \frac{\dot{\psi} + \Omega\delta_R}{V} \quad (2.17)$$

Kalker's (1972) linear theory is used to relate creep forces to wheel slip:

Left wheel:

$$F_{Lx} = F'_{Lx} \cos \psi - F'_{Ly} \cos(\delta_L + \phi) \sin \psi \quad (2.18)$$

$$F_{Ly} = F'_{Lx} \sin \psi + F'_{Ly} \cos(\delta_L + \phi) \cos \psi \quad (2.19)$$

$$F_{Lz} = F'_{Ly} \sin(\delta_L + \phi) \quad (2.20)$$

$$M_{Lx} = M'_{Lz} \sin(\delta_L + \phi) \sin \psi \quad (2.21)$$

$$M_{Ly} = -M'_{Lz} \sin(\delta_L + \phi) \cos \psi \quad (2.22)$$

$$M_{Lz} = M'_{Lz} \cos(\delta_L + \phi) \quad (2.23)$$

Right wheel:

$$F_{Rx} = F'_{Rx} \cos \psi - F'_{Ry} \cos(\delta_R - \phi) \sin \psi \quad (2.24)$$

$$F_{Ry} = F'_{Rx} \sin \psi + F'_{Ry} \cos(\delta_R - \phi) \cos \psi \quad (2.25)$$

$$F_{Rz} = -F'_{Ry} \sin(\delta_R - \phi) \quad (2.26)$$

$$M_{Rx} = -M'_{Rz} \sin(\delta_R - \phi) \sin \psi \quad (2.27)$$

$$M_{Ry} = M'_{Rz} \sin(\delta_R - \phi) \cos \psi \quad (2.28)$$

$$M_{Rz} = M'_{Rz} \cos(\delta_R - \phi) \quad (2.29)$$

Where F'_x , F'_y and M'_z are forces and moments of longitudinal, lateral and spin creep, respectively, and can be calculated using:

$$F'_x = -f_{33}\mathcal{E}'_x \quad (2.30)$$

$$F'_y = -f_{11}\mathcal{E}'_y - f_{12}\mathcal{E}'_{sp} \quad (2.31)$$

$$M'_z = f_{12}\mathcal{E}'_y - f_{22}\mathcal{E}'_{sp} \quad (2.32)$$

Terms f_{11} , f_{12} , f_{22} and f_{33} are called Kalker coefficients and are obtained by the following expressions

$$f_{11} = (ab)GC_{22} \quad (2.33)$$

$$f_{12} = (ab)^{3/2}GC_{23} \quad (2.34)$$

$$f_{22} = (ab)^2GC_{33} \quad (2.35)$$

$$f_{33} = (ab)GC_{11} \quad (2.36)$$

where:

- G = Modulus of rigidity of rails and wheels (they are considered to be of the same material)
- C_{ij} = Creepage and spin coefficients, which are dependent on the Poisson's ratio σ and the ratio a/b , can be found in tables such as those in Kalker (1972) and Garg (2012).

2.3 Rolling friction

Frictional force refers to the opposing force that acts against the motion of a body when it comes into contact with another body's surface. This definition also applies to a wheel rolling on a rail, as the rail resists the wheel's motion and dissipates its kinetic energy. This resistance to motion is dependent on three mechanisms that take place at the moment of contact (Suh and Sin, 1981):

- Impact and asperity deformation on both surfaces,

- Adhesion of sliding surfaces
- Encrustations of particles on both surfaces (plowing).

2.3.1 Wheel-rail's friction model

The free-body diagram of a traction wheel exerting a vertical force P on a rail is depicted in Figure 2.9. The engine of the railway vehicle applies a torque T to the drive wheel, causing it to rotate at an angular velocity on the rail and propelling the vehicle at a speed V . The tangential thrust occurs in the small contact area and is caused by the appearance of the friction force F_f , which acts in opposition to the tangential thrust force F_T .

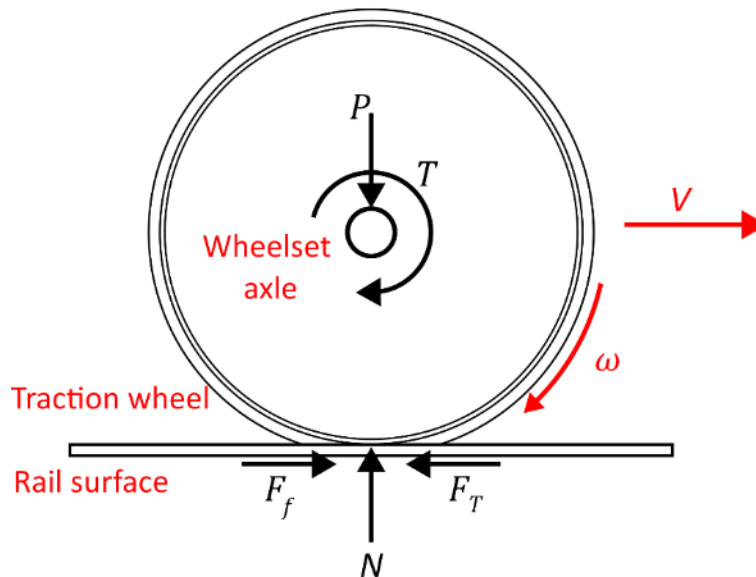


Figure 2.9 The development of tangential forces at the wheel-rail contact surfaces. Through a torque T and an angular velocity ω , the wheel exerts a tangential traction force F_T on the rail surface. The frictional force F_f has the same magnitude as F_T , but acts in the opposite direction.

Frictional force F_f is obtained from

$$F_f = \mu P \quad (2.37)$$

where μ is the friction coefficient. This straightforward model is the well-known Coulomb model and is widely accepted to model the friction behavior on clean rails.

Under optimal friction conditions, the wheel has full traction, i.e., no slippage between wheel and rail. However, the reality is that there is always a small amount of slippage. The contact area is then said to contain a slip region and an adhesion

region. The slip region can be expanded until the wheel is completely slipping on the rail. In this condition, the tangential force is saturated and equals μP . This can occur if the force P is insufficient or if the engine torque increases abruptly, which is very common during violent acceleration or deceleration.

Figure 2.10 depicts the F_T -creep curve, which demonstrates how the adhesion and slip zones change as these two variables evolve (Olofsson, 2009). When the creep is low, the adhesion region covers nearly the entire contact area, resulting in small tangential forces. As the creep increases, the tangential forces increase until they reach a critical value at which the entire area begins to slip.

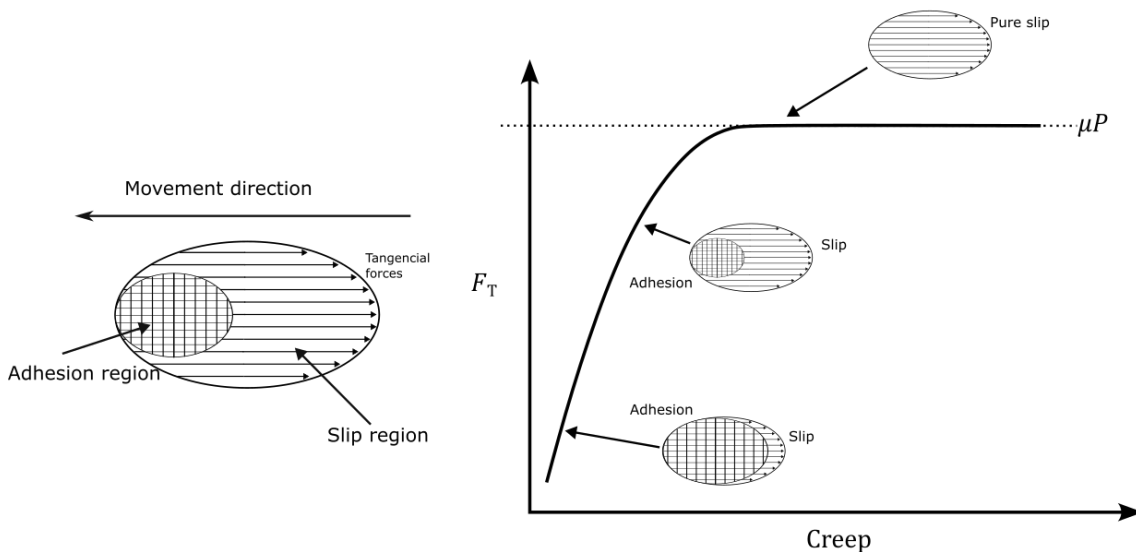


Figure 2.10 The contact area is divided into two regions: slip region and adhesion region. The size of these two regions is determined by creep. When the sliding region extends across the entire contact area, the value of the tangential forces equals the kinetic friction as the creep increases (Olofsson, 2009)

2.3.2 Monitoring of the wheel's tangential forces

The behavior of the forces in the wheel-rail contact can be studied using a sensor connected to the drive wheel, as depicted in Figure 2.11. Not only is the incremental encoder used to measure the speed of the drive wheel, but the captured speed signal also reflects the dynamics of the wheel over time. In the traction wheel's speed signal, any change or vibration caused by a disturbance in the drive wheel can be monitored.

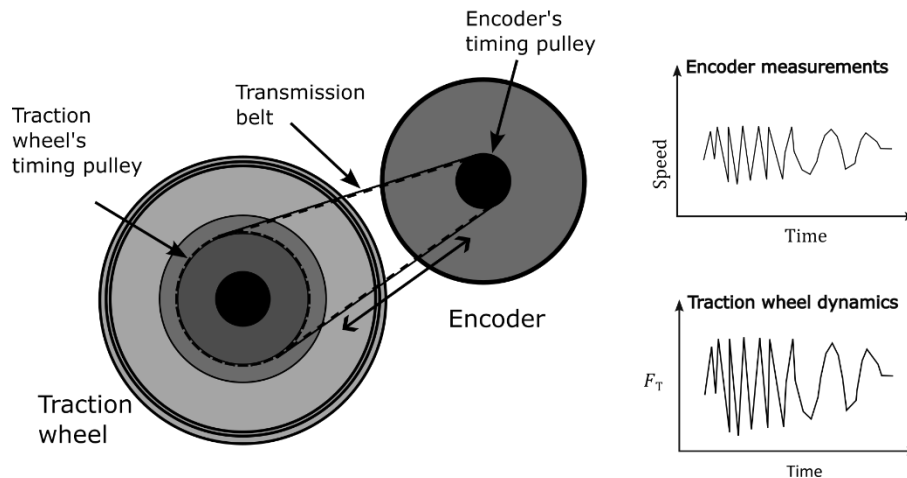


Figure 2.11 The connection between the motor and the rotary encoder using a timing belt. This diagram demonstrates why the tangential forces acting on the wheel are perceived in the encoder signal.

2.3.3 Friction modifiers

The value of μ under dry and clean conditions is approximately 0.3 (Moore, 1975). This value depends on the nature of the contaminants in the rails and is not constant. Due to the fact that the rails and wheels are exposed to the environment, it is impossible to maintain optimal friction conditions for optimal performance. On rails, contaminants such as water, snow, leaves, and even grease are commonly found. In these instances, friction modifiers are required to improve traction when contamination on the rails makes it difficult for the wheels to gain traction (Harmon & Lewis, 2016).

Numerous researchers, including Lu & Eadie (2005), Arias-Cuevas et al (2010) and Lundberg et al (2015), have examined various friction modifiers to determine which provides the best starting traction performance. According to reports, an increase in the coefficient of friction improves the locomotives' dynamic performance. On the other hand, it has been observed that the rear wheels have better traction due to the fact that the front wheels remove a portion of the dirt (Bosso et al, 2019). However, this only improves the performance of the rear wheels by 20%, compared to 32% when using friction modifiers such as sand. Therefore, friction modifiers are preferred to enhance acceleration or braking in low-friction conditions, as well as to prevent

skidding on hills. Figure 2.12 depicts a mechanism that dispenses sand between the rail and drive wheel.

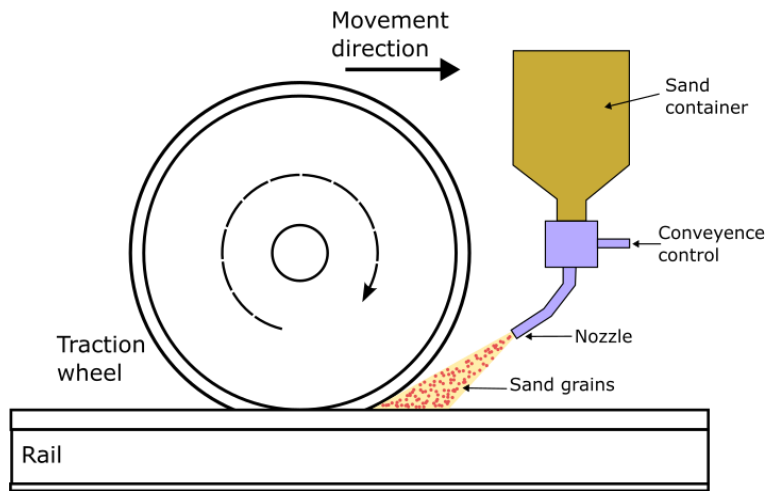


Figure 2.12 The sand ejection system. Sand is applied between the wheel and rail to enhance the coefficient of friction on rails that are contaminated (Roberts, 2021)

Typically, the performance of wheels under various rail friction conditions is depicted on an adhesion curve similar to Figure 2.12, in which longitudinal creep is plotted against tangential force. In this graph, two curves are presented: the adherence curve of Kalker's theory and a more realistic adherence curve (Vollebregt, 2013). Based on Coulomb's friction model, Kalker's creep theory is an ideal curve used on rails without contaminants. The * are real measurements taken on contaminated rails, which exhibit a different behavior than the Kalker curve. The other, more accurate curve was generated by the extended CONTACT algorithm, which approximates the behavior of actual measurements more accurately.

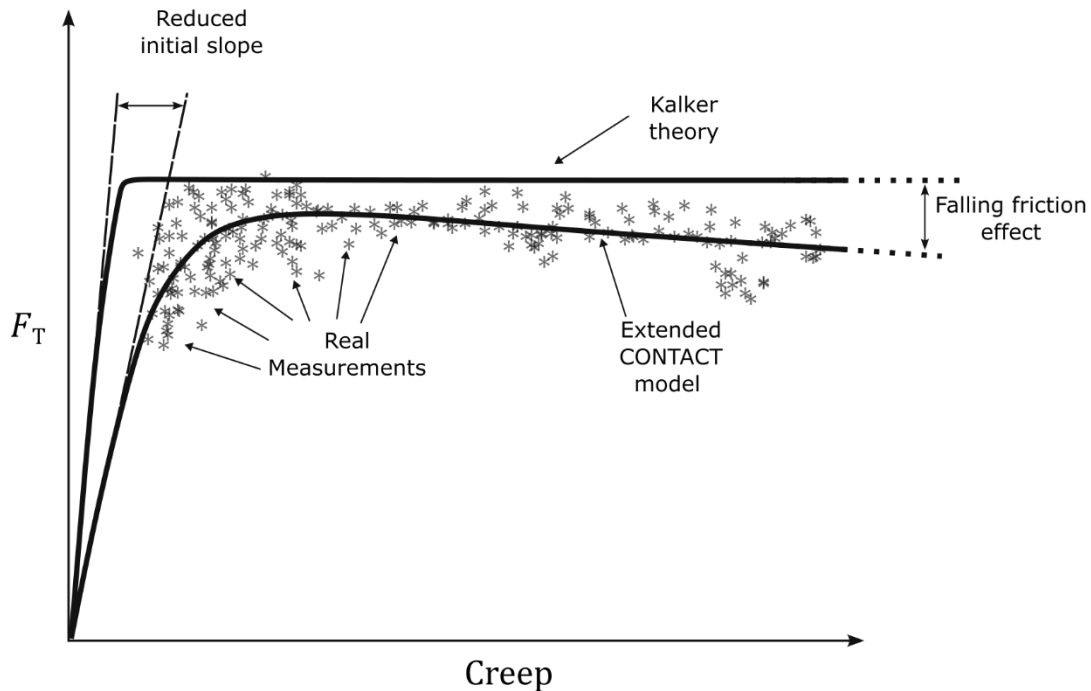


Figure 2.13 Comparison of Kalker's theory and a model that fits the real measurements (extended CONTACT model). In fact, tangential forces have a lower initial slope and tend to decrease after reaching their maximum value (Vollebregt, 2013).

Two main characteristics distinguish the experimental measurement curves from the behavior of clean rails: a smaller initial slope and a decrease in friction as creep increases. It is believed that contaminants in the rail and/or roughness on both surfaces contributed to the reduced initial slope, while the decrease in friction is primarily caused by an increase in temperature as creep increases. As seen in Figure 2.13, the tangential forces are smaller on wet rails than on dry rails, and the reduced initial slope and falling friction effect depend on the type of contaminant as well.

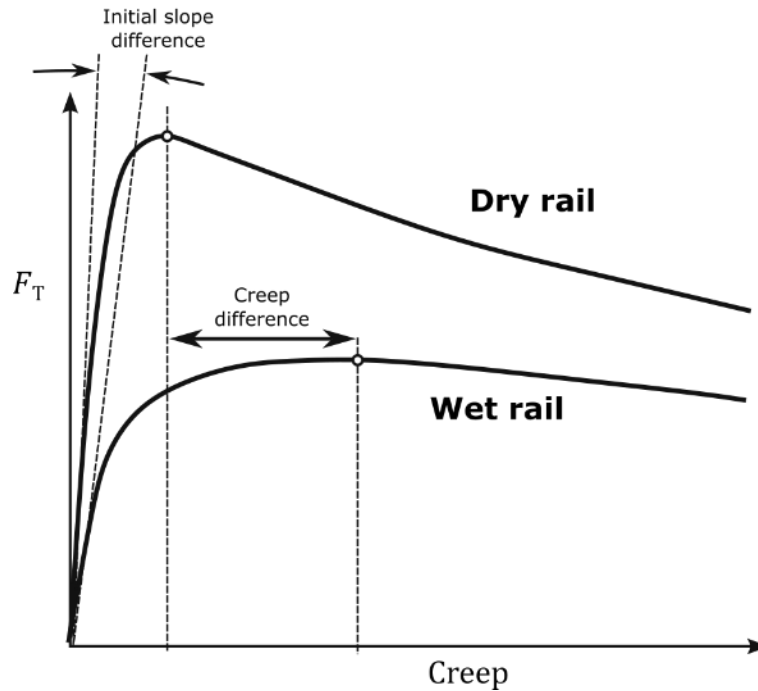


Figure 2.14 The type of contamination on the rails affects how the tangential force behaves. (Polach, 2005)

There have been numerous attempts to model the behavior of real adhesion curves. Polach (1999) suggests the following model:

$$F_T = \frac{2Q\mu}{\pi} \left(\frac{\varepsilon}{1 + \varepsilon^2} + \arctan(\varepsilon) \right) \quad (2.38)$$

$$\varepsilon = \frac{2}{3} \frac{C\pi a^2 b}{Q\mu} s \quad (2.39)$$

where G denotes the materials' modulus of rigidity, s denotes creep, and C denotes a proportionality factor that describes the contact stiffness (Kalker, 1967). The semi-axes of the contact patch a and b were described in section 4.2.1. To simulate the falling friction effect, in very large creeps, the coefficient of friction is taken as a function of speed:

$$\mu = \mu_0 [(1 - A)e^{-Bs} + A] \quad (2.40)$$

where μ_0 denotes the static coefficient of friction, B denotes an empirically determined constant that simulates the exponent of the friction drop, and A denotes the ratio between μ_∞ (at creep $\rightarrow \infty$) and μ_0 .

$$A = \frac{\mu_\infty}{\mu_0} \quad (2.41)$$

Some typical values for these parameters for dry and wet rails are shown in Table 2.1.

Table 2.1 Commonly used parameters for simulating wet and dry rail wheel contact.

Parameter	Dry rail	Wey rail
μ_0	0.55	0.30
A	0.40	0.40
B	0.60	0.20

3 Analytical methods for vibrations

In this section the methods used for the analysis of vibration signals in the time and frequency domain are presented.

3.1 Time domain analysis technics.

The techniques presented here are among the most common methods for diagnosing defects in vibrating machines. These methods of analysis will be used to detect variations in the amplitudes of the vibrations from the rail vehicle.

3.1.1 Kurtosis

The kurtosis of a distribution measures the dispersion around its mean value. When the kurtosis is large, most of the data points are atypical. Kurtosis is proportional to the difference between the mean value \bar{x} and the standard deviation s .

$$K = \frac{1}{n} \frac{\sum (x_i - \bar{x})^4}{s^4} \quad (3.1)$$

3.1.2 Root mean square (RMS)

The RMS of a given data set x_1, x_2, \dots, x_n , is the square root of the mean value of the squared data set. This value is calculated as:

$$RMS = \sqrt{\frac{1}{n}(x_1^2 + x_2^2 + \dots + x_n^2)} \quad (3.2)$$

3.1.3 Crest factor (CF)

CF is the ratio of peak values to the RMS value. The crest factor characterizes the amplitude variation of a waveform by revealing the magnitude of its peaks. The formula for this is:

$$CF = \frac{\text{Peak value}}{RMS} \quad (3.3)$$

3.1.4 Variance

The variance represents the degree of dispersion of a sample of data in relation to its mean value \bar{x} . To calculate it, the quadratic sum of each data's difference from the mean must be taken:

$$s^2 = \frac{\sum(x_i - \bar{x})^2}{n - 1} \quad (3.4)$$

3.2 Frequency domain analysis technics

3.2.1 Empirical Mode Decomposition (EMD)

The presence of extremely low or extremely high frequency components in the acquired signals can distort the results of frequency analysis. Low-frequency components are referred to as rigid-body modes and appear when the acquired signal has a mean value that is significantly greater than zero, whereas higher-frequency components are likely noise. In these instances, EMD is applied to the analyzed signal in order to filter out vibration modes that are not useful for the analysis. EMD divides the signal being analyzed into a series of fundamental signals known as intrinsic mode functions (IMFs). Each IMF is a signal with a single carrier tone, with the property that the number of zero crossings must equal the sum of the maximum and minimum values, and the original signal is recovered by adding them all together.

The following is a description of the process for extracting IMF functions from a signal:

1. The first step is to obtain the upper and lower envelopes of the original signal using splines.
2. The next step is to calculate an IMF by averaging the envelopes. Here begins an iterative procedure in which the algorithm has to find the first IMF under the condition that the envelopes have a very small mean value.
3. What follows is to subtract the first IMF from the original signal.
4. Repeat steps 2 and 3 to subtract the IMF functions from the signal.
5. The procedure ends when the residual signal is no longer oscillatory.

As an example, to illustrate the use of the EMD, a signal obtained from a speed sensor of a traction wheel at the time of braking, in which medium and high frequencies must be analyzed, see Figure 3.1. It can be seen that the speed's behavior is not entirely oscillatory, except at high frequencies. If the signal is analyzed as is, the behavior of the medium and high frequencies cannot be observed.

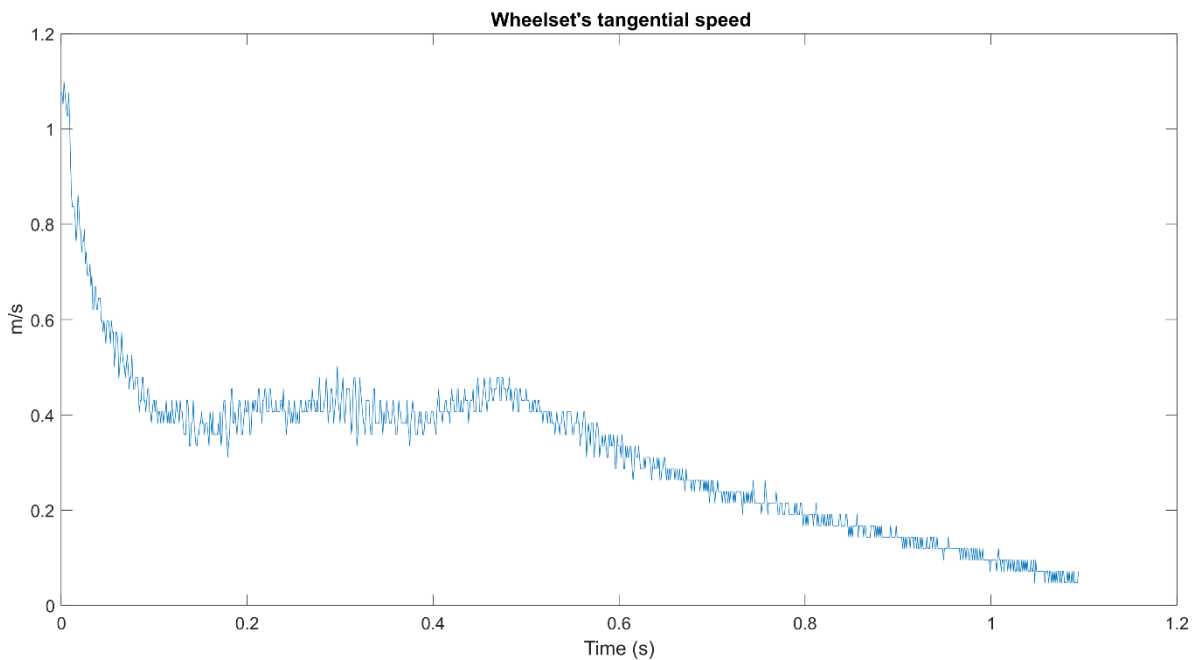


Figure 3.1 Braking curve of a railway traction wheel.

The IMFs extracted from the encoder velocity are depicted in Figure 3.2. The first IMF holds the highest frequencies, while the last has the lowest. The EMD also leaves behind a residue that is no longer oscillatory and therefore cannot be considered as an IMF. If the IMFs from the first to the third are added together, the curve depicted in Figure 3.3 is obtained, which is easiest to analyze with a frequency analysis tool because it lacks rigid body modes.

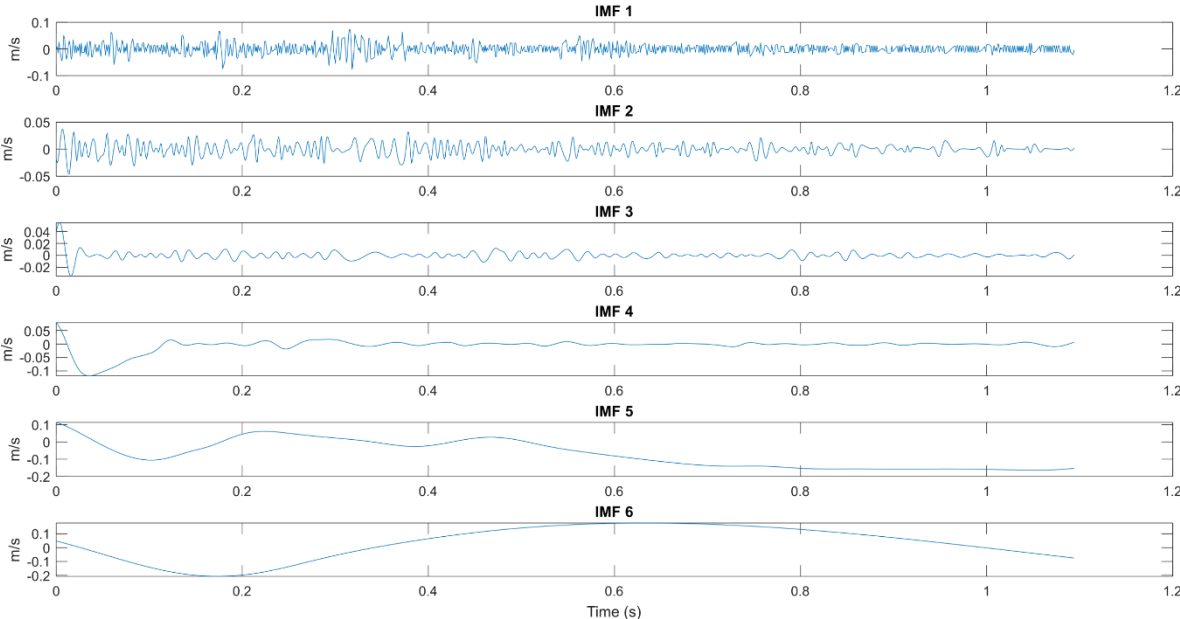


Figure 3.2 The 6 IMFs extracted from the encoder velocity.

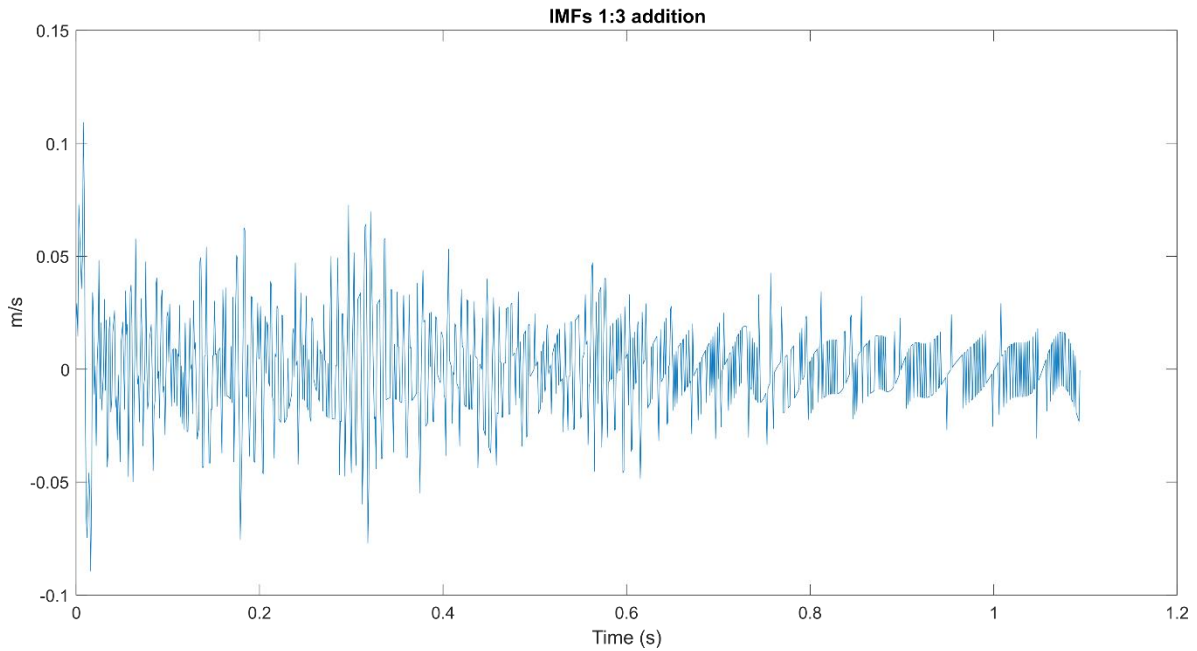


Figure 3.3 *The sum of the first 3 IMFs of the braking curve.*

3.2.2 Fast Fourier transform (FFT)

FFT is a commonly employed method for determining the frequency components of vibration signals. The result is the spectrum of frequencies contained in the signal under analysis. The frequency spectrum applied to the braking curve from Figure 3.1 is shown in Figure 3.4. There are quite a few peaks in this spectrum, the ones with the greatest amplitude representing the principal frequency components (12, 144, and 156 Hz).

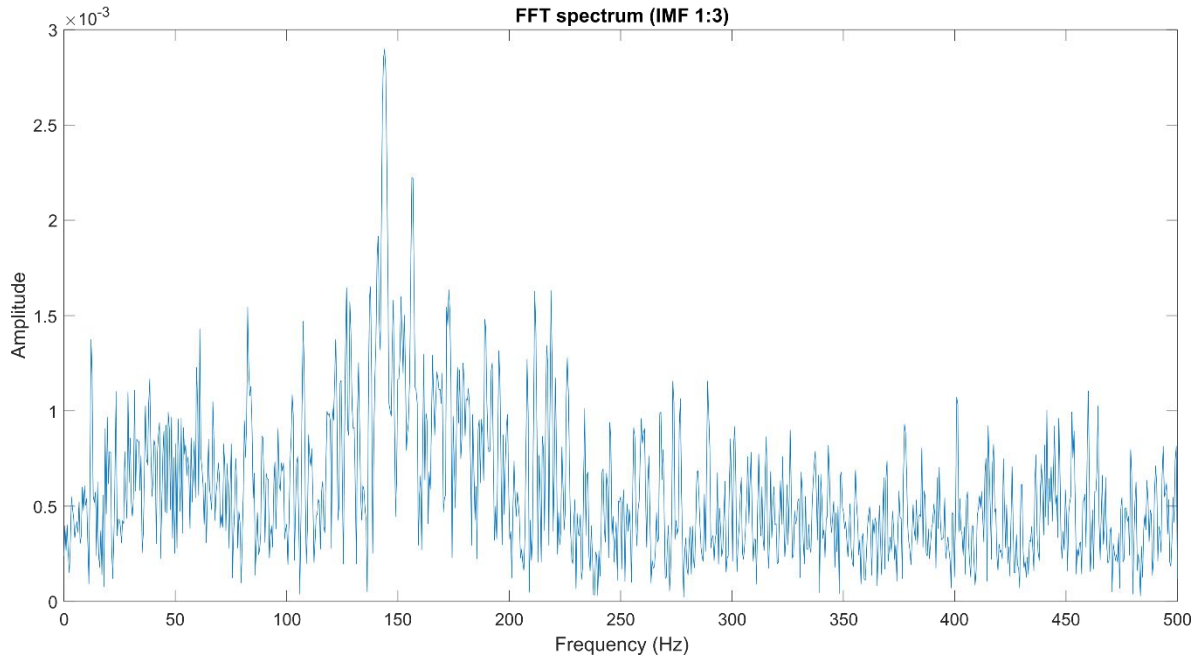


Figure 3.4 FFT spectrum of the IMFs 1 to 3 of the braking curve.

To fully understand how the FFT algorithm works, the Discrete Fourier Transform (DFT) is first presented in matrix form:

$$\mathbf{G}_k = \frac{1}{N} \mathbf{W}_{kn} \mathbf{g}_n \quad (3.5)$$

where \mathbf{g}_n is the vector containing the samples of the signal in time, \mathbf{G}_k is the vector containing the N frequency components of the signal, and \mathbf{W}_{kn} is a matrix of unit vectors $e^{-j2\pi kn/N}$ representing how much to rotate each sample of \mathbf{g}_n in the complex plane (Randall, 2021). Table 3.1 details the eight rotations of $n = 0, 2, \dots, 7$ and $k = 1$ in the complex plane for the particular case $N = 8$.

Table 3.1 First rotations in the complex plane for $N = 8$

n	$e^{-j2\pi n/8}$	Complex-plane direction
0	0	↑
1	-45	↗
2	-90	→
3	-135	↘
4	-180	↓
5	-225	↙
6	-270	←
7	-315	↖

The matrix \mathbf{W}_{kn} for $N = 8$ is as follows:

$$\mathbf{W}_{kn} = \begin{bmatrix} \uparrow & \uparrow & \uparrow & \uparrow & \uparrow & \uparrow & \uparrow & \uparrow \\ \uparrow & \nearrow & \rightarrow & \searrow & \downarrow & \swarrow & \leftarrow & \nwarrow \\ \uparrow & \rightarrow & \downarrow & \leftarrow & \uparrow & \rightarrow & \downarrow & \leftarrow \\ \uparrow & \searrow & \leftarrow & \nearrow & \downarrow & \nwarrow & \rightarrow & \swarrow \\ \uparrow & \downarrow & \uparrow & \downarrow & \uparrow & \downarrow & \uparrow & \downarrow \\ \uparrow & \swarrow & \rightarrow & \nwarrow & \downarrow & \nearrow & \leftarrow & \searrow \\ \uparrow & \leftarrow & \downarrow & \rightarrow & \uparrow & \leftarrow & \downarrow & \rightarrow \\ \uparrow & \nwarrow & \leftarrow & \swarrow & \downarrow & \searrow & \rightarrow & \nearrow \end{bmatrix} \begin{matrix} \dots 000 (0) \\ \dots 001 (1) \\ \dots 010 (2) \\ \dots 011 (3) \\ \dots 100 (4) \\ \dots 101 (5) \\ \dots 110 (6) \\ \dots 111 (7) \end{matrix} \quad (3.6)$$

The FFT is an algorithm that calculates the Discrete Fourier Transform (DFT) more efficiently. As illustrated by $N=8$, the FFT algorithm rearranges the rows of the \mathbf{W}_{kn} matrix into \mathbf{W}'_{kn} , for $N = 8$:

$$\mathbf{W}'_{kn} = \begin{bmatrix} \uparrow & \uparrow & \uparrow & \uparrow & \uparrow & \uparrow & \uparrow & \uparrow \\ \uparrow & \downarrow & \uparrow & \downarrow & \uparrow & \downarrow & \uparrow & \downarrow \\ \uparrow & \rightarrow & \downarrow & \leftarrow & \uparrow & \rightarrow & \downarrow & \leftarrow \\ \uparrow & \leftarrow & \downarrow & \rightarrow & \uparrow & \leftarrow & \downarrow & \rightarrow \\ \uparrow & \nearrow & \rightarrow & \searrow & \downarrow & \swarrow & \leftarrow & \nwarrow \\ \uparrow & \swarrow & \rightarrow & \nwarrow & \downarrow & \nearrow & \leftarrow & \searrow \\ \uparrow & \searrow & \leftarrow & \nearrow & \downarrow & \nwarrow & \rightarrow & \swarrow \\ \uparrow & \nwarrow & \leftarrow & \swarrow & \downarrow & \searrow & \rightarrow & \nearrow \end{bmatrix} \begin{matrix} \dots 000 (0) \\ \dots 100 (4) \\ \dots 010 (2) \\ \dots 110 (6) \\ \dots 001 (1) \\ \dots 101 (5) \\ \dots 011 (3) \\ \dots 111 (7) \end{matrix} \quad (3.7)$$

In this example, a bit inversion is performed (001 becomes 100, 011 becomes 110, etc.). The matrix \mathbf{W}'_{kn} factors into $N \log(N)$ matrices with relative ease. By substituting these factors for \mathbf{W}'_{kn} in equation 3.3, the number of operations is

drastically reduced. In this example with $N = 8$, the operations are reduced from 64 to 24, but for $N = 1024$ there are up to 100 times fewer operations.

$$W'_{kn} = \begin{bmatrix} \uparrow & \uparrow & 0 & 0 & 0 & 0 & 0 & 0 \\ \uparrow & \downarrow & 0 & 0 & 0 & 0 & 0 & 0 \\ 0 & 0 & \uparrow & \leftarrow & 0 & 0 & 0 & 0 \\ 0 & 0 & \uparrow & \rightarrow & 0 & 0 & 0 & 0 \\ 0 & 0 & 0 & 0 & \uparrow & \swarrow & 0 & 0 \\ 0 & 0 & 0 & 0 & \uparrow & \nearrow & 0 & 0 \\ 0 & 0 & 0 & 0 & 0 & 0 & \uparrow & \swarrow \\ 0 & 0 & 0 & 0 & 0 & 0 & \uparrow & \nearrow \end{bmatrix} \begin{bmatrix} \uparrow & 0 & \uparrow & 0 & 0 & 0 & 0 & 0 \\ 0 & \uparrow & 0 & \uparrow & 0 & 0 & 0 & 0 \\ \uparrow & 0 & \downarrow & 0 & 0 & 0 & 0 & 0 \\ 0 & \uparrow & 0 & \downarrow & 0 & 0 & 0 & 0 \\ 0 & 0 & 0 & 0 & \uparrow & 0 & \rightarrow & 0 \\ 0 & 0 & 0 & 0 & 0 & \uparrow & 0 & \rightarrow \\ 0 & 0 & 0 & 0 & 0 & 0 & \uparrow & \leftarrow \\ 0 & 0 & 0 & 0 & 0 & \uparrow & 0 & \leftarrow \end{bmatrix} \begin{bmatrix} \uparrow & 0 & 0 & 0 & \uparrow & 0 & 0 & 0 \\ 0 & \uparrow & 0 & 0 & 0 & \uparrow & 0 & 0 \\ 0 & 0 & \uparrow & 0 & 0 & 0 & \uparrow & 0 \\ 0 & 0 & 0 & \uparrow & 0 & 0 & 0 & \uparrow \\ \uparrow & 0 & 0 & 0 & \downarrow & 0 & 0 & 0 \\ 0 & \uparrow & 0 & 0 & 0 & \downarrow & 0 & 0 \\ 0 & 0 & \uparrow & 0 & 0 & 0 & \downarrow & 0 \\ 0 & 0 & 0 & \uparrow & 0 & 0 & 0 & \downarrow \end{bmatrix} \quad (3.8)$$

3.2.3 Continuous wavelet transform (CWT)

The CWT is a method for analyzing the frequency behavior of a signal over time by translating and scaling wavelets (a wave signal). This method makes it simple to determine whether the analyzed vibratory phenomenon has a linear or nonlinear behavior. The expression for the CWT is derived from the expression for the convolution:

$$W(a, b) = \frac{1}{\sqrt{a}} \int_{-\infty}^{\infty} x(t) \psi * \left(\frac{(t - b)}{a} \right) dt \quad (3.9)$$

where $\psi(t)$ represents the mother wavelet, which is translated by b and stretched by a . The Morlet mother wavelet is used in this study because it is the most suitable for evaluating nonlinear vibration phenomena (Hurtado et al., 2022), which has the time domain form:

$$\psi(t) = \frac{\sigma}{\sqrt{\pi}} e^{-\sigma^2 t^2} e^{j2\pi f_0 t} \quad (3.10)$$

Where the wavelet's central frequency is denoted by f_0 , while its width is represented by σ . The CWT produces a matrix of coefficients that are arranged and plotted on a spectrogram. The abscissa represents frequency while the ordinate represents time. The higher values on the spectrogram correspond to the dominant frequency components present in the signal over time.

To illustrate the use of the Continuous Wavelet Transform (CWT), the same braking curve from Figure 3.1 is employed. The spectrogram of the traction wheel speed curve with the first IMFs is shown in Figure 3.5. The areas of maximum amplitude are represented by yellow color, while the regions of minimum are represented by blue color.

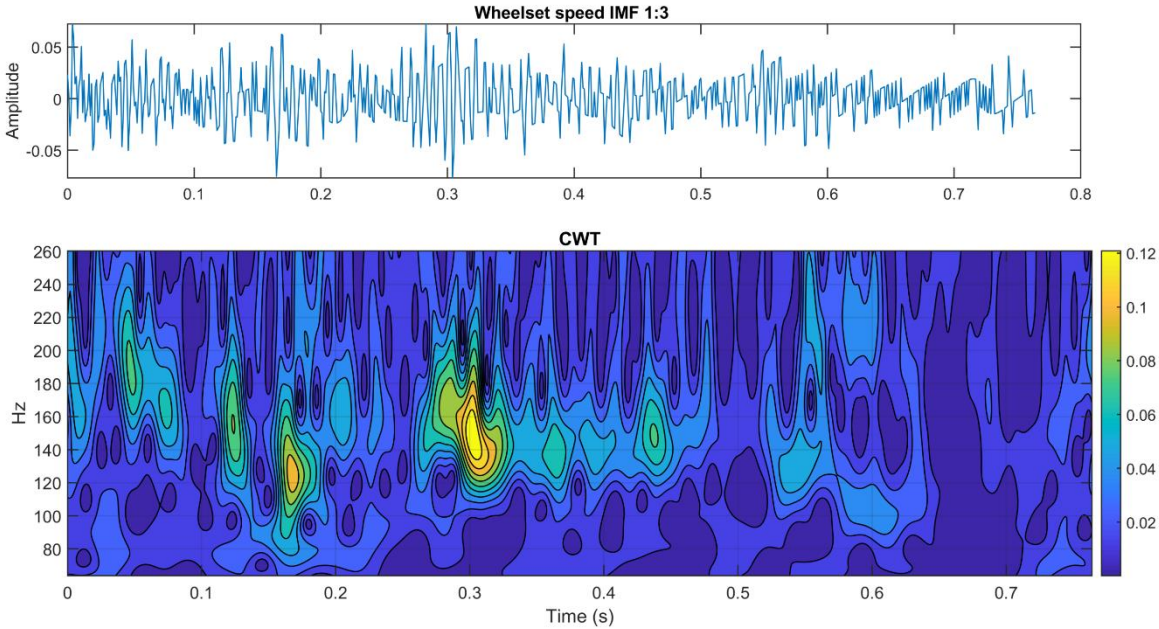


Figure 3.5 Spectrogram plot of the first three IMFs of the braking curve computed using CWT. It must be observed that the resulting frequencies are identical to those found in the FFT spectrum.

When compared to the FFT analysis, the results obtained reveal the frequency components present at all times throughout the signal. It is clear that the wheel vibrates at a lower frequency after the principal component of 144 Hz appears at $t = 0.3$ s.

3.2.4 Proposed correlation method

The proposed method enables the visualization of tangential force transfer from wheels to vehicle. The correlation method uses the results of the CWT applied to the vibration signals of the wheel and the vehicle to identify time-frequency coincidences in both dynamics. The comparisons are as follows: longitudinal acceleration-

wheelset speed ($ax-ws$), lateral acceleration-wheelset speed ($ay-ws$), and vertical acceleration-wheelset speed ($az-ws$).

Figure 3.6 is a diagram of the proposed correlation method. Figure 3.6a is a spectrogram depicting vehicle dynamics with frequencies detected at times t_1 and t_2 , while Figure 3.6b is a spectrogram depicting wheel dynamics with frequencies detected at times t_1 and t_2 . By superimposing the two spectrograms, as depicted in Figure 3.6c, it is possible to identify coincidence zones, denoted by darker areas. Only the biggest coincidence zones are displayed in the final spectrogram, Figure 3.6d. If the CWT images of the wheel and vehicle are identical at any time and frequency, tangential forces have an impact on the vehicle.

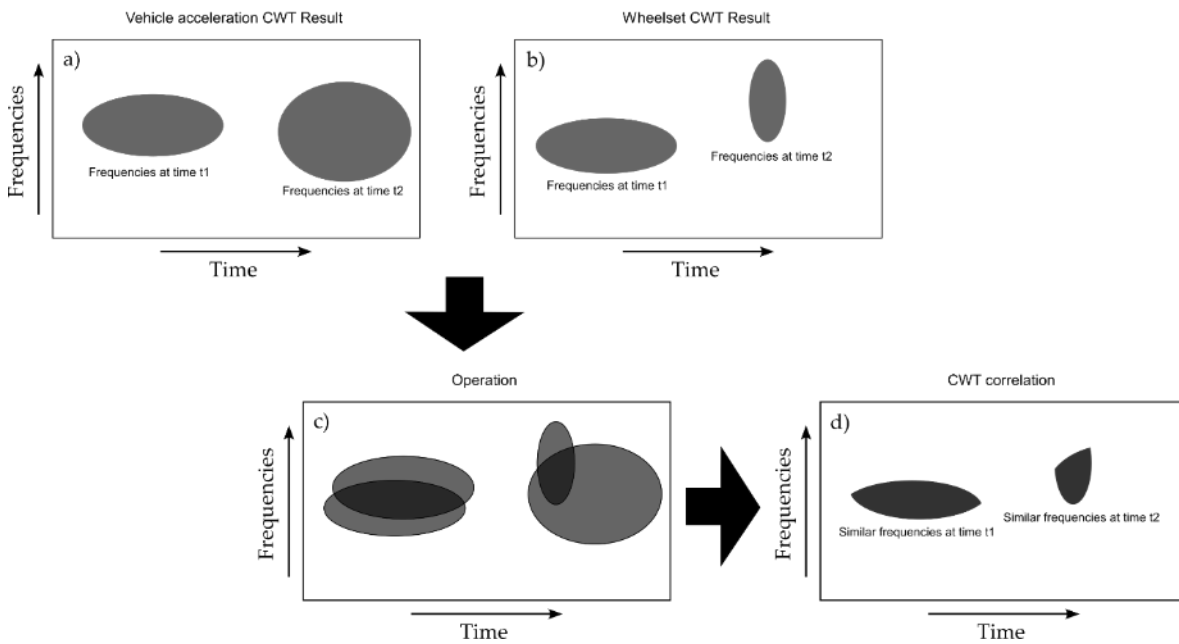


Figure 3.6 The proposed correlation method algorithm. The method described by equations 3.10 to 3.16 is applied to each signal's CWT output. The common frequency components in time are solid proof that the tangential forces of the wheel influence the dynamic response of the vehicle.

In Figure 3.6c, the coincidence of the interval t_1 is more pronounced because the frequency is clearer and the duration is longer. On the other hand, the coincidence of the t_2 interval is not a useful correlation, as its frequency is difficult to define and its duration quite brief.

The traction wheel speed CWT results are contained in the array E with elements $e_{a,b}$, while the acceleration results are contained in the arrays A_x , A_y , and A_z with

elements $ax_{a,b}$, $ay_{a,b}$ and $az_{a,b}$, respectively. An intermediate operation is used to consider only the most significant frequency components (those with the highest amplitude). To accomplish this, we only consider values that are greater than a default value, such as the mean. Consequently, the subsequent conditions apply:

$$ax'_{a,b} = \begin{cases} ax_{a,b}, & ax_{a,b} \geq u_{ax} \\ 0, & ax_{a,b} < u_{ax} \end{cases} \quad (3.10)$$

$$ay'_{a,b} = \begin{cases} ay_{a,b}, & ay_{a,b} \geq u_{ay} \\ 0, & ay_{a,b} < u_{ay} \end{cases} \quad (3.11)$$

$$az'_{a,b} = \begin{cases} az_{a,b}, & az_{a,b} \geq u_{az} \\ 0, & az_{a,b} < u_{az} \end{cases} \quad (3.12)$$

$$e'_{a,b} = \begin{cases} e_{a,b}, & e_{a,b} \geq u_e \\ 0, & e_{a,b} < u_e \end{cases} \quad (3.13)$$

where the minimum threshold values are denoted by u_{ax} , u_{ay} , u_{az} and u_e . The components of the correlation matrices for the three directions are as follows:

$$c_{xi,j} = a'_{xi,j} \times e'_{i,j} \quad (3.14)$$

$$c_{yi,j} = a'_{yi,j} \times e'_{i,j} \quad (3.15)$$

$$c_{zi,j} = a'_{zi,j} \times e'_{i,j} \quad (3.16)$$

The correlation between both signals in frequency and time is represented by the set of nonzero-valued elements $c_{xi,j}$, $c_{yi,j}$ and $c_{zi,j}$.

Figure 3.7 illustrates an application of the proposed correlation method. In this case, the wheel speed signal is compared with the longitudinal vehicle-body acceleration signal. The outcome clearly illustrates the frequencies and times at which both signals match.

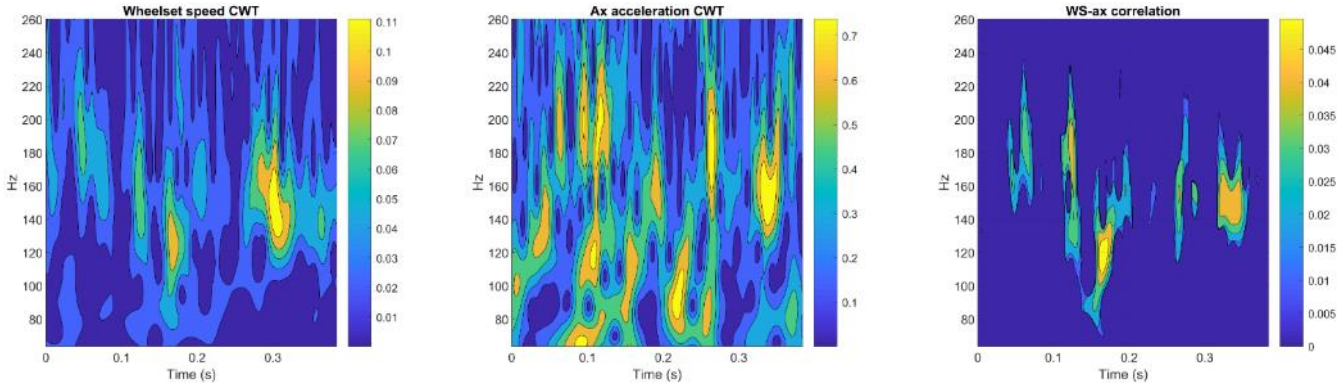


Figure 3.7 Example of method proposed correlation method. The wheel's vibration signal is compared to the vehicle's vibration signal in the longitudinal direction. Time and frequency matches are displayed on a spectrogram, with the greatest coincidences having the largest amplitudes.

4 Methodology

This section describes the procedures used to conduct the experimental braking tests on the scale-down rail vehicle. It begins with a description of the scale-train test bench and continues with a detailed explanation of the methodology's steps.

4.1 Test Bench Description

4.1.1 The scaled-down railway vehicle

The test rail vehicle is a single wagon supported by two bogie wheels, with the rear bogie providing torque and traction. The vehicle was designed at a 1:20 scale reduction. On clean roads, the vehicle can reach its top speed of 1.3 m/s in three seconds, propelled by a servomotor coupled via belt transmission to the drive axle. The vehicle's body is attached to the bogies by means of a secondary suspension consisting of eight springs. In the vehicle's middle section are the motor control circuits, sensors, and data storage. In Table 4.1, the primary vehicle parameters are detailed. Figure 4.2 depicts the vehicle mounted on the test bench's rails.

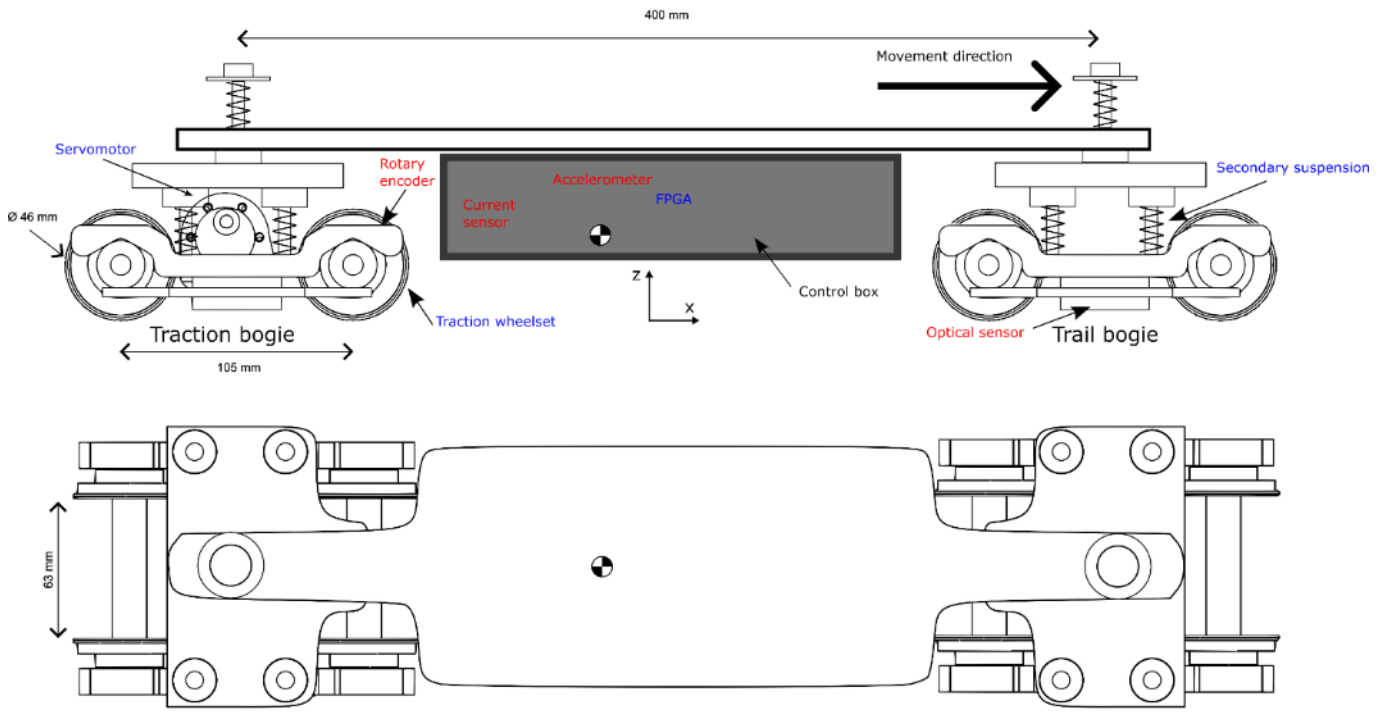


Figure 4.1 Dimensions and major components of the model vehicle used in the experiments, as seen from both a lateral and an aerial perspective.

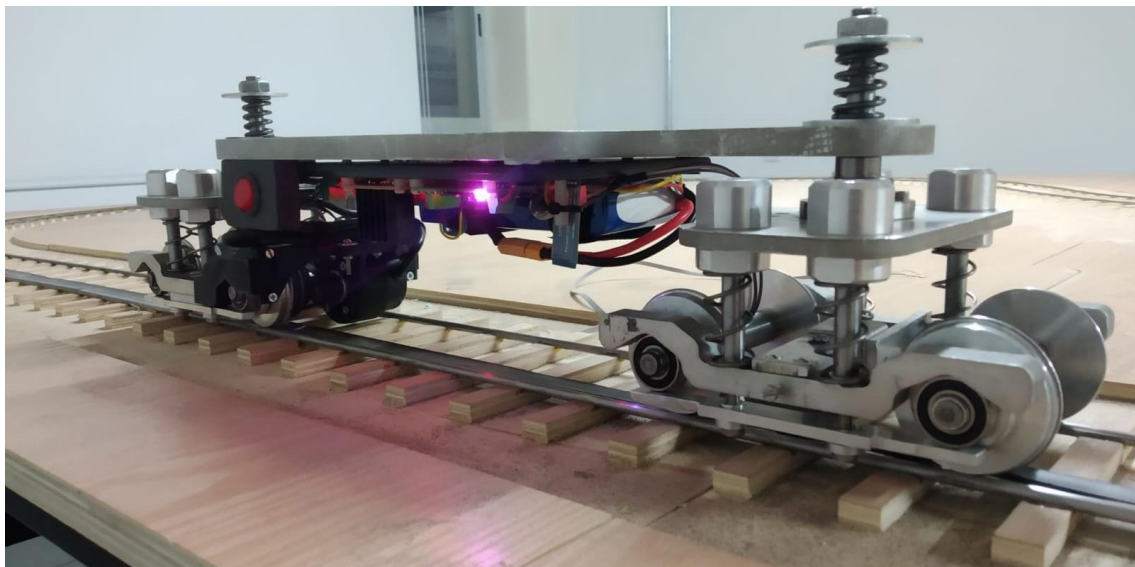


Figure 4.2 The vehicle positioned on the test bench's rails.

Table 4.1 Principal parameters of the scaled vehicle

Parameter	Value
Mass	
• Total mass	4.4 kg
• Traction Bogie	1.0 kg
• Trail Bogie	0.64 kg
• Vehicle body	2.76 kg
Dimensions	
• Full length	506 mm
• Total height	100 mm
• Overall width	120 mm
• Wheel radius	23 mm
Suspension	5.82 N/mm
Center of mass	x: -42 mm
• (Measured from the reference frame)	y: 0 mm z: 62 mm

4.1.2 Test bench

The test bench, on which the railcar vehicle experiments are conducted, is a horizontal β -shaped closed-circuit track. Figure 4.3 depicts a general perspective of the table, which measures 2.36 x 5.68 x 0.92 m (width x length x height). The body of the table is a steel structure with plywood sheets on the surface; it has levelers on the bottom to set the level. As shown in Figure 4.4a, the track sleepers are CNC-machined into the surface of the plywood sheet. Figure 4.4b depicts the dimensions of the rails and sleepers. The rails are 5 mm-diameter steel wires with a round profile that are mounted in longitudinal grooves on the sleepers using epoxy resin.



Figure 4.3 Panoramic view of the test bench table. The track is a β -shaped closed loop.

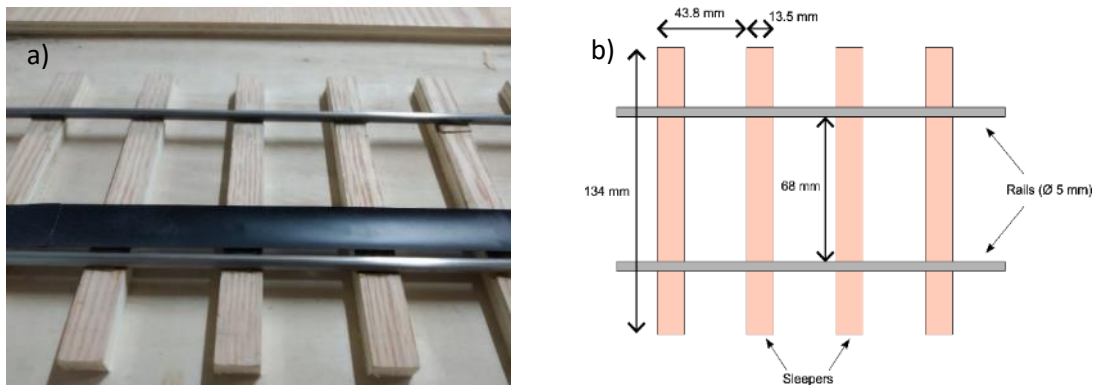


Figure 4.4 a) Detailed view of the test bench rails; b) track dimensions.

4.1.3 Data acquisition system

The monitoring and control system for the vehicle is comprised of an FPGA board, vibration sensors, and a servo motor. The FPGA board receives control instructions and settings to drive the vehicle from a Bluetooth module and stores the measured data on a micro-SD card. The FPGA has an embedded 16-bit microcontroller with RISC architecture and a proprietary instruction set. It features two caches, one for 1kB of data and the other for 1kB of instructions, as well as external memory interfaces for 1MB of data and 128kB of instructions. A 16MB flash memory is included for storing user data, processor firmware, and FPGA configuration. The

processor is equipped with a 32-bit single-precision floating-point unit, a direct memory access (DMA) unit, an interrupt handler, four timers, and a watchdog timer. There are also FFT and PID controller modules implemented within the microcontroller. It has multiple communication interfaces, including USB, UART, SPI, I2C, RS485 and SD, which are used to communicate with the board's sensors, including MEMS sensors (Accelerometer, Gyroscope, Magnetometer) and converters (ADC, DAC). C language is used to program microcontrollers with a set of tools designed to compile, program, and verify the embedded processor's proprietary instruction set. For more information about this board, see Cureño et al (2023) and Clemente et al (2022).

The accelerometers used for monitoring vehicle vibrations are contained within the control box. The speed of the traction wheel is measured by a 600-pulse-per-revolution incremental rotary encoder installed on the drive bogie, while the speed of the vehicle is measured by an optical sensor mounted on the other (trailed) bogie; see Figures 4.5 and 4.6. The traction-wheel speed signal is also used to detect the vibrations in the wheel during the test. The characteristics of the principal components of the data acquisition system is presented in Table 4.2.

Table 4.2 *Principal technical features of the components of the acquisition system.*

Component	Features
Accelerometer	3 axis, MEMS sensor, model LSM6DS3, $\pm 4G$
Gyroscope	3 axis, MEMS sensor, model LSM6DS3, ± 143 °/s
Optical sensor	IR Sensor, model TCRT5000
Rotary encoder	600 ppr, model DC5-24V 600.
Control board	DUA, Spartan 3.
Bluetooth module	Bluetooth UART RS232, model HC-05.
Current sensor	Hall effect, Model ACS712
LiPo battery	4000 mAh, 14.8 V

Servomotor	Pololu 37D con motorreductor, motor DC 12 V, 5.5 A y 12W. Gear ratio 19:1 Max speed 530 RPM; 8.5 kg-cm torque.
Servomotor driver	H bridge, model L298N, 2 A, 30 V

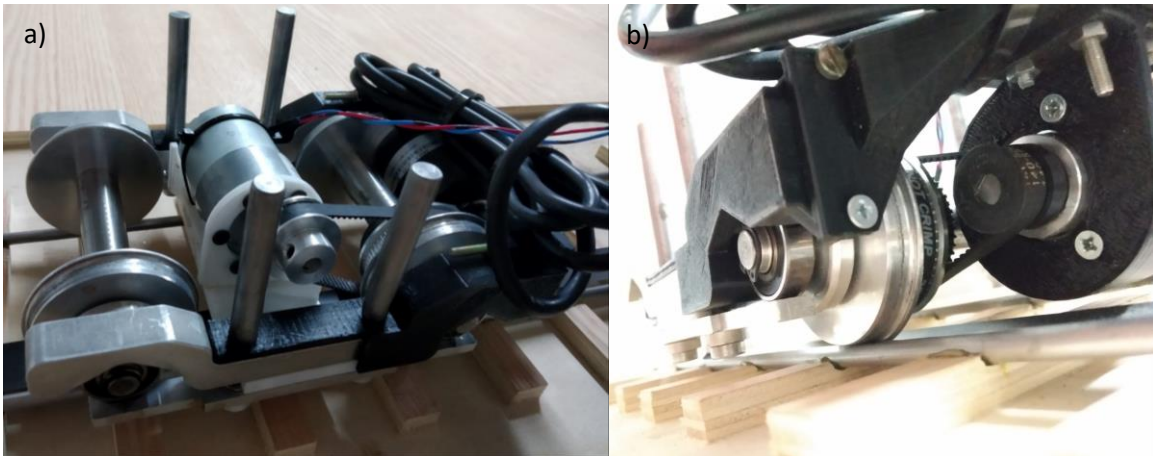


Figure 4.5 Traction bogie. a) Top view, showing the DC motor coupled to the traction wheel via a transmission timing belt with a 19:1 ratio. b) Bottom side view, showing the incremental encoder connected to the traction wheel, also via timing belt transmission. The motor and encoder supports were 3D printed.

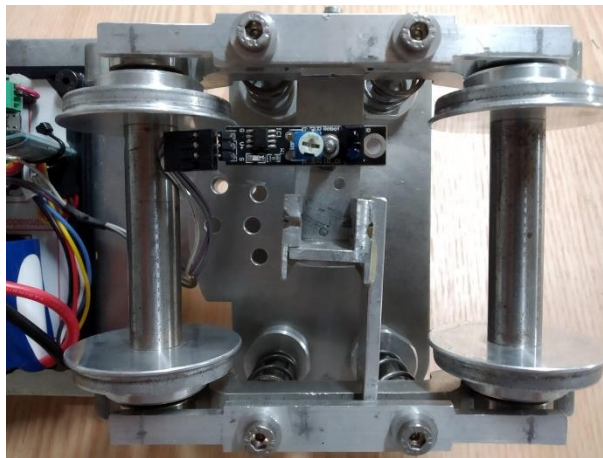


Figure 4.6 Bottom view of the trail bogie, showing the optical sensor. The sensor employs an infrared sensor that is sensitive to black and white contrast. To measure speed with this sensor, a tape with black-white areas is required, as shown in Figure 4.9.

Figure 4.7 depicts the installation of the acquisition system modules inside the vehicle's control box. A sensor connected to the power input of the motor driver

measures current consumption. A 14.8 V Li-Po battery powers the entire system. Figure 4.7 shows the control system interconnections.

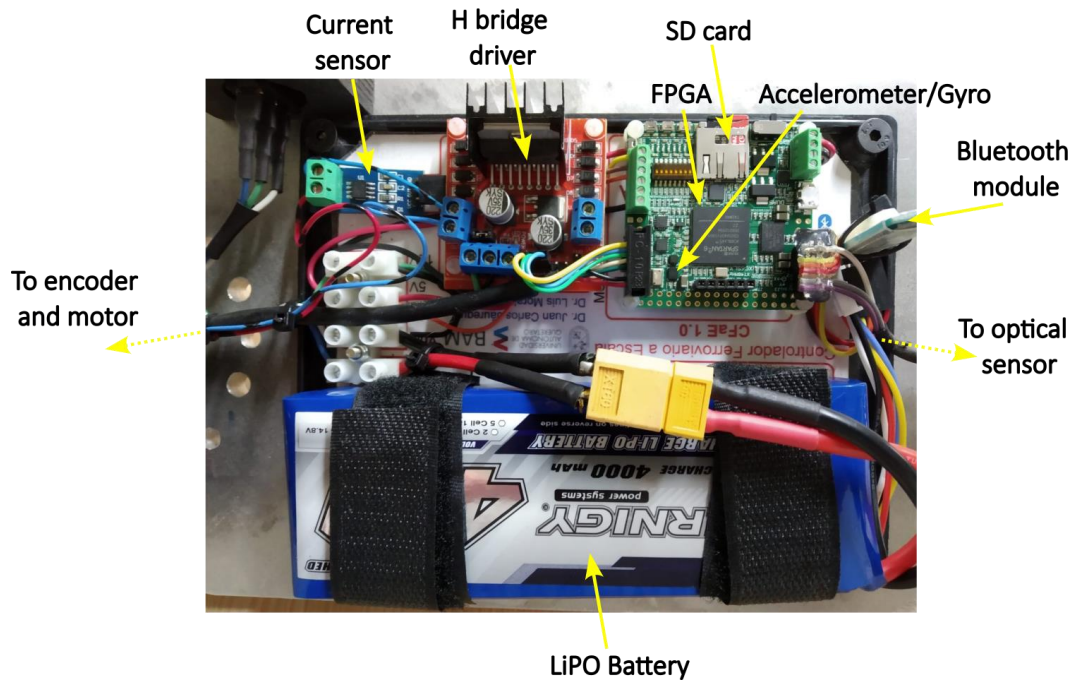


Figure 4.7 The acquisition system components inside the vehicle's control box.

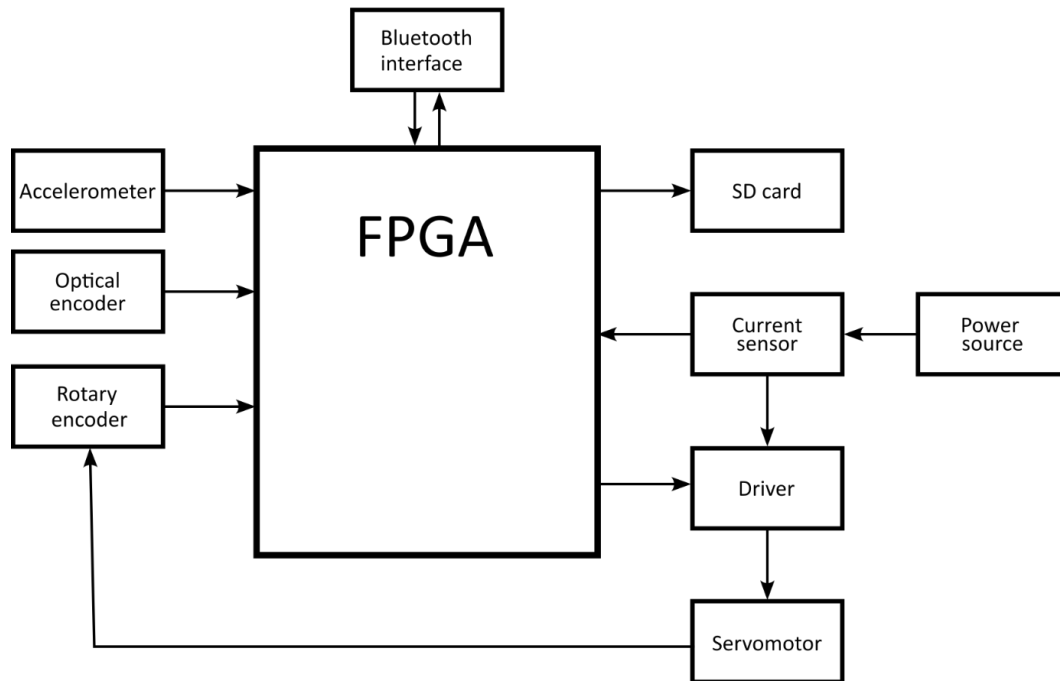


Figure 4.8 Schematic of the principal control and data acquisition modules of the vehicle. Arrows pointing toward the FPGA represent the direction of information flow from the sensors, whereas arrows pointing away from the FPGA represent control signals and data.

4.2 Methodology

In the railcar vehicle's braking tests, the coefficient of friction between the wheel and the rail was varied in order to see the changes in the vibrations of the vehicle's body caused by wheel's tangential forces. Experiments were conducted with and without braking the vehicle. The rotary encoder signal was used to detect wheel vibrations, while accelerometers were used to detect vehicle vibrations. When the coefficient of friction is high, tangential forces are amplified and transmitted throughout the vehicle's body.

The subsequent section describes in detail how the experiments were conducted and how the data was analyzed in order to measure the level of vibration at low and high coefficients of friction and to establish a correlation between the vibrations of the vehicle and the tangential forces on the wheel.

4.2.1 Experiment overview

The experiment consists of driving the vehicle to its top speed and collecting vibration samples with the sensors. The velocity of the wheel, the vehicle, and the motor's current consumption are also measured. At each run of the vehicle, data was collected before and during the braking test in order to have samples of both situations and learn more about the mechanism of tangential force transfer to the vehicle's body. The coefficient of friction between the rails differs in each experiment. This is accomplished with the friction modifiers described below.

4.2.1.1 Friction modifiers.

The tests are conducted on both clean and friction-modified rails. In the clean rail test, both the rails and the wheels are cleaned with gauze soaked in thinner to remove dust and grease residues, see Figure 4.10. In the other tests, friction modifiers were directly applied to the rails. The coefficient of friction between the wheel and clean rails is 0.2, while the values for friction-modified rails are as follows:

- Grease. To provide a coefficient of friction of less than 0.1, solder paste was used as the lubricant.
- Soap. A thin coating of liquid dish soap is applied. Soap dries rapidly, resulting in a coefficient of 0.25.

- Sand. Sand dust (very fine grains) is used to increase the coefficient of friction on the rails to 0.45, as shown in Figure 4.11.

As depicted in Figure 4.9, friction coefficients were measured using a dynamometer and the following formula:

$$\mu = \frac{P}{4F_f} \quad (4.1)$$

where P is the total weight of the vehicle and F_f is the static friction force measured with the dynamometer

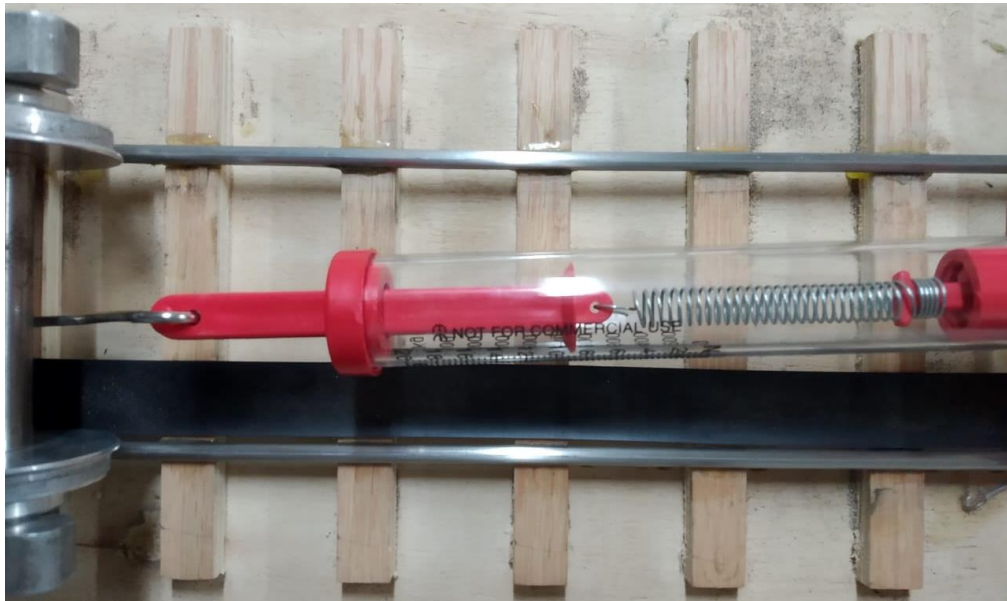


Figure 4.9 A dynamometer used to determine the coefficient of static friction resulting from the application of each friction modifier. At this measurement, the drive wheel is locked to pull the vehicle while measuring the resistance force (F_f). The dynamometer scale indicates the force required to move the vehicle from the rest.

The friction modifiers used in the tests replicate the environmental conditions found on real track rails. Soap has been used in other works (Bosso, 2019) to simulate leaf contamination, and sand is used to facilitate starting and prevent wheel slippage on contaminated and wet rails by increasing the coefficient of friction.



Figure 4.10 Clean rails. Wheels and rails were cleaned to remove any traces of contamination.



Figure 4.11 Sand-scattered rails. The sand was spread across the entire braking zone.

4.2.1.2 Experiment matrix

In each experiment, ten runs were conducted to collect data before and during braking. Table 4.3 provides a summary of all the tests carried out on clean and friction-modified rails.

Table 4.3 *Experiment Matrix.*

Friction modifiers	Rail friction	No brake/Brake	Quantity
Grease	Low (0.1)	NB	7
		B	7
Clean	Medium (0.2)	NB	7
		B	7
Soap	High (0.3)	NB	7
		B	7
Sand	Very high (0.45)	NB	7
		B	7

4.2.2 Braking Experiments

Experiments were conducted on the track's straight section. In this section of the table, the vehicle is accelerated to 1.3 m/s and then decelerated 2.5 m later in an area chosen for its lack of rail disturbances. There should be no major disruptions on the tracks, as this would make it harder to analyze vibrations and the forces involved in braking. Following the steps outlined in this section, the experiments are conducted to collect the vibration data with and without braking.

All experiments were conducted in the same area and at the same speed to reduce the number of variables. To accomplish this, the vehicle must automatically brake using a flag as a stop signal. In addition to measuring the vehicle's speed, the optical sensor was also used to send the braking signal to the control board. A zebra-striped tape was placed in the designated stopping area to serve as both a braking flag and a speed sensor, see Figure 4.12. Installed below the trailed bogie, the optical sensor emits the first pulse when passing over the first white of the zebra tape, thereby indicating the vehicle to brake. Then, during braking, the optical sensor's successive pulses are used to measure speed.

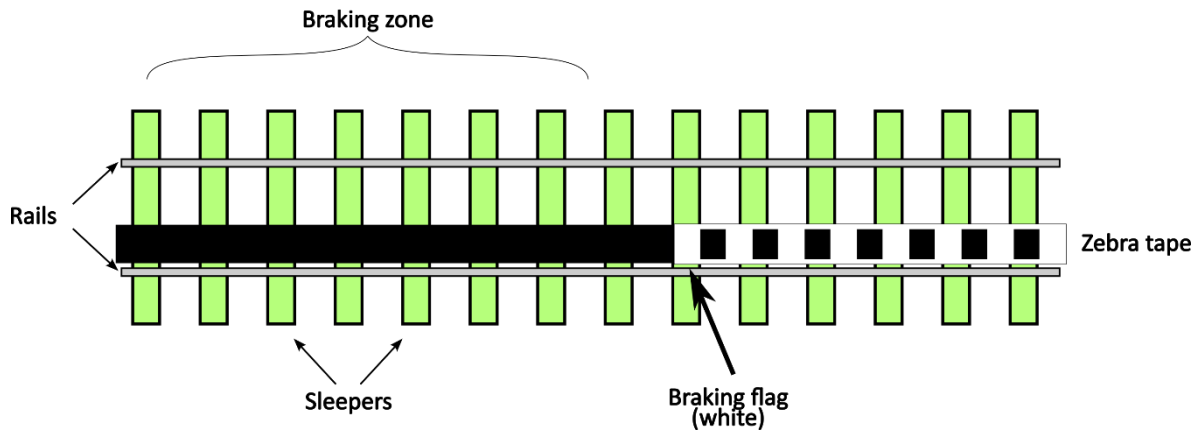


Figure 4.12 Braking zone diagram. Zebra tape is used to measure the vehicle speed. The first white of the zebra works as the braking flag.

Figure 4.13 depicts the initial position of the vehicle, while Figure 4.14 depicts an aerial view of the experimental section. A black tape was placed before the braking zone just below the speed sensor to prevent the vehicle from decelerating.



Figure 4.13 Position of the test vehicle before the start of the experiment. To prevent the optical sensor from activating before the braking zone, a black tape was placed over the track.



Figure 4.14 The area where braking experiments are conducted; approximately 2.5 meters long, from the curve to the center of the test bench.

An application on the cell phone is used to send Bluetooth instructions to the rail vehicle in order to operate it. Table 4.4 provides an overview of the vehicle's commands.

Commands can be sent on a single line separated by a space; for instance, the command **R1 T5 S127** specifies forward motion with a maximum final speed and an acceleration time of 5 seconds.

Table 4.4 The instructions used to operate the vehicle. These commands are transmitted from any serial Bluetooth application installed on a cell phone and linked to the Bluetooth module of the vehicle.

Instruction	Description	Example
R0	Move forward	R0
R1	Move backwards	R1
R3	Stop	R3
S	Maximum speed	S1-S127
T	Acceleration time	T1-T10
G1	Start data recording	G1
G2	Stop data recording	G2
G3	Eject SD memory	G3
F0	Automatic braking (Based on optical sensor)	F0
F1	manual braking	F1

When the vehicle comes to a full stop, it is prompted to stop recording data in order to conclude the test, see Figure 4.15. Each test's stopping distance is different because it is determined by the rail's friction modifier.

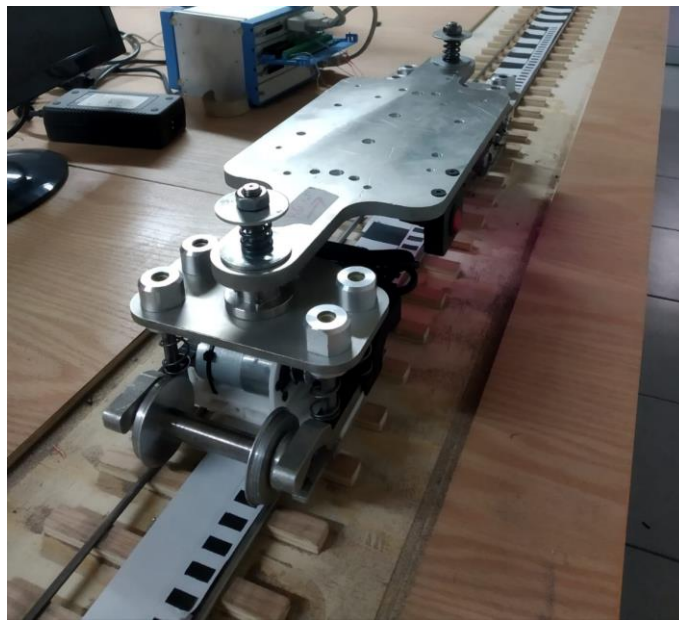


Figure 4.15 Photograph of the vehicle completely stopped in the braking zone.

In conclusion, Figure 4.16 depicts the typical sequence used in each experiment. Table 4.3 provides a summary of the friction modifiers employed in each experiment. The principal steps are as follows:

1. Apply the friction modifier in the braking area.
2. Place the vehicle in the starting position (2.5 m from the braking zone), making sure the wheels are well aligned on the rails and that it is over the black tape.
3. Data save (G1) and automatic braking (F0) commands are sent.
4. The forward acceleration commands are sent, with the maximum final speed and a 5 second acceleration (R0 T5 S127).
5. The vehicle is expected to accelerate and brake automatically in the braking zone.
6. When the vehicle comes to a complete stop, (G2) is sent to stop data recording.
7. The vehicle is returned to its starting position, and the procedure is repeated from step 2 until all ten repetitions are finished.
8. At the end of all experiments, the command (G3) must be sent to eject the SD-card.
9. Finally, the vibration data is analyzed in the time and frequency domains, as explained in the following section.

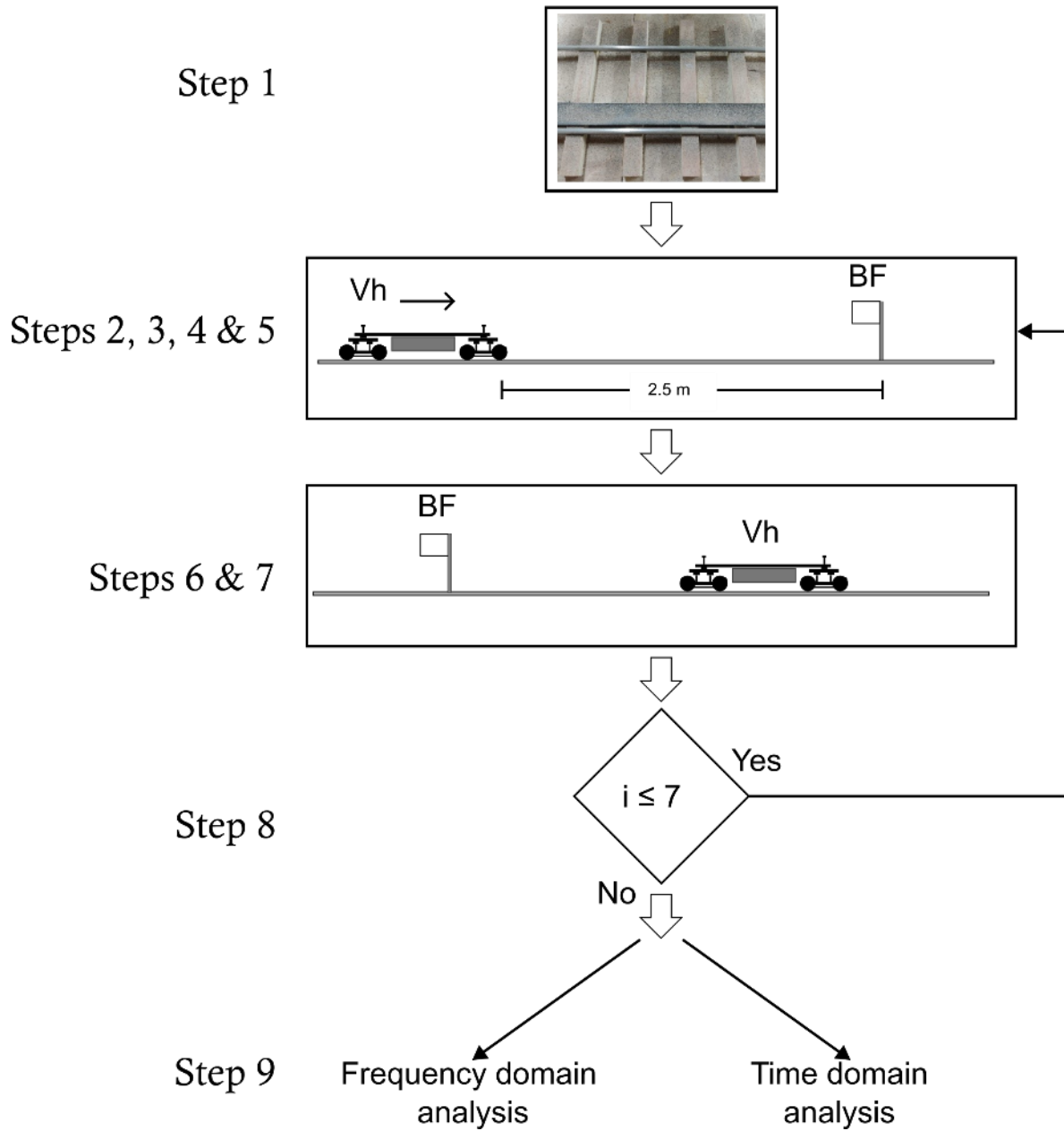


Figure 4.16 The primary procedures that were utilized throughout each experiment. *Vh*, for Vehicle; *BF*, for Braking Flag.

4.2.3 Vibration analysis

The vibration signals captured during testing are analyzed in the time domain and frequency domain. The methods described in section 3.1 are used to detect variations in the amplitudes of vehicle vibrations in the time domain prior to and during braking. The objective is to identify the index that most accurately represents

the variation in the coefficient of friction of the wheels. The flowchart that was followed in this analysis over time is depicted in Figure 4.17.

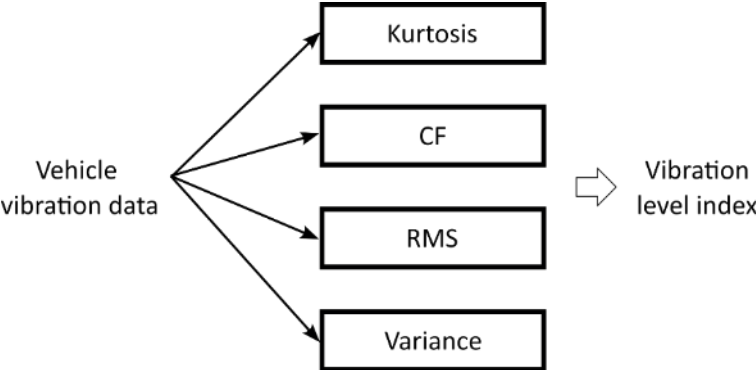


Figure 4.17 The process for analyzing the vibrational signals in the time domain.

Additionally, the same data is analyzed in the frequency domain to demonstrate the effect of tangential forces on the vehicle’s dynamics. Empirical Mode Decomposition (EMD), Fast Fourier Transform (FFT), Continuous Wavelet Transform (CWT), as well as a proposed correlation method, are employed for this purpose. Figure 4.18 depicts the analysis of wheel and vehicle vibration signals applying the methods outlined in Section 3.2.

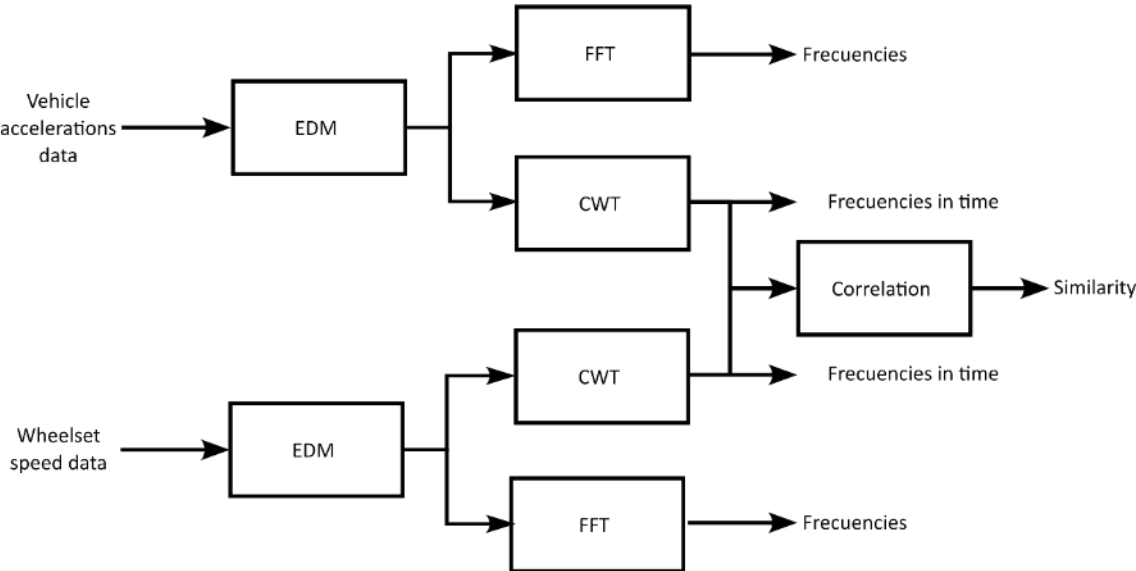


Figure 4.18 The process for analyzing the frequencies of vibrational signals. The first step is to apply EMD to eliminate non-useful signal characteristics (such as extremely low frequencies). The FFT and CWT are used to extract the signal’s frequencies, and the proposed correlation method compares the extracted frequencies to find time and frequency similarities.

FFT is a widely used technique for identifying the frequency components of vibration signals. CWT is also a technique to identify the frequencies of a signal and their positions over time. The FFT is used in this study to investigate how the different friction coefficients affect the vehicle's vibration modes and to determine the frequencies that are shared by both the vehicle's and the wheel's dynamics.

In addition to determining the frequencies of the signals over time, the CWT coefficients are used to compare the vehicle's and the wheel's vibration signals using the proposed correlation method. The purpose of this comparison is to find similarities between both signals that allow us to verify that what we see in the vehicle's vibration signals is actually caused by tangential forces of the wheels. The comparison is easier to make in the frequency domain.

5 Results and discussion

This chapter presents the results of the braking tests outlined in the previous chapter. First, the vibration responses are displayed in the time domain, demonstrating that there is a significant change in vibration level when the wheel-rail coefficient of friction is modified. In the preceding section, statistical techniques are used to analyze the vibration signals in order to determine the most effective method for characterizing the coefficient of friction.

The study concludes by comparing the outcomes of the lower and higher coefficients of friction on the rails, pointing out the impact of the coefficient of friction on vehicle dynamics when it is increased. The frequency-domain comparison is performed with the use of the Fast Fourier Transform (FFT), the Discrete Wavelet Transform (DWT), and the proposed correlation method.

5.1 Time domain analysis

This section presents the time response charts showing the accelerations of the vehicle in the longitudinal ax , lateral ay and vertical az directions, as well as the vehicle's rotations in roll gx , pitch gy and yaw gz . In addition, the velocity of the drive

wheel and the vehicle's velocity are included in the charts to illustrate how vibrations change between braked and no brake states. The outcomes of applying kurtosis, RMS, variance, and crest factor to the signals of the vehicle dynamics (ax , ay , az , gx , gy y gz) are presented at the end of this section.

5.1.1 Vibration responses over time

Rails that are lubricated with grease exhibit the lowest coefficient of friction, which is less than 0.1. The accelerations and rotations of the vehicle in the three directions are depicted in Figure 5.1. The graph's response time ranges from $t = -1 s$ to $t = 2.7 s$, with $t = 0 s$ denoting the moment the vehicle brakes, to demonstrate the amplitude of vibrations both before and after braking.

The same Figure 5.1 also depicts the behavior over time of the wheel's and vehicle's speeds. The black line depicts the tangential velocity of the wheel w_s , while the red line, which appears after $t = 0$, depicts the vehicle's velocity V ; the vertical red lines indicate the beginning and end of the vehicle's braking state. The pulses from the optical sensor are represented by the blue lines, which separate as the vehicle slows down. The behavior of both speeds, which is described in detail in the following section, is quite distinct in both components and provides a graphical representation of how the wheel slides along the rail. In this case, the wheel's braking speed drops instantly to 0.25 m/s, whereas the vehicle's speed decrease is more gradual.

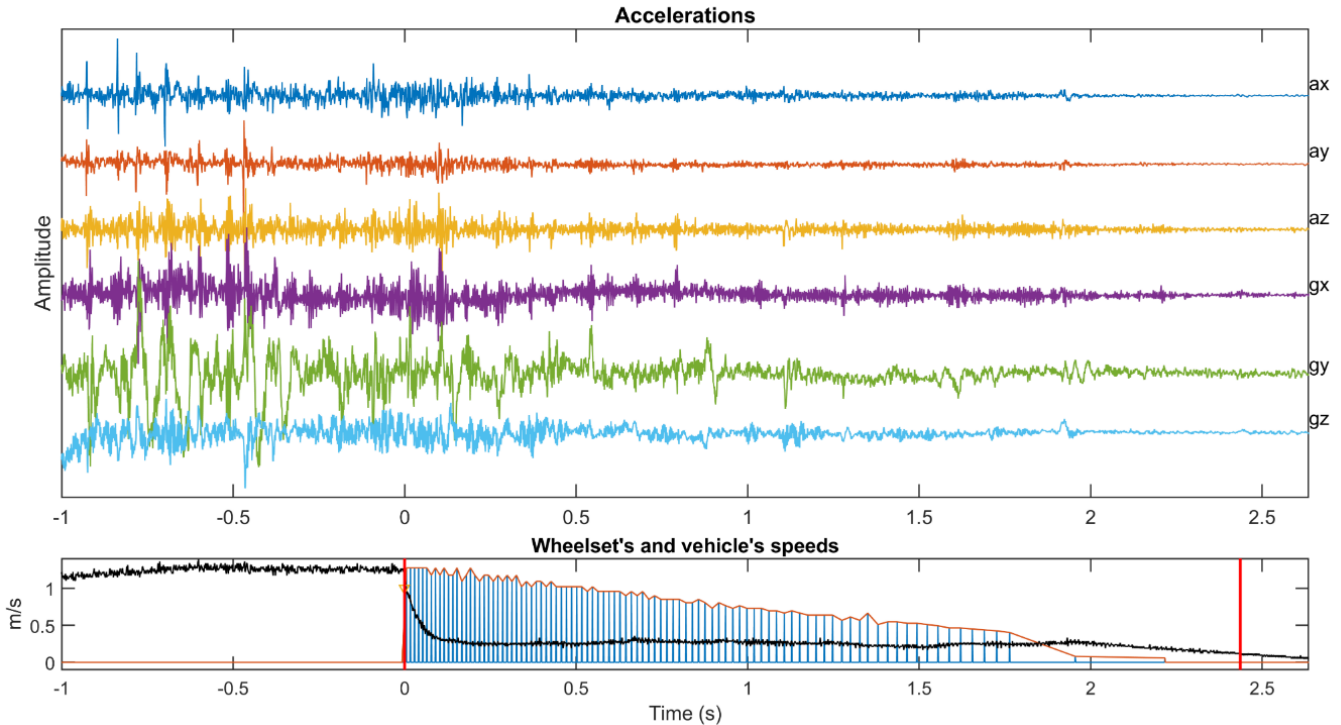


Figure 5.1 Time response of vehicle vibrations on greased rails in all three directions and rotations, before and during braking. Additionally, wheel and vehicle speeds are displayed. When braking, the tangential velocity of the wheel is reduced up to 0.25 m/s instantly, while the vehicle's speed is reduced gradually.

Pulses of high amplitude in the signals are caused by wheel collisions at rail joints. In the case of low-friction rails, the duration of these high amplitudes is extremely brief. However, if the rails have a high coefficient of friction, these high amplitudes are maintained for a longer period of time, as will be seen in the following section.

When both the rail and the wheel are clean, the coefficient of friction is 0.2. Figure 5.2 depicts the accelerations and rotations of the vehicle, as well as the wheel and vehicle speeds. In this case, the vibrations are different than when the rails are lubricated. In the case of greased rails, impacts are immediately absorbed, which is not the case with clean rails. Compared to greased rails, the vehicle requires slightly less time to stop (2.5 seconds) when using clean rails. Despite the fact that the wheel's speed decrease is greater (0.2 m/s during the first 0.5 seconds). The time it takes for the vehicle to come to full stop is 2.15 seconds.

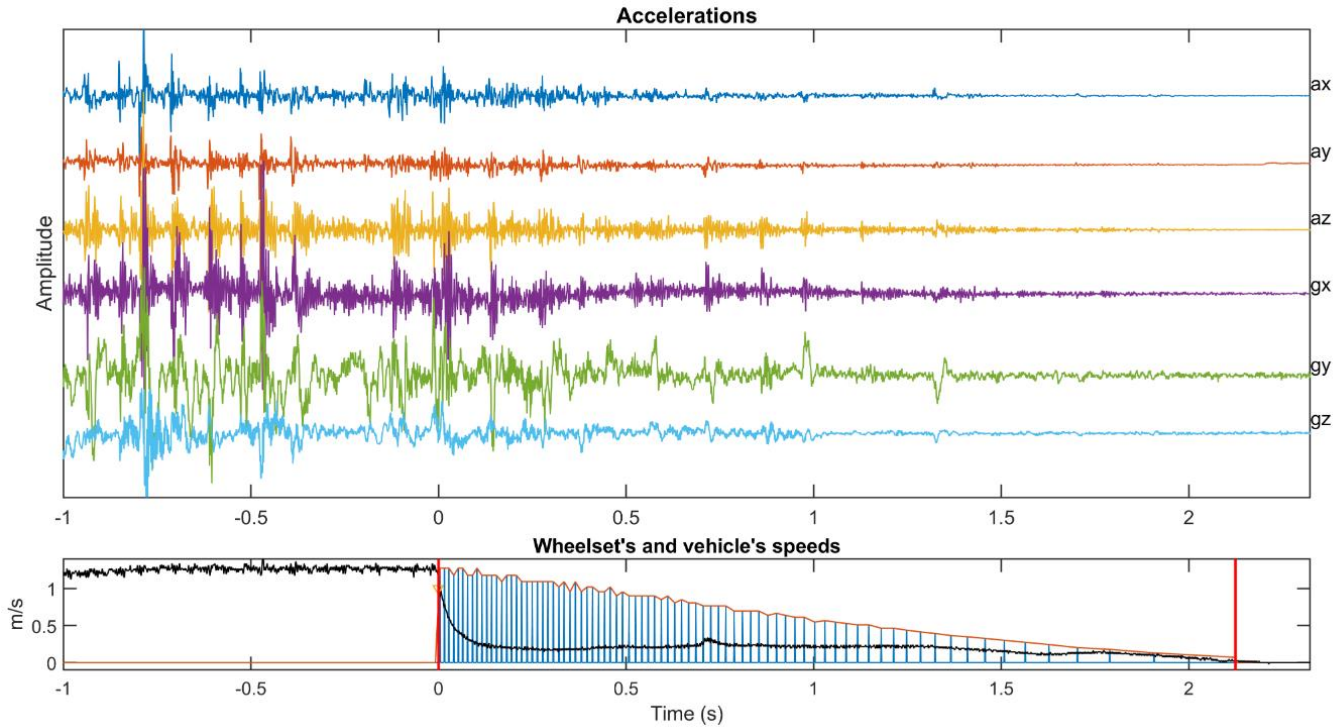


Figure 5.2 Time response of the vehicle vibrations in all three directions and rotations, before and during braking, on clean rails. Wheel and vehicle speeds are also displayed.

The soap also dampens the rails' impact, but the vehicle vibrations have increased. The soap reduced the braking time to 1.7 seconds by slightly increasing the coefficient of friction to 0.25. When braking, the wheel speed reduced to 0.38 m/s. In addition, the chart of speeds shows that after 0.75 s, the speeds of the vehicle and the wheel are identical. This means that the slip is nearly zero from then on.

The use of soap was meant to reduce the impact of friction, but the opposite happened. The fluid dried into a residue that provided more friction against the traction wheel's rotation.

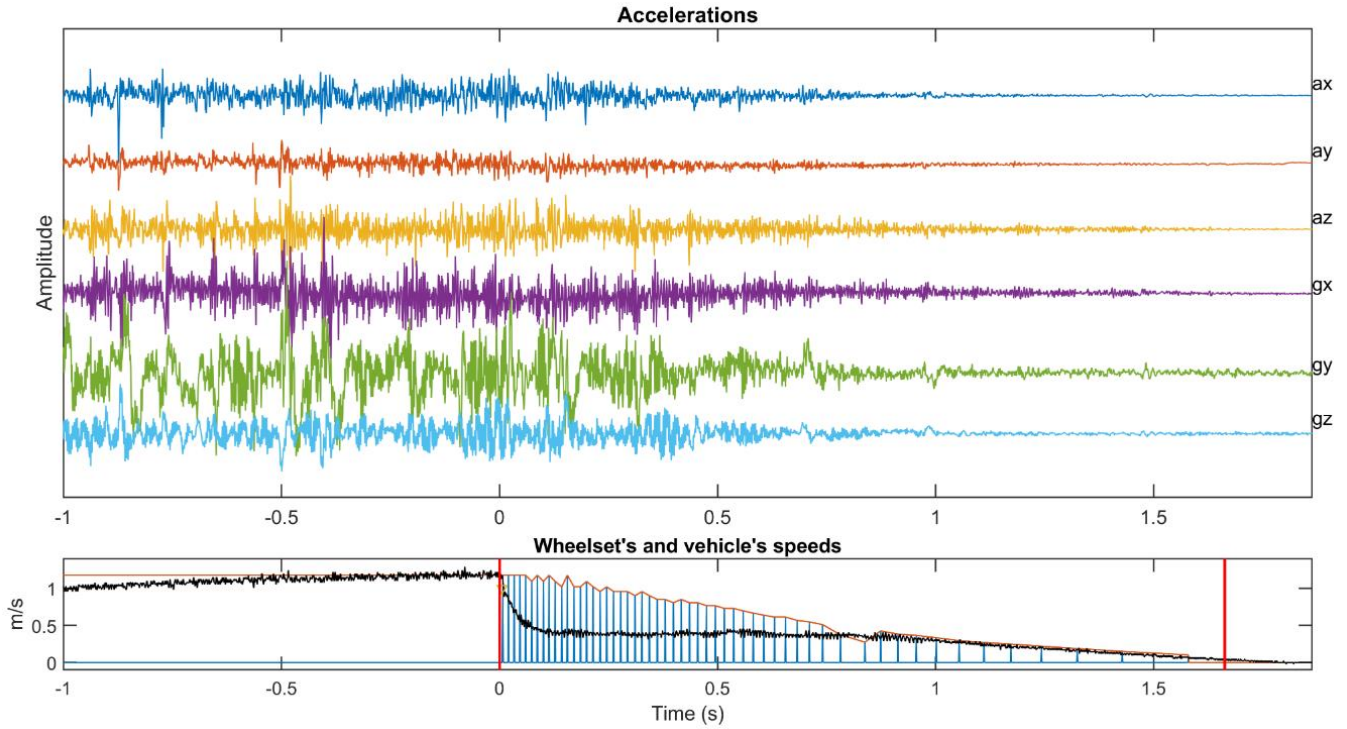


Figure 5.3 Time response of the vehicle vibrations in all three directions and rotations, before and during braking, on soap-coated rails. Wheel and vehicle speeds are also displayed.

With the highest coefficient of friction (0.45), the vehicle's dynamics have been drastically changed compared to previous cases. Clearly, the sand grains' impacts amplified the vehicle's vibrations in all directions. The wheel speed during braking is reduced to 0.5 m/s, and the braking time is 1.2 seconds. At nearly half the braking time ($t = 0.5$ s), both speeds are identical, indicating that the sliding time is short.

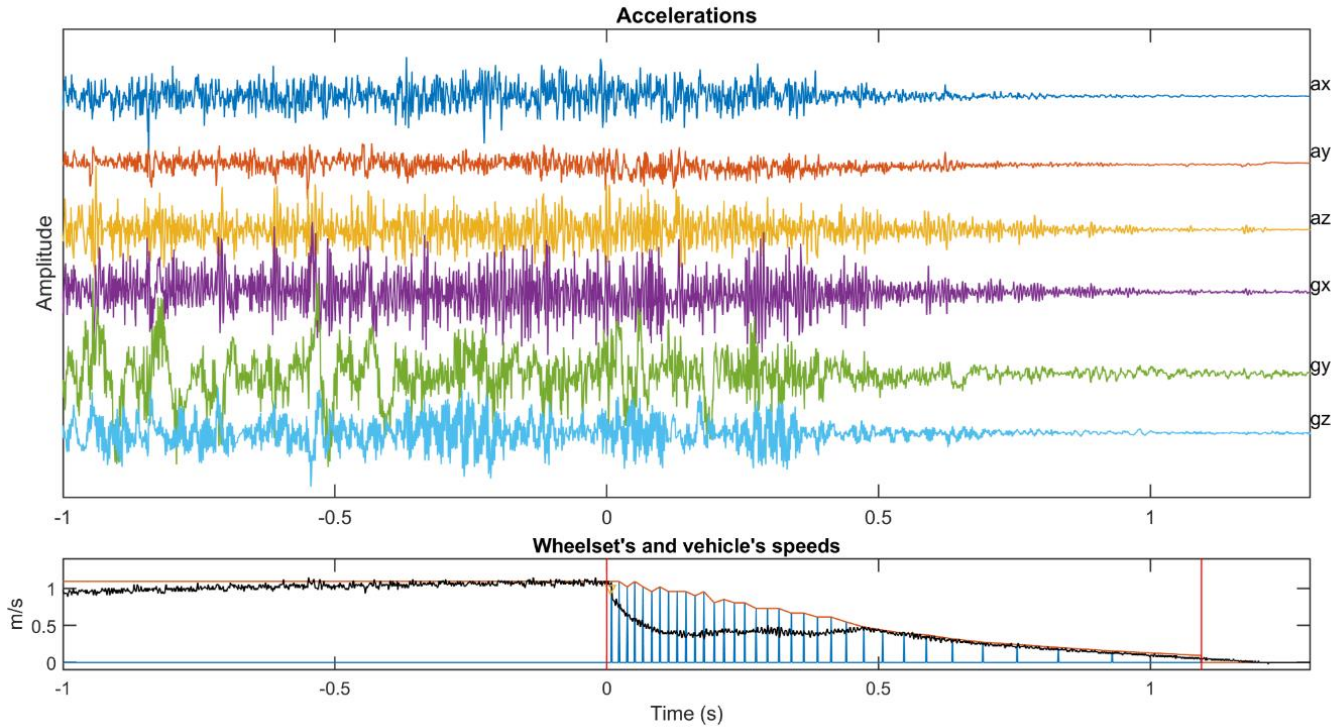


Figure 5.4 Time response of the vehicle vibrations in all three directions and rotations, before and during braking, on sand-scattered rails. Wheel and vehicle speeds are also displayed.

5.1.2 Descriptive statistics of the vibration's time series

In this section, the vibration signals of the vehicle are analyzed using the descriptive statistics techniques presented in section 3.1. The signals are analyzed before and during braking to determine whether or not the indices are proportional to the variations in friction.

5.1.2.1 Analysis before braking

Using equations 3.1 to 3.4, the statistical indices of the vibration measurements of the vehicle body before braking were calculated. Since it would be difficult to display the results of each test in this brief section, it was decided to show graphs with the average values from each test. However, the reader is encouraged to review Annex A, which contains all graphs with the statistical indices of each test. Figure 5.5 displays the kurtosis and crest factor results. Each colored line represents a different test type (the different contaminants), with each point representing the mean value for the longitudinal (a_x), lateral (a_y), vertical (a_z), roll (g_x), pitch (g_y), and yaw (g_z)

directions. In other words, each point on this graph represents the mean of 7 tests conducted on clean rails (red line), greased rails (blue line), soapy rails (green line), and sand-scattered (purple line).

In kurtosis chart, it is evident that the index is greater for low coefficients of friction, such as grease and clean rails. This is due to the fact that kurtosis is high when the data distribution is very far from or very close to the mean, as is the case for clean rails, where large amplitudes at the time of direct rail impacts but a rapid decline thereafter. A small kurtosis is the result of a more uniform distribution of vibration data due to the high coefficient of friction. This is most evident in the longitudinal (vehicle's movement direction) and lateral directions, whereas it is less pronounced in all other directions and rotations.

The crest factor also proved to be very useful in locating coefficients of friction with high or low values in the longitudinal and lateral directions, but it is slightly more confusing than kurtosis, especially in the vertical direction.

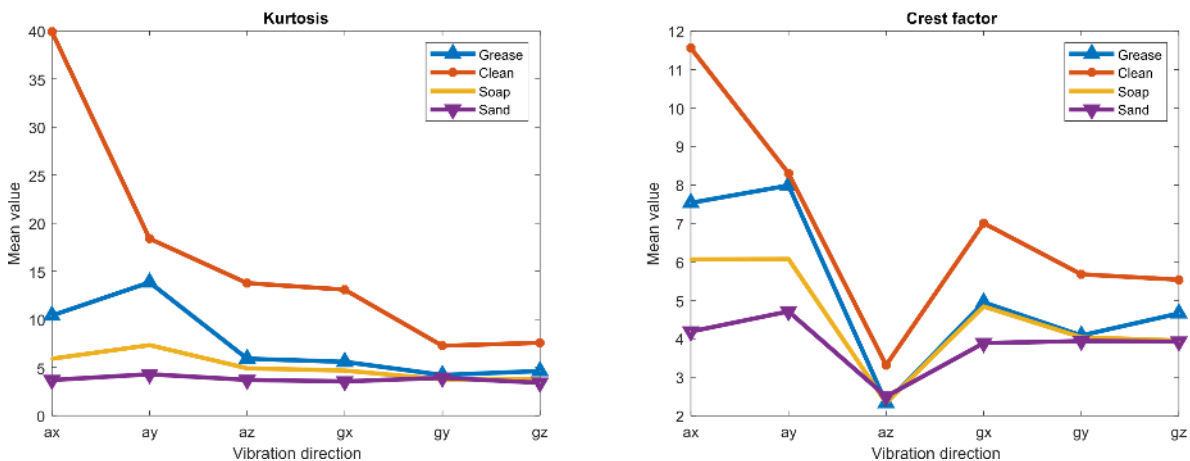


Figure 5.5 Kurtosis and crest factor indices of the vehicle's vibration data before braking. Every point of these charts are the mean values of every test type. The most evident differences in friction coefficient are in ax and ay directions, for the kurtosis, and in ax direction for the crest factor.

Differences between high and low friction coefficients are less pronounced in the variance and RMS values. Although there is a significant difference between the vibration levels of a clean and sand-scattered rail, as seen in Figures 5.1 and 5.4, both indices are identical in these charts. The amplitude of the vibrations is

comparable between the two coefficients of friction, but the duration is longer for sand, which is not easily distinguished by these indices.

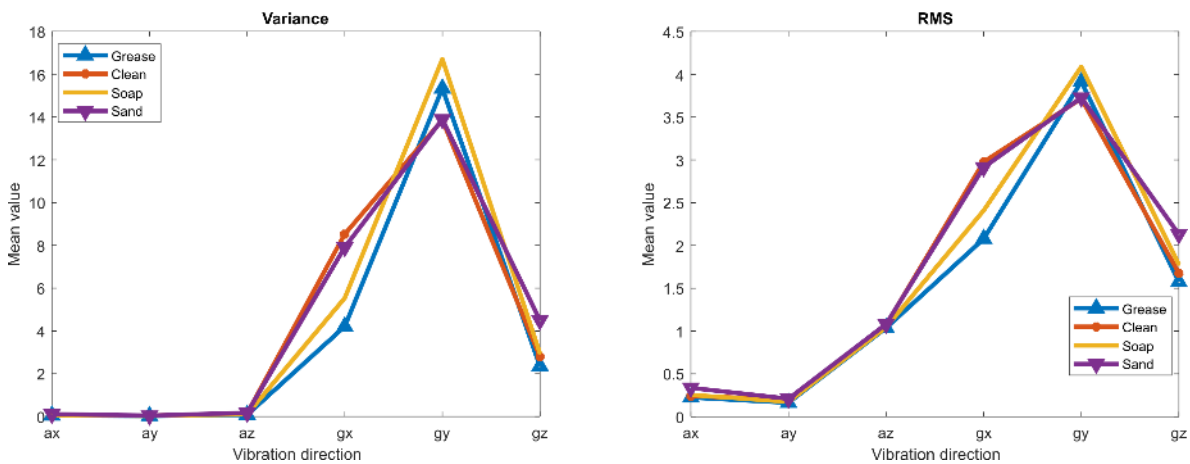


Figure 5.6 Variance and RMS indices of the vehicle's vibration data before braking. Every point of these charts are the mean values of every test type. Using these indices, there is no clear distinction between high and low friction coefficients; only in the gx direction a slight distinction is revealed.

As a final observation, based on the kurtosis and crest factor results, it appears that the coefficient of friction is lowest when the rails are clean. This could be due to the fact that the pulses caused by rail impacts are so large that they confuse these statistical indices. The good news is that very clean rails do not exist in reality, and there should be no such confusion in field applications. Nevertheless, there is a clear distinction between coefficients of friction with high and low values.

5.1.2.2 Analysis during braking

When applying a sudden brake, slippage and tangential forces increase significantly. During the first third of the braking phase, however, the vehicle still vibrates quite a bit. Figure 5.7 depicts the mean values of kurtosis and variance results for each direction. As in the analysis prior to braking, the kurtosis can easily differentiate between high and low coefficient of friction. The crest factor is also very effective at differentiating this distinction, but in the longitudinal and vertical directions, it becomes somewhat confused.

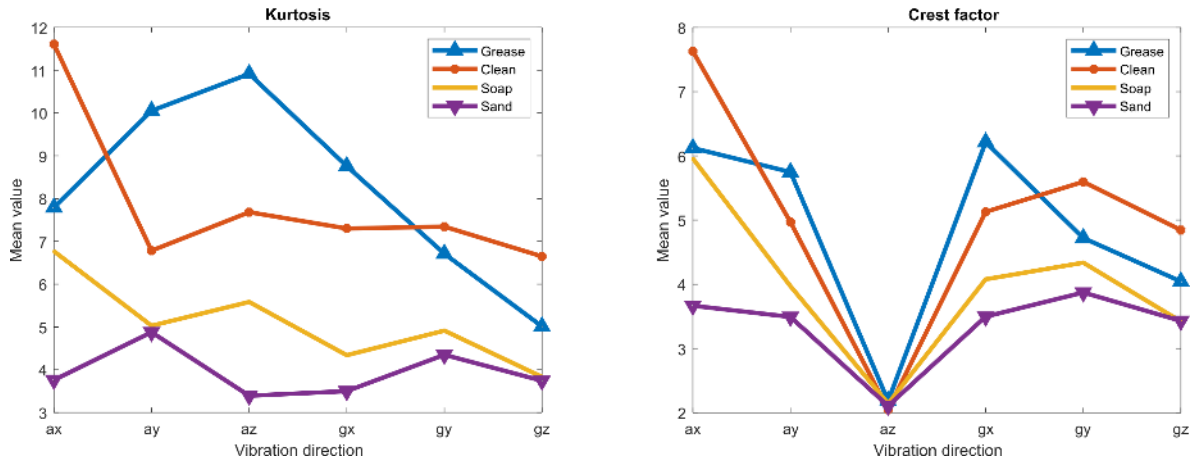


Figure 5.7 Kurtosis and crest factor indices of the vehicle’s vibration data during braking. Every point of these charts are the mean values of every test type. The most evident differences in friction coefficient are in ay , az and gx directions, for the kurtosis, and in ax , ay , gx , and gy direction for the crest factor.

Variance and RMS are somewhat more effective during braking, particularly in gx , gy , and gz rotations; see Fig. 5.8. During braking, it is easier to distinguish the coefficient of friction using these two methods, a result that differs from Figure 5.6. As will be demonstrated in the following section, this may be because braking vibrations are less chaotic.

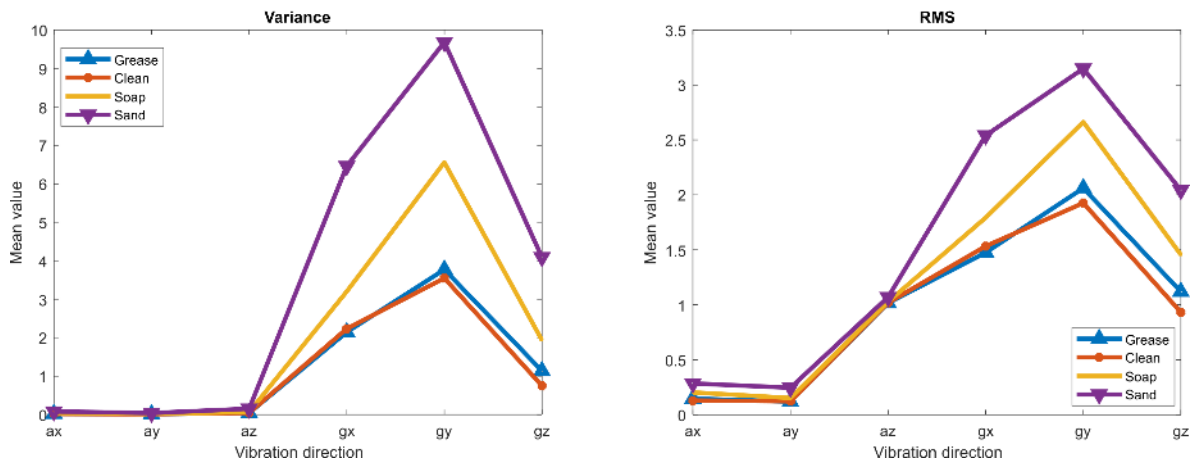


Figure 5.8 Variance and RMS indices of the vehicle’s vibration data during braking. Every point of these charts are the mean values of every test type. The most evident differences in friction coefficient are in gx , gy and gz directions, for both variance and RMS. It should be noted that, unlike kurtosis and crest factor, high coefficients of friction have greater RMS and variance indices than low coefficients of friction.

5.2 Frequency domain analysis.

In this section, it will be demonstrated that the change in vehicle dynamics is the result of changing the friction coefficient between wheels and rails. For this demonstration, the proposed correlation method is applied using frequency domain analysis. The methodology consists of comparing the wheel's dynamics to the vehicle's dynamics and seeking any similarities. If there is a clear similarity between the two dynamics when increasing the coefficient of friction in the wheels, then it is certain that the change in the vehicle's dynamics is a result of increasing the coefficient of friction.

In each experiment, seven signals are analyzed: the longitudinal, lateral, and vertical accelerations of the vehicle and its rotations, as well as the speed of the drive wheel. The signals ax , ay , az , gx , gy and gz describe the vehicle's dynamics, while the signal ws describes the dynamics of the wheel. Only the most extreme conditions are compared: when the rails are lubricated and when there is sand on them. The presented charts correspond to the outcomes of the CWT and FFT analyses. The proposed correlation method's comparison of the wheel and vehicle dynamics is also given.

5.2.1 Vibration analysis before braking

Initially, the wheel dynamics are examined for 0.5 seconds while running on the lubricated rails prior to braking. Figure 5.9 depicts the frequencies obtained from the FFT analysis, where the frequencies of 78, 158, and 177 Hz are special because they are also present in the vehicle's dynamics. It must take in mind that it is important to look for frequency similarities in order to verify if the wheel forces are transmitted to the vehicle.

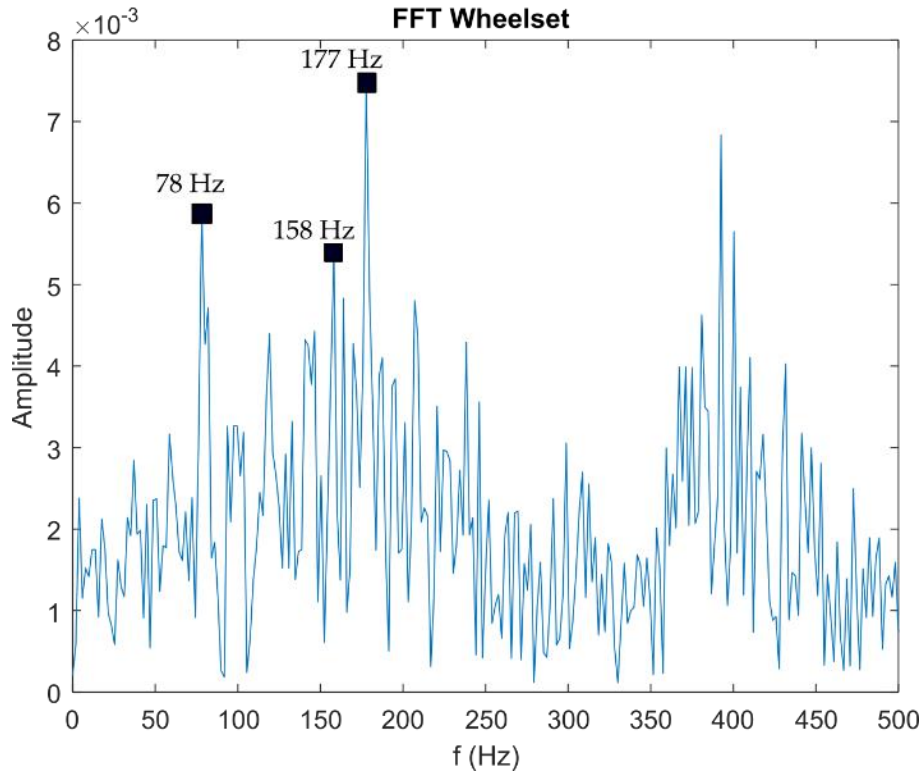


Figure 5.9 Frequencies obtained from the FFT analysis of the wheelset while running on greased rails.

Figure 5.10 demonstrates that the CWT analysis contains more information than the FFT because it locates the frequencies over time. This analysis is performed on the same previous data within the same time window. In the spectrogram, $t = 0$ represents the time at which the vehicle begins to brake. In the analysis, frequencies of 140, 180, and 200 Hz, as well as others with less amplitude, can be found. Important here are the amplitude and duration of the frequencies, as described in section 3.2.4; thus, it can be seen that when the rails are lubricated, both the amplitude and duration of the vibrations are small in comparison to a high-friction test results, as will be seen later. It is important to clarify at this point that the frequency range between 60 and 260 Hz was chosen because, according to an FFT analysis, the wheel vibrates in this range during all tests.

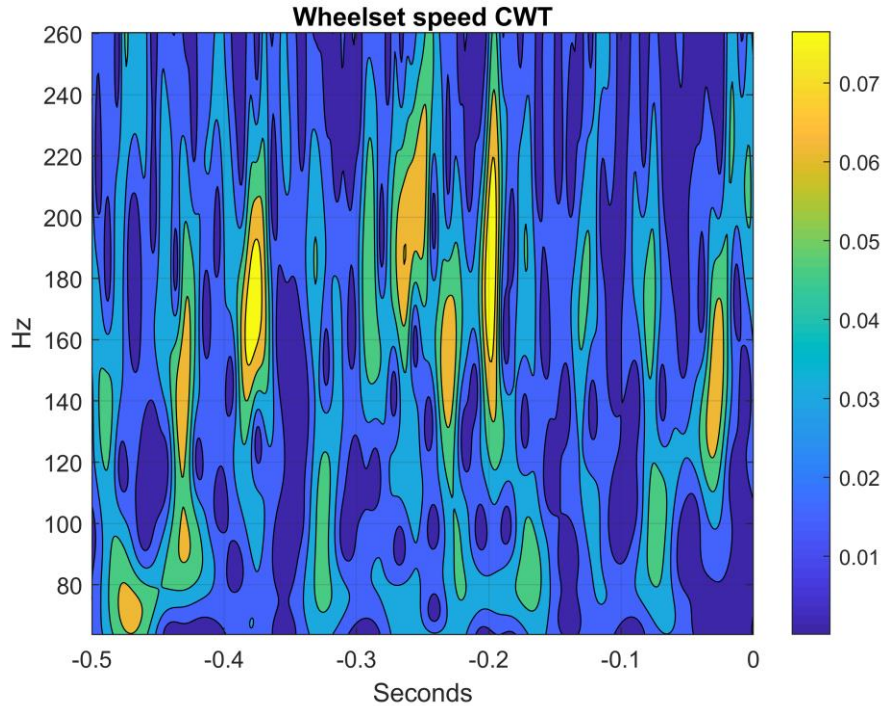


Figure 5.10 Results of the wheelset's CWT while running on greased rails. The yellow areas represent frequencies with the greatest amplitude. Multiple short-duration frequencies stand out.

Figure 5.11 depicts the spectrums used to analyze the vehicle's dynamics in all directions and rotations using the FFT. Very few of the vehicle's frequencies, such as 80, 158, and 180 Hz, are also found in the FFT spectrum of the wheel; see Figures 5.9 and 5.11. The spectrum of the vertical direction and of the rotations g_x and g_z are the most significant because they are the easiest to figure out and contain frequencies within the established range. As previously stated, frequencies greater than 260 are of no interest because they are unrelated to the dynamics of the wheel. Also, frequencies below 50 Hz, which are associated with wheel rotation, the passage of sleepers, and other phenomena, are of little interest because they are not part of the friction phenomenon.

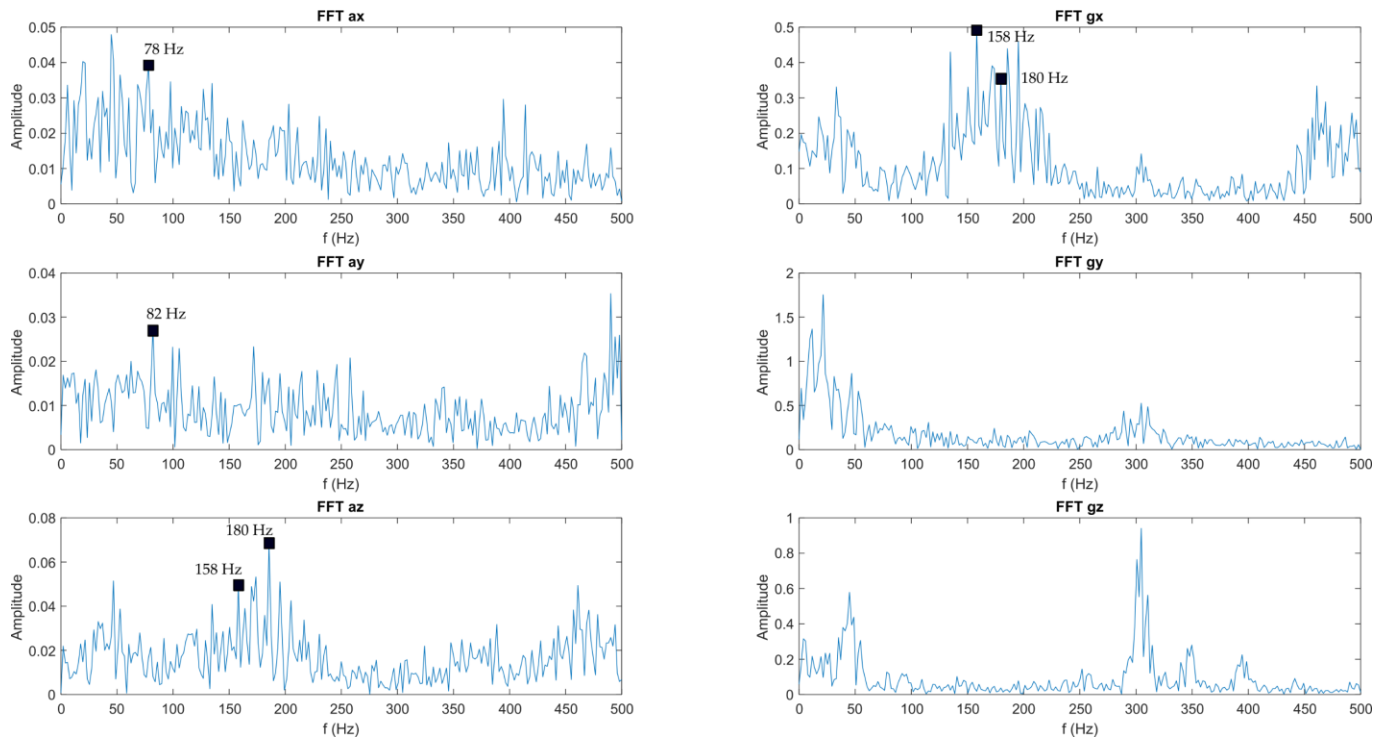


Figure 5.11 FFT spectrums of the vehicle's vibrations while running on greased rails. In these results, the most significant charts are the vertical direction and the rotation gx .

Figure 5.12 depicts the CWT spectrogram, which reveals how the vehicle dynamics behave in all directions over time. As can be seen, only the vertical direction and the gx rotation are noteworthy because they follow an easily discernible pattern. In contrast, the frequencies of the other directions and turns are highly dispersed or fall outside the frequency range.

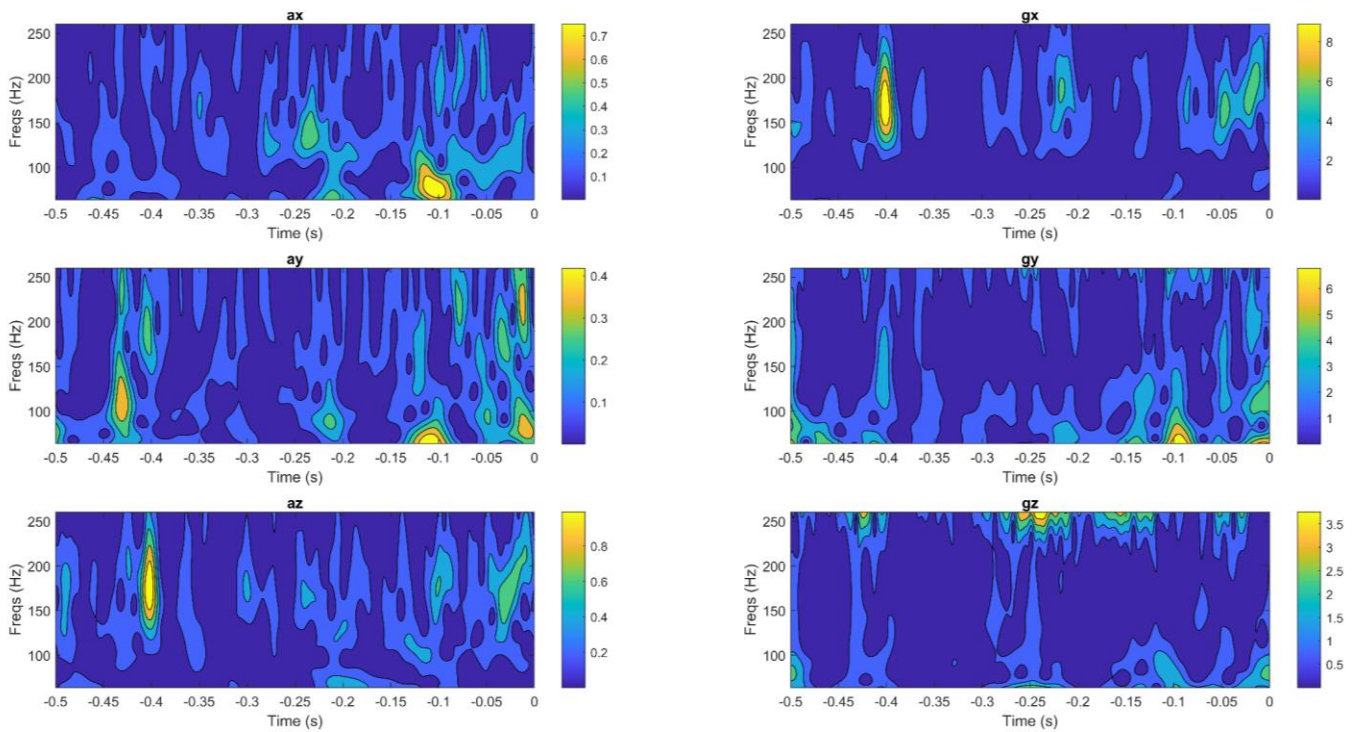


Figure 5.12 CWT spectrograms of the vehicle's vibrations while running on greased rails. In the vertical direction and the rotation gx , a pattern is obvious around 180 Hz, whereas in the other spectrograms, nothing of interest is visible.

The proposed correlation method is used to easily and quickly compare both the wheel and vehicle dynamics. The method outlined in section 3.24 identifies similarities in time and frequency between both dynamics in order to visualize how the friction forces on the wheels affect the vehicle. In addition to locating similarities in time and frequency, it is also important to consider the amplitude and duration of the matches. It can be seen that the gx rotation has the greatest amplitude and multiple matches around few frequencies. This fact indicates that the forces acting on the wheels can also be observed in the vehicle's roll. Additionally, the longitudinal and vertical directions have excellent matches, but they are very brief. In the lateral direction a significant disturbance appears at $t = -0.42$, however, this is a collision caused by the rails, as can be seen in Figure 5.1. Due to the brief duration and low magnitude of the tangential forces in this scenario, it is difficult to detect them on the vehicle's body during this analysis. Unlike the FFT, the correlation method makes comparing both dynamics less complicated.

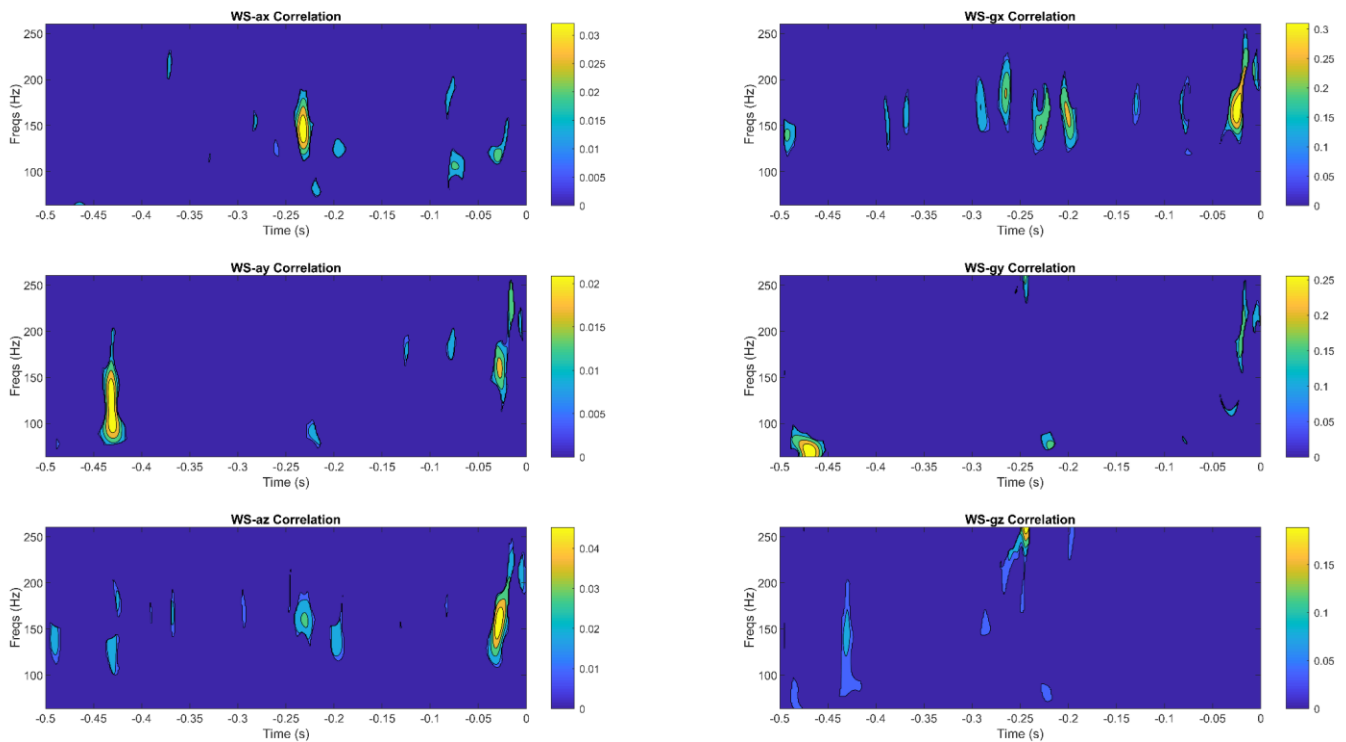


Figure 5.13 The results of the wheel and vehicle correlation using the proposed correlation method while running on greased rails. The regions with the greatest amplitude share the most similarities. In this instance, the roll motion (gx) correlates most closely with the wheel's dynamics.

According to the results of the frequency analysis, the dynamics of a wheel moving on sand-scattered rails are similar to those on greased rails. Figure 5.14 depicts the spectrogram of the wheel moving on sanded rails prior to braking, which is very similar to Figure 5.9.

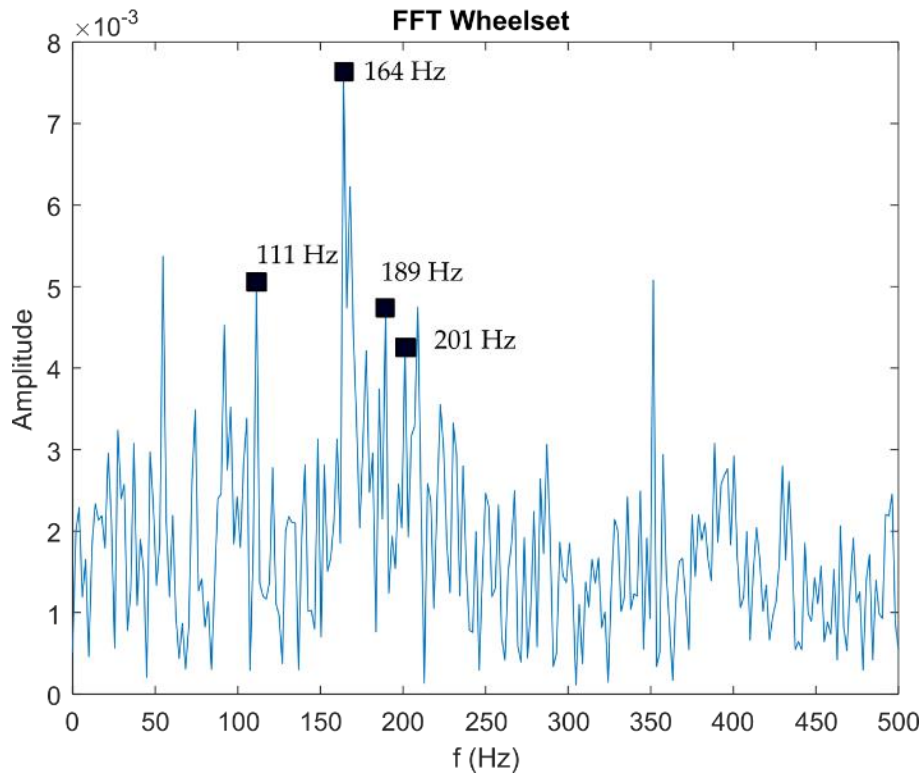


Figure 5.14 Frequencies obtained from the FFT analysis of the wheelset while running on sand-scattered rails. It is important to note that this spectrum closely resembles the spectrum in Figure 5.9.

Figure 5.15 depicts a CWT spectrogram of the wheel dynamics in which there is no discernible pattern, making it extremely difficult to determine what is going on. As shown by the FFT in Figure 5.14, the majority of frequencies appear to be around 165 Hz, but they are quite brief. This is because the sand particles are scattered evenly along the rails, making the wheels to vibrate randomly.

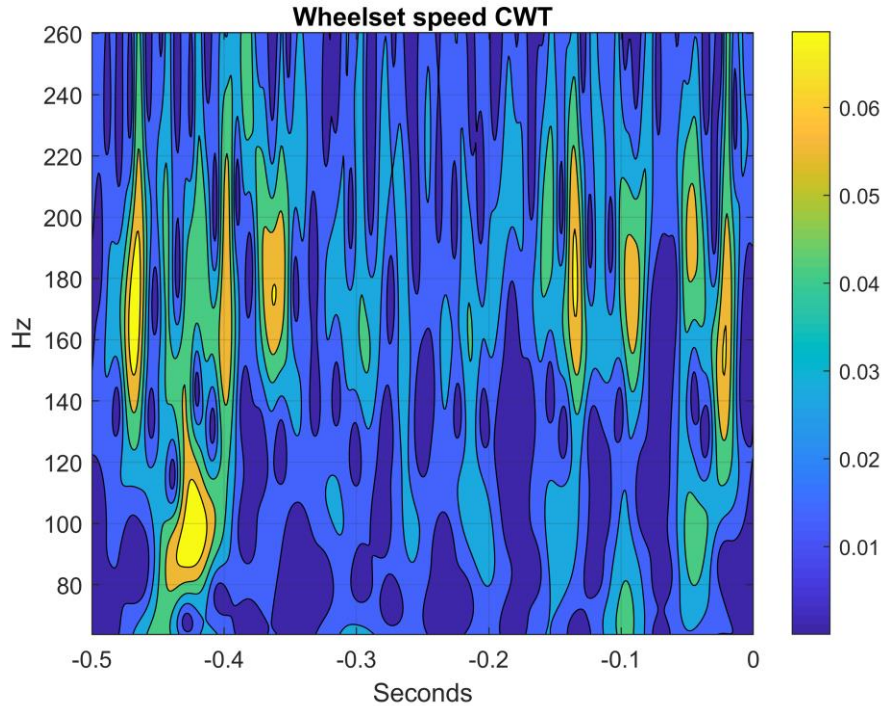


Figure 5.15 Results of the wheelset's CWT while running on sand-scattered rails. The yellow areas represent frequencies with the greatest amplitude. Multiple short-duration frequencies stand out, just like the spectrogram in Figure 5.10

The vehicle dynamics on sand-scattered rails exhibit notable dissimilarities when compared with those on oiled rails. Figure 5.16 displays the spectrograms of the vehicle vibrations, indicating that the frequencies are comparable to those of the greased rails. However, the amplitudes in the ax and az directions, as well as in the gx rotation, are significantly higher, nearly twice as much. The frequencies associated with wheel vibrations that are observed in the vehicle vibrations are 111, 168, 189, and 200 Hz.

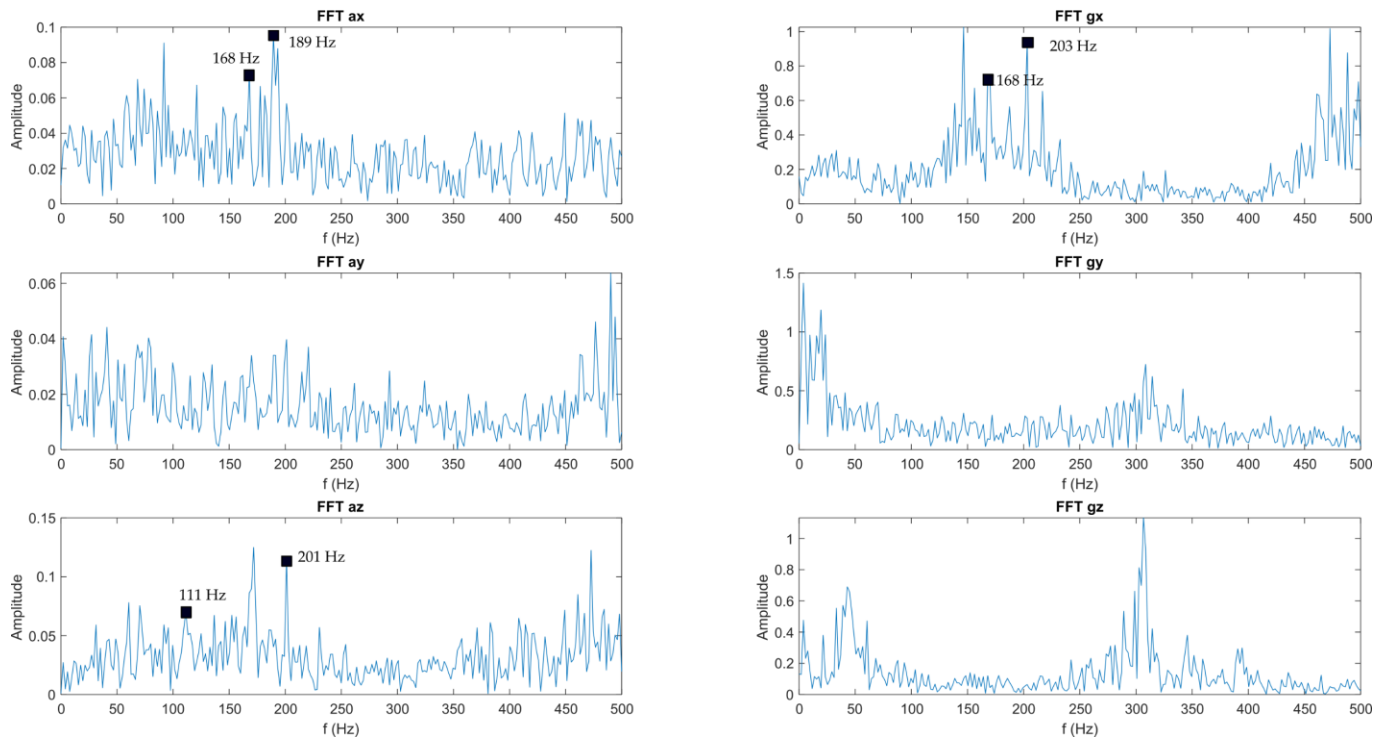


Figure 5.16 FFT spectrums of the vehicle's vibrations while running on sand-scattered rails. In these results, the most significant charts are also the vertical direction and the rotation gx .

The CWT results of the same data sample reveal a distinct pattern in the gx rotation during this test, see Figure 5.17. On the greased rails, something similar occurred, though at a lower intensity. In all other directions and rotations, there is little of interest, except for the gz turn, revealing that is unaffected by the wheel's dynamics.

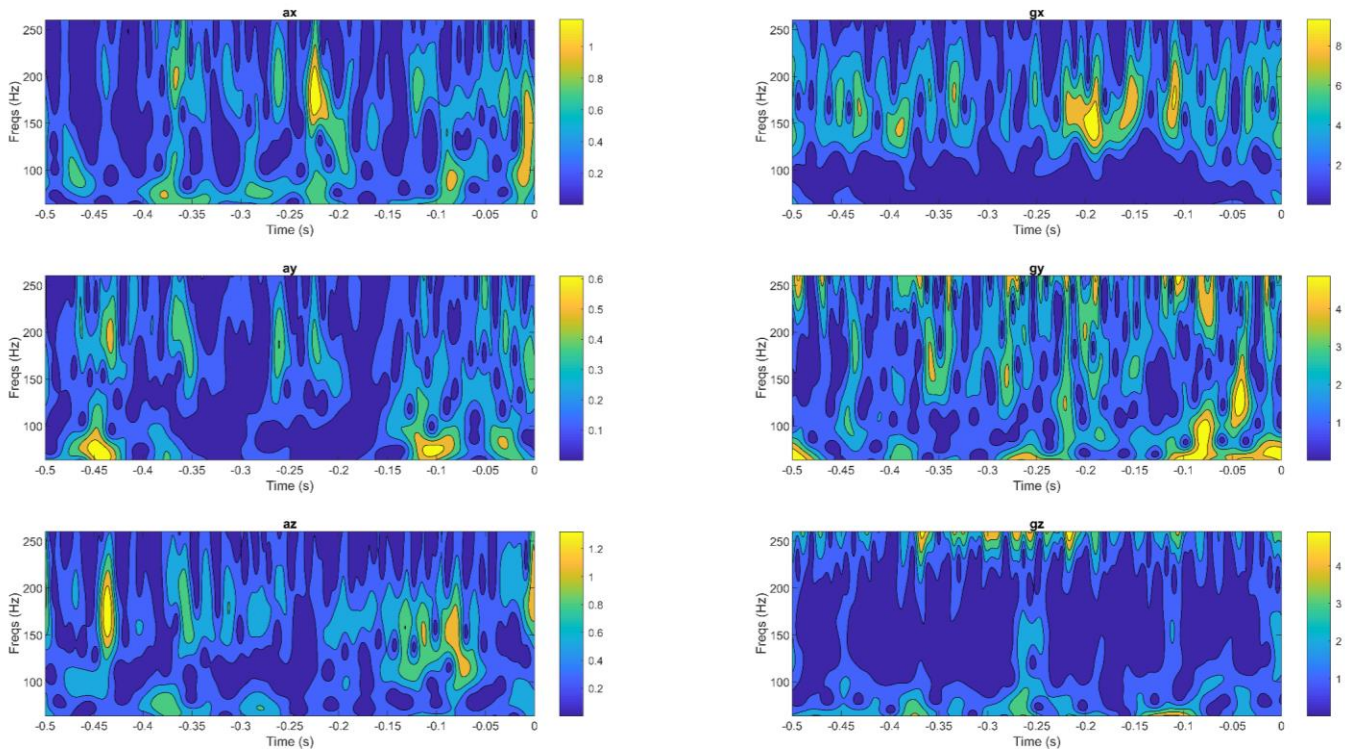


Figure 5.17 CWT spectrograms of the vehicle's vibrations while running on sand-scattered rails. In the vertical direction and the rotation gx , a pattern is obvious around 170 Hz, whereas in the other spectrograms, nothing of interest is visible.

Numerous coincidences are evident in the wheelset-vehicle correlation, particularly in the vertical direction and rotation gx , Figure 5.18. This indicates that the transmission of frictional forces is more efficient with a higher wheel-rail friction coefficient and can be detected in the vertical vibrations of the vehicle (roll can also be seen as a vertical vibration).

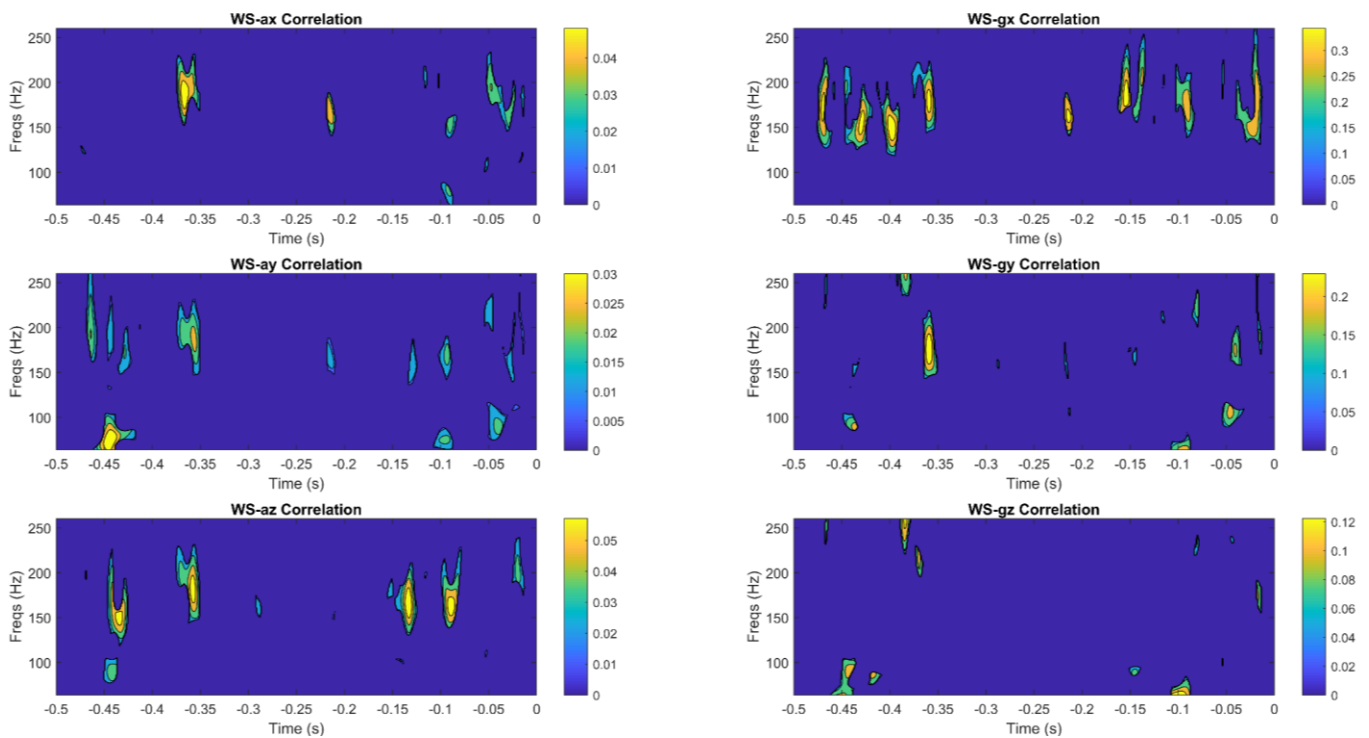


Figure 5.18 The results of the wheel and vehicle correlation using the proposed correlation method while running on sand-scattered rails. The regions with the greatest amplitude share the most similarities. In this instance, the vertical and roll motions correlates most closely with the wheel's dynamics.

5.2.2 Creep during braking

Before beginning the frequency analysis of vibrations during braking, it is necessary to show how the creep phenomenon occurs in rails with different coefficients of friction (grease and sand). When a vehicle brakes, the tangential speed of the wheel and the longitudinal speed of the vehicle differ, and this difference is more pronounced during abrupt braking. If the two speeds are different, then slippage is occurring between wheel and rail. Creep refers to the relative slippage of the wheels on the rail in relation to the vehicle's speed. During the raking tests, longitudinal creep is measured using the vehicle and the traction-wheel speeds. Figure 5.19 depicts the vehicle and wheel speeds for both greased and sand-scattered rails tests during braking.

In Figure 5.19a, the slip is extremely large, as the vehicle's speed decreases at a nearly constant rate, whereas the wheel's speed decreases abruptly from the beginning. Apparently, the wheel reaches equilibrium and continues rolling with a tangential velocity of 0.2 m/s for 1.4 s until the vehicle reaches the same speed at approximately $t=1.5$ s, at which point both components begin to slow down at the same rate. Figure 5.19b depicts the same behavior, but the wheel attains equilibrium at a speed of 0.4 m/s. This indicates that the creep is less and the friction force is more effective at slowing down the vehicle. In addition, when the friction coefficient is high, the wheel vibrates with a greater amplitude, and the vehicle reaches the same speed of both the wheel in a shorter amount of time.

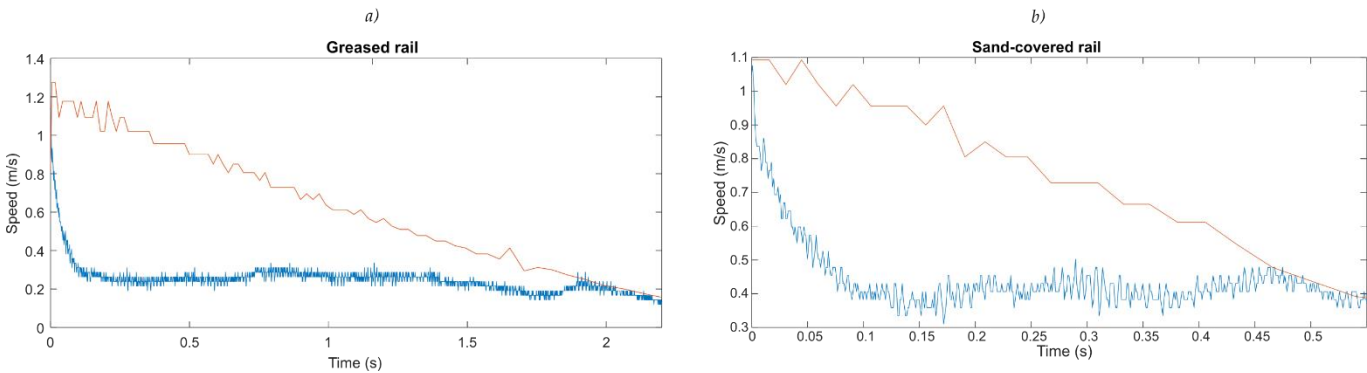


Figure 5.19 Behavior of vehicle and traction wheel speeds during a) greased rail test and b) sand-scattered rail test. The test vehicle can take up to 2 seconds to stop on clean rails, but only 0.75 seconds on sand-covered rails.

Figure 5.20 shows the creep curves of the greased rail and sand-scattered rail tests, computed using:

$$creep = \frac{V - ws}{V} \tag{5.1}$$

where V is the vehicle's speed and ws is the wheelset speed.

In these charts, it can be seen that the most significant creep occurs just after braking the vehicle and decreases gradually until it reaches a very low value (just when the wheel and vehicle speeds are equal). In the case of greased rails, the slip is very high (80 percent at its peak) and decreases slowly over 1.8 seconds. As expected, the sand's increased friction on the rail allows the wheel and vehicle to come to a faster stop. The span of the curve of the sand-scattered rail creep is 0.45 seconds,

and its peak value is 66%. Thus, demonstrating that the vehicle brakes faster as a result of greater frictional forces (lower tangential forces of sliding).

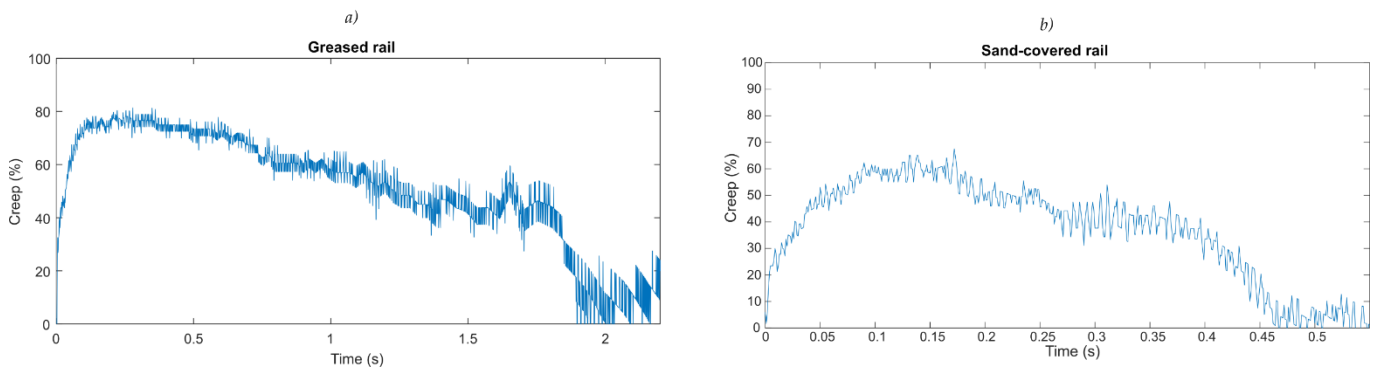


Figure 5.20 The creep produced by braking. a) Greased rails have a creep of up to 80%, while b) sand-scattered rails have a creep of up to 60%.

5.2.3 Frequency Analysis during braking.

Wheel vibrations and vehicle dynamics were analyzed at a time when the amount of creep was significant. In the case of oiled rails, this time is 1.5 s from the beginning of braking (as seen in Figure 5.1, the vehicle vibrates very little in the final 0.3 s of braking, so 1.5 s of analysis is sufficient). In the case of sand-covered rails, this time is 0.5 seconds. The analysis begins with the low-friction rails (greased rails).

The traction wheels vibrate minimally when braking on greased rails, even less than when the vehicle is not braking. The FFT revealed a small amplitude for a few principal frequencies shared by the vehicle dynamics. This is due to the fact that the wheel has a very large slip (80% creep), resulting in very low tangential forces; see also Figure 5.20a.

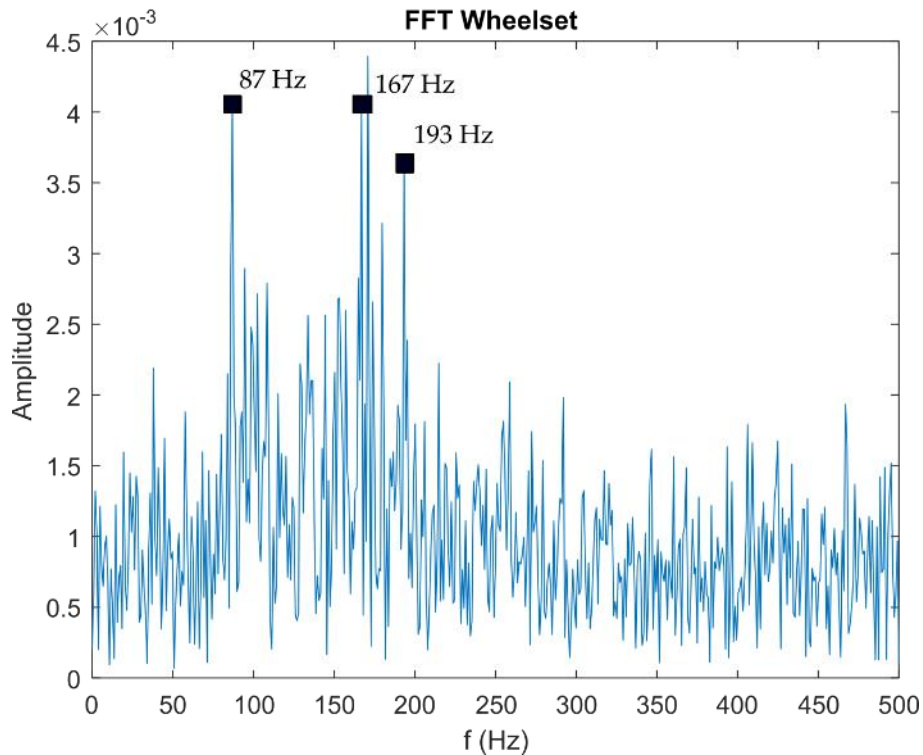


Figure 5.21 Frequencies obtained from the FFT analysis of the wheelset while braking on greased rails. This FFT spectrum is very different from the one shown in Figure 5.9, and the frequency components have a more moderate amplitude. Note that the 400 Hz frequencies, which are characteristic of the vehicle's dynamics, no longer appear.

The results obtained from the CWT reveal that the vibration frequencies of the wheel exhibit a certain level of dispersion when the vehicle applies the brakes on greased rails, as depicted in Figure 5.22. In addition to diminishing the coefficient of friction, the application of grease also serves to mitigate the impact between the wheel and the rail. Consequently, the magnitudes of wheel vibrations are significantly reduced during the braking process.



Figure 5.22 Results of the wheelset's CWT while braking on greased rails. The yellow areas represent frequencies with the greatest amplitude. Multiple short-duration frequencies stand out. In contrast to the no-brake scenario, a more regular pattern is observed here: one with low frequencies around 80 Hz and one with high frequencies around 180 Hz.

Because braking on lubricated rails results in minimal wheel movement, the vehicle's dynamics are also moderate. A small number of wheel frequencies, including 83, 156, 166, and 192 Hz, are detected with very low magnitude by the vehicle. Figure 5.23 demonstrates that, despite the low intensity of the vibrations under these low friction conditions, the FFT analysis of the vehicle vibration reveals that nearly the same frequencies result as in all previous cases. In all circumstances, only the intensity of the vibration varies.

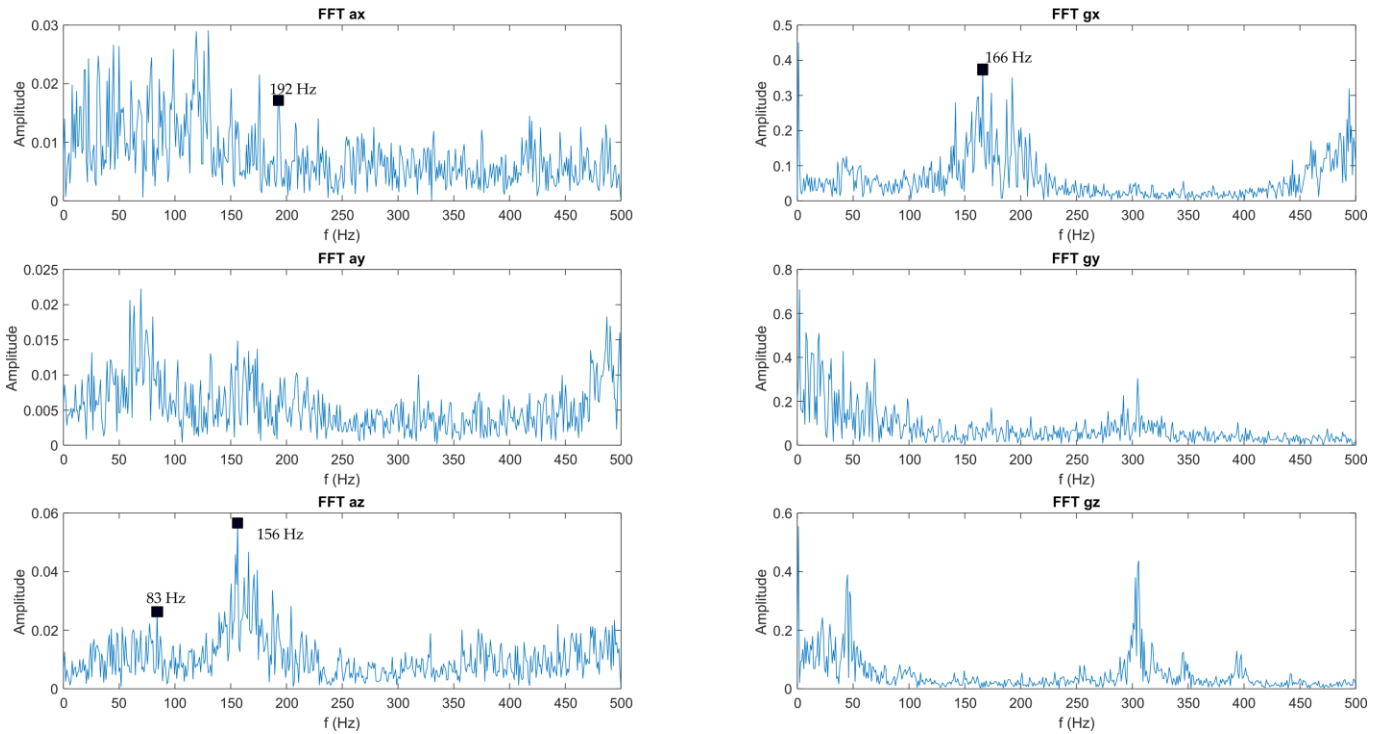


Figure 5.23 FFT spectrums of the vehicle's vibrations while braking on greased rails. In comparison to the no-brake scenario (see Figure 5.11), the resulting spectrums have smaller amplitudes and more distinct frequency components. The most significant charts in these results are the lateral and vertical directions as well as the rotation gx .

The CWT results, displayed in Figure 5.24, indicate that the highest vibration amplitudes occur at the beginning of braking, which makes sense given that the amplitudes are low at the end of braking because the vehicle is coming to a stop. Regardless, a pattern in the frequencies is only perceived in the vertical direction and in the gx rotation.

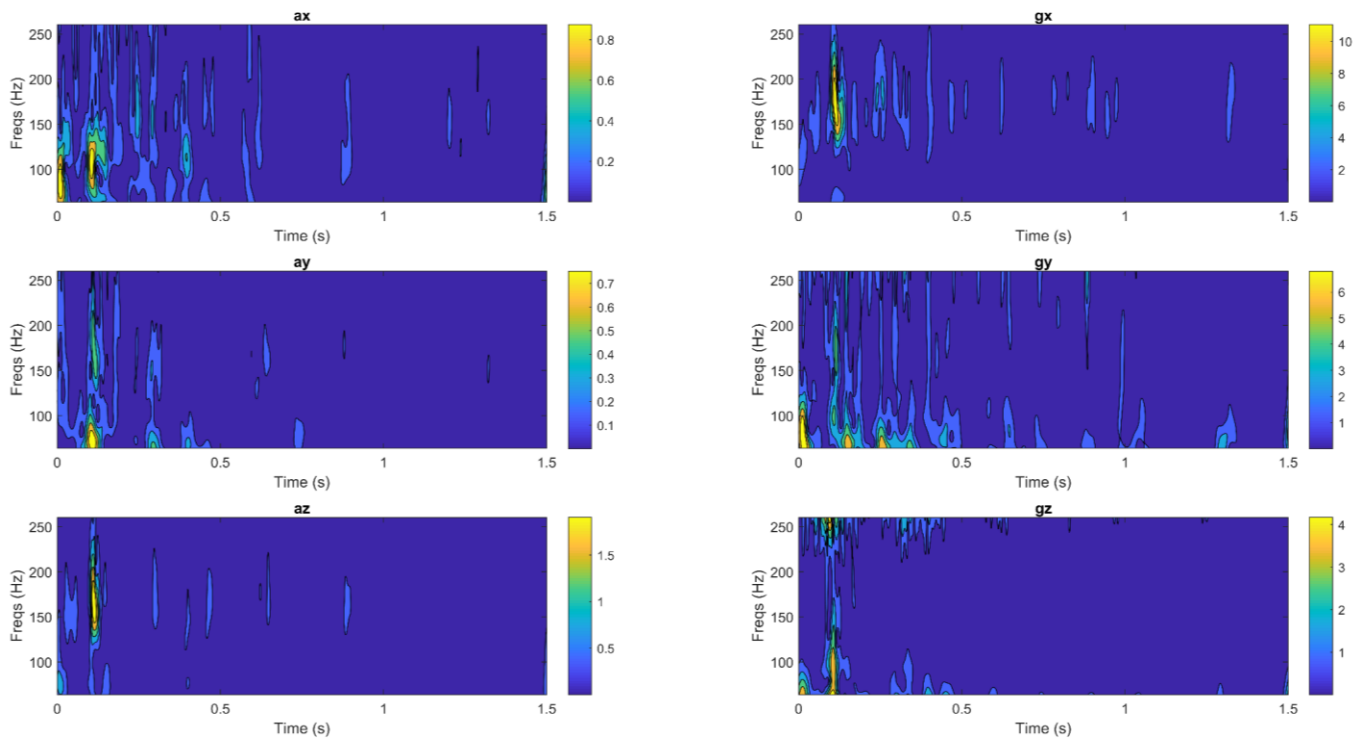


Figure 5.24 CWT spectrograms of the vehicle's vibrations while braking on greased rails. In these results, it can be seen that the highest vibration amplitude occurs around 150 Hz at the beginning of the braking action in the lateral and vertical directions, as well as the g_x rotation. This phenomenon is repeated, though at a lower intensity, in the vertical direction and g_x rotation for nearly the entirety of the braking slip.

Figure 5.25 displays the correlation results, which indicate that the vehicle and wheel dynamics share little similarity. This indicates that the tangential forces are insufficient to reach the vehicle's body.

So far, it is evident that the proposed correlation method is very useful, as it improves the search for similarities between the two dynamics, revealing that, under conditions of low friction, the vibrations of the vehicle have nothing to do with the tangential forces on the wheels.

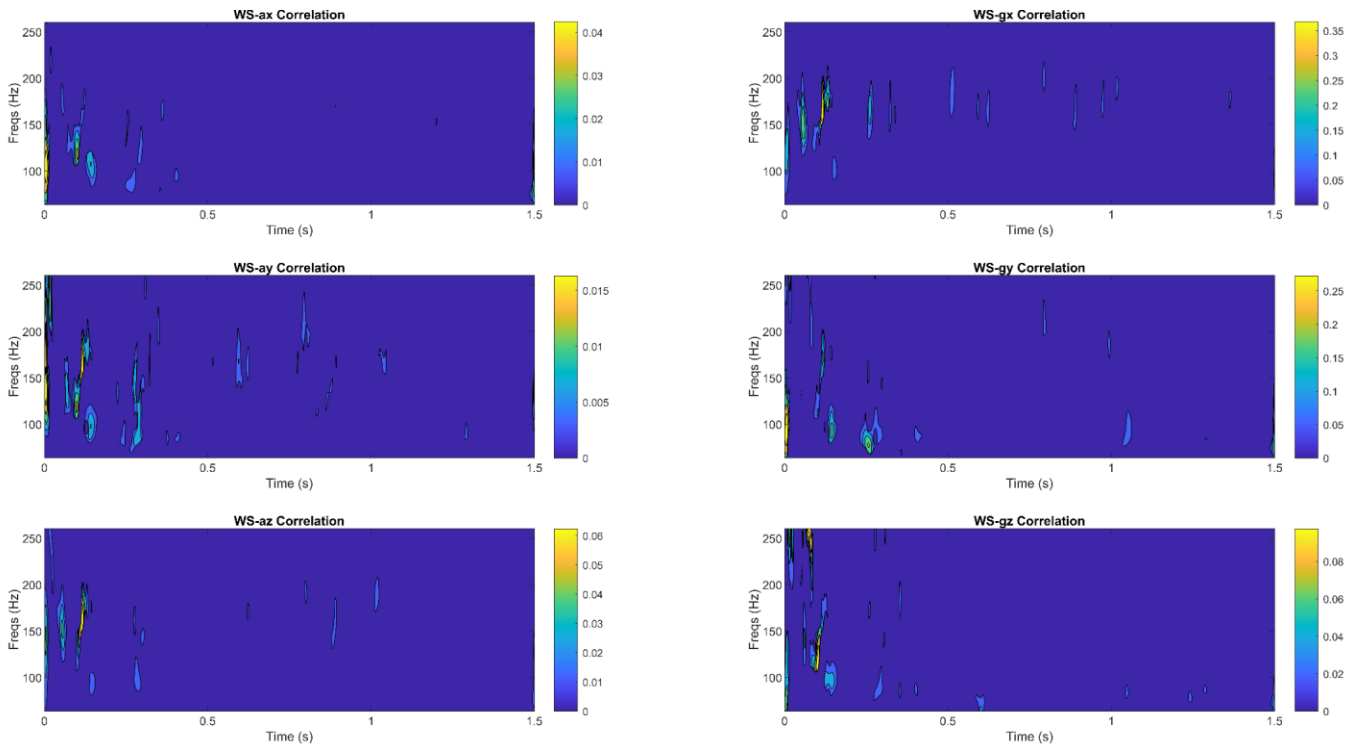


Figure 5.25 The results of the wheel and vehicle correlation using the proposed correlation method while braking on greased rails. The regions with the greatest amplitude share the most similarities. As expected, the highest correlation occurs at the start of braking, with frequencies around 150 Hz. This correlation can still be observed in the g_x rotation, though at a very low amplitude. This indicates that the friction forces and vibrations in the wheel are not effectively transmitted to the vehicle during this test.

Figure 5.26 shows that the amplitudes of wheel dynamics when braking on sand-scattered rails are significantly greater than when braking on greased rails. The most prominent peak corresponds to the natural frequency of the bogie suspension, which is around 144 Hz.

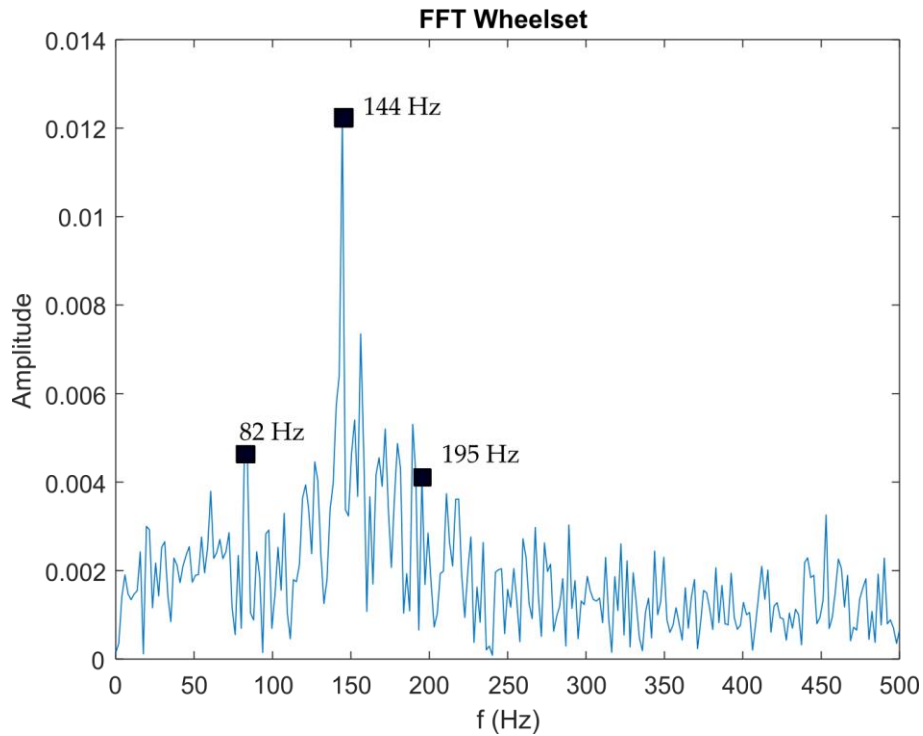


Figure 5.26 Frequencies obtained from the FFT analysis of the wheelset while braking on sand-scattered rails. This spectrum features a prominent 144 Hz peak, which distinguishes it from the spectrum in Figure 5.14. Similarly, the 350 Hz frequency, which is indicative of the vehicle's dynamics, is no longer discernible while braking.

According to the CWT results depicted in Figure 5.27, nothing interesting occurs at the beginning of braking, but at $t = 0.3$ s, there is an increase in friction with the rail, causing the wheel to vibrate at 144 Hz, as seen in the previous FFT. This vibration lasts approximately 0.2 seconds, which is significantly longer than any vibrations from the previous tests. The most interesting thing here is that the wheel vibrates at this frequency until it matches the vehicle's speed.

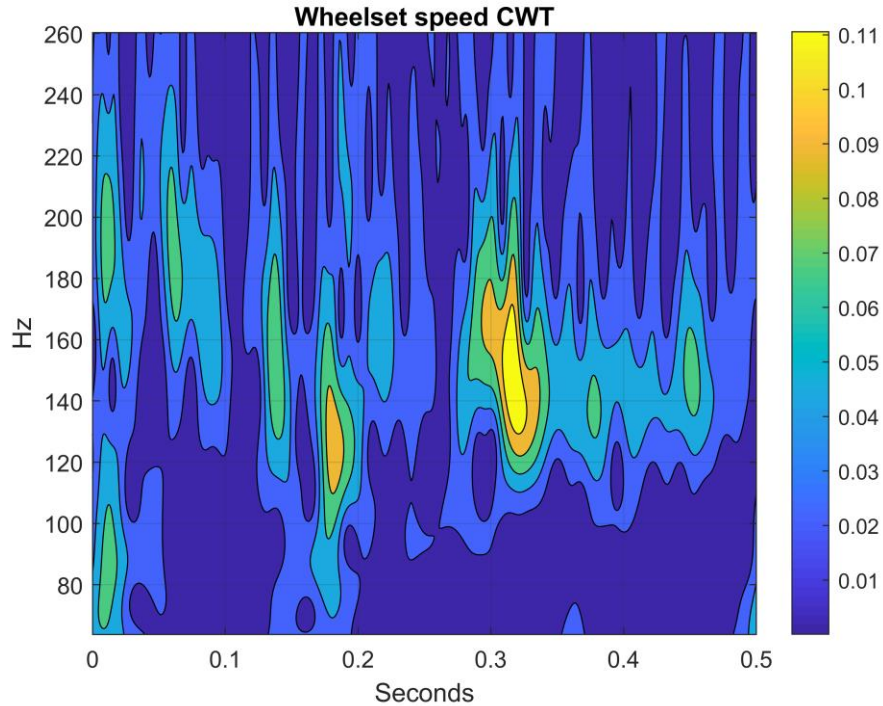


Figure 5.27 Results of the wheelset's CWT while braking on sand-scattered rails. The yellow areas represent frequencies with the greatest amplitude. At the initial stage of braking, there is no notable vibration behavior. At $t=0.3$, however, a 144 Hz component appears and persists until the conclusion of the slip.

The FFT spectrum exhibit minimal variation compared to the other tests, with the exception of significantly higher amplitudes, as depicted in Figure 5.28. During the conducted test, it was observed that the vehicle exhibited increased vibrations in the vertical direction and gx rotation, which can be attributed to the strong dynamics of the wheel.

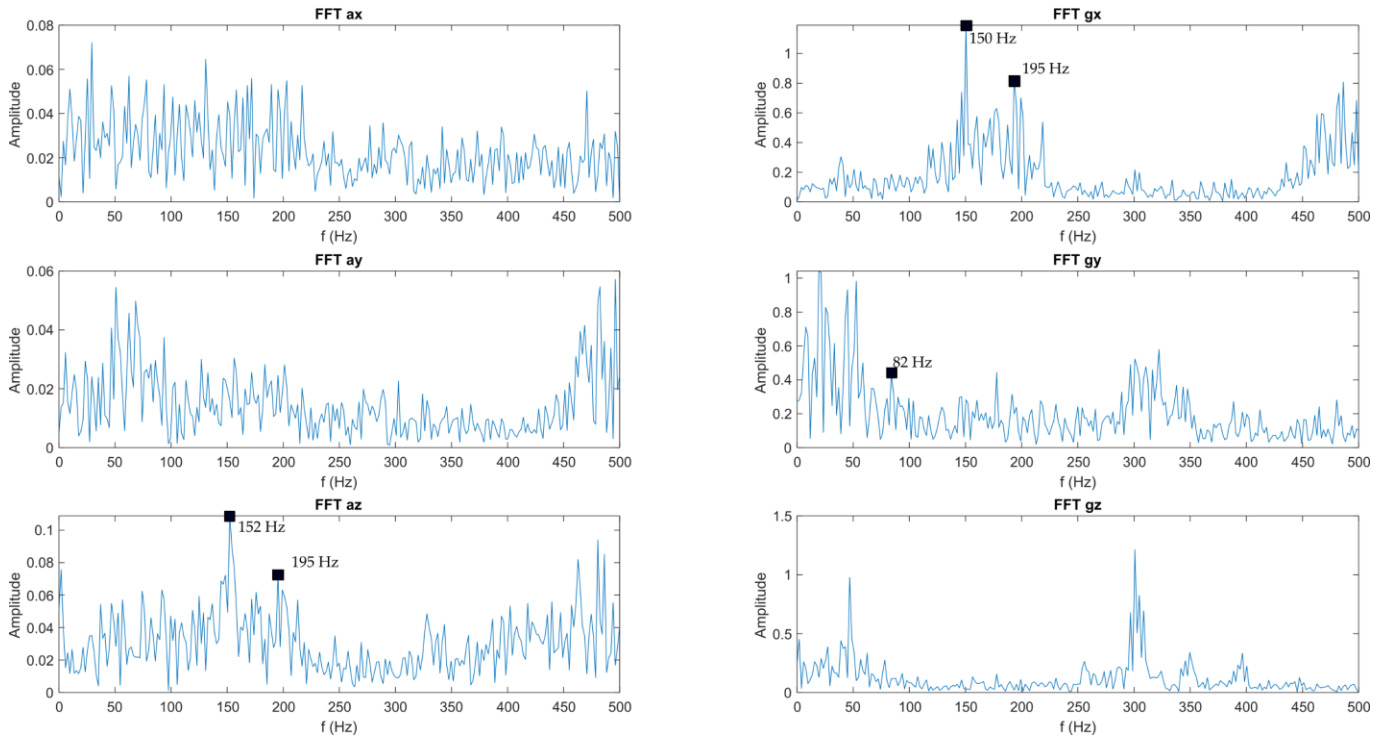


Figure 5.28 FFT spectrums of the vehicle's vibrations while braking on sand-scattered rails. In these results, the most significant charts are the vertical direction as well as the rotation g_x . The amplitudes in these results closely resemble those shown in Figure 5.16. In contrast, the 150 Hz peak is quite prominent in this case, indicating an absolute influence of wheel vibration on az and g_x .

When braking on sand-scattered rails, the vehicle's dynamics are entirely different from those of previous tests. The vehicle vibrates intensely in all directions in this particular case. In the vehicle dynamics spectrogram depicted in Figure 5.29, it can be observed that the vehicle is affected by the friction forces in the wheels in the lateral, vertical, and roll directions; even the yaw (g_z) turn is affected at $t = 0.3$.

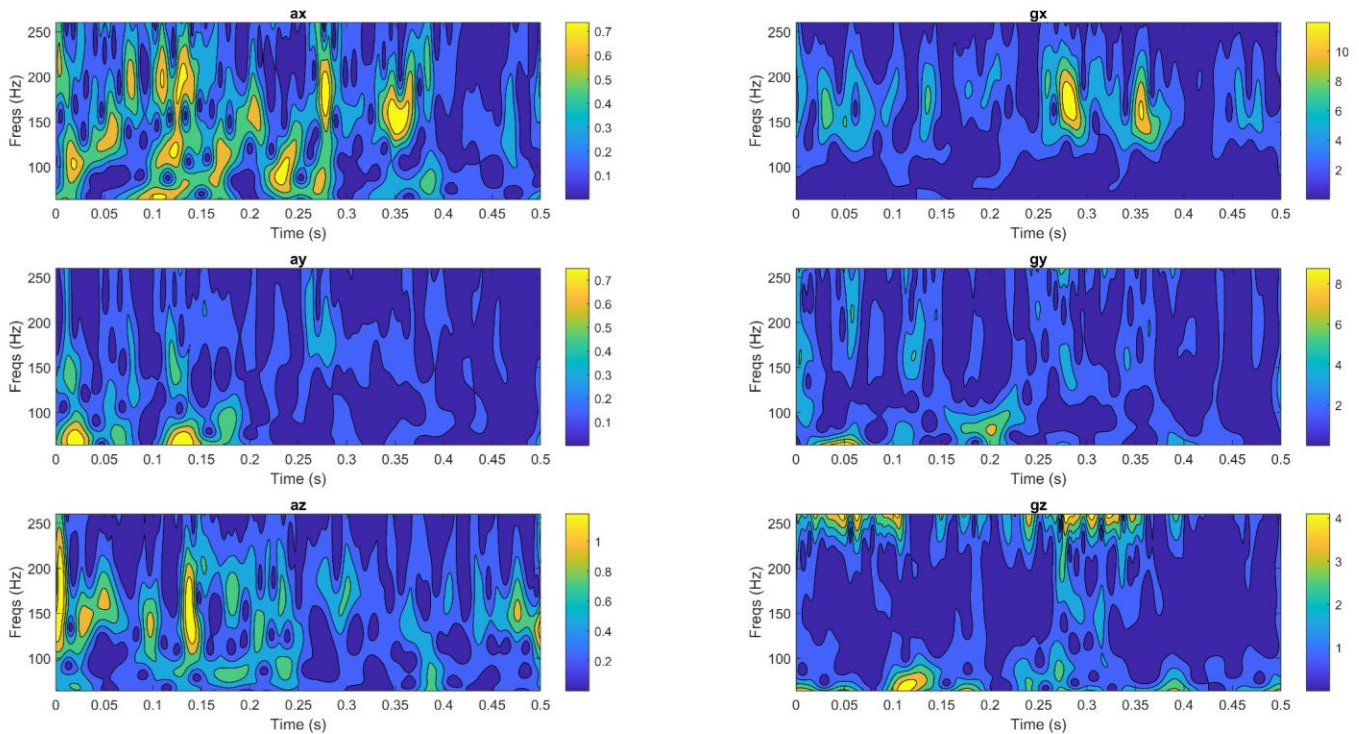


Figure 5.29 CWT spectrograms of the vehicle's vibrations while braking on sand-scattered rails. It is evident that the vehicle's lateral, vertical, and gx rotations are affected by the wheel's disturbance that occurs at $t=0.3$; even the vehicle's gz rotation is also affected.

The correlation between wheel and vehicle dynamics is illustrated in Figure 5.30. The chart clearly demonstrates that tangential forces play a significant role in influencing the dynamic response of the vehicle in all directions and rotations. Despite not having the highest vibration amplitudes among all tests, a significant proportion of traction wheel vibrations are transferred to the vehicle body in this case.

The vehicle roll is the most prominent motion in this analysis because it correlates with the dynamics of the wheel for a longer duration than any other motion. This becomes immediately apparent when the friction increases abruptly at $t = 0.3$ s. When braking on rails with a high coefficient of friction, the vehicle's dynamics fully respond to the friction forces on the wheels.

Surprisingly, there is a strong correlation between wheel and vehicle dynamics in the longitudinal direction. This is extremely difficult to figure out in the FFT spectrum, but with this tool, it is evident in which direction and at what time the vehicle is affected by the frictional forces on the wheels.

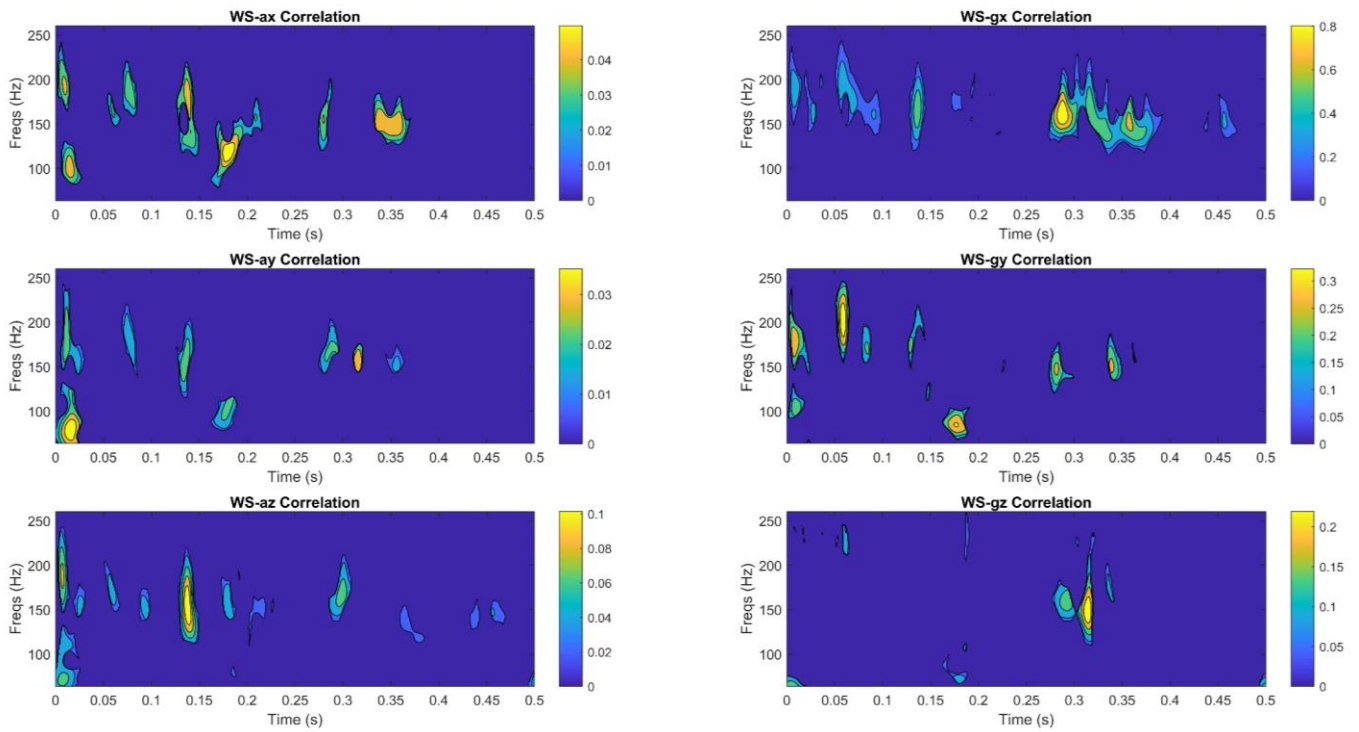


Figure 5.30 The results of the wheel and vehicle correlation using the proposed correlation method while braking on sand-scattered rails. These graphs illustrate how significantly wheel disturbances impact the vehicle. The vibrations of the wheel braking under high friction conditions on the rails completely affect the vehicle's body from beginning to end. The perturbation of the wheel at $t=0.3$ can be seen clearly in the longitudinal direction and in the rotation gx .

6 Conclusions and prospects

6.1 Conclusions

In this project, the effect of wheel friction on the dynamic response of a 1:20-scale railroad vehicle was investigated. The vehicle was subjected to a number of braking tests with varying wheel coefficients of friction. Accelerometers were used to measure vibrations within the vehicle's body.

It was discovered that low coefficients of friction result in low vibrations or in vibrations with high amplitude and short duration. High friction coefficients, on the other hand, result in longer-lasting vibrations with a more uniform distribution, but not necessarily the largest amplitude. Before and during braking, these vibrations were analyzed using statistical indices such as kurtosis, crest factor, RMS, and variance. Kurtosis and crest factor best distinguished between low friction and high friction vibrations on running, while RMS and variance are better during braking.

In addition, an analysis of the frequencies was conducted using the FFT, CWT, and a proposed correlation method to demonstrate that the frictional forces on the wheels influence the vehicle dynamics by increasing the coefficient of friction. However, FFT

does not reveal all of the characteristics of the phenomenon of braking. In contrast, the CWT spectrograms proved to be very useful for studying the vehicle's response, in addition to their results being incorporated into the proposed correlation method.

It was discovered that the forces of friction in the wheels have an effect on the vehicle's dynamics, as evidenced by the correlation charts. This is most noticeable when braking on rails with high friction. These results demonstrate implicitly that it is possible to study the forces of friction in the wheels using the vehicle's vibrations.

The correlation method proposed in this study proves to be a highly valuable tool for examining the source of oscillatory loads in a mechanical system. It was applied in this project to show how braking on rails with a high coefficient of friction significantly influence the dynamics of rail vehicles.

Researchers who design railway braking systems will find the results of this study useful. Before applying the brakes, the control system can take into account the vehicle's level of vibrations, which indicate the degree of wheel friction. On rails with low or high friction, inconveniences can be avoided by measuring with accelerometers from the locomotive's cabin.

6.2 Prospects

Using vibrations to better comprehend the phenomenon of wheel friction requires further investigation. For example, the origin of squeal, rail corrugation, and the formation of flat faces in wheels.

The results of the statistical indices can be used to measure the coefficient of friction (to determine whether it is high or low) and to implement more optimal braking control. Then, there is the possibility of designing the braking control based on the vibration indices for both the scale vehicle and full-scale trains.

It remains feasible to perform a comparable investigation on full-scale railway vehicles in order to illustrate the impact of variations in the coefficient of friction on the dynamic response of the vehicle, as previously demonstrated with the scale-down model.

7 References

1. Arias-Cuevas, O., Li, Z., Lewis, R., & Gallardo-Hernandez, E. A. (2010). Rolling–sliding laboratory tests of friction modifiers in dry and wet wheel–rail contacts. *Wear*, 268(3-4), 543-551.
2. Bosso, N., Gugliotta, A., Magelli, M., Oresta, I. F., & Zampieri, N. (2019). Study of wheel-rail adhesion during braking maneuvers. *Procedia Structural Integrity*, 24, 680-691
3. Bosso, N., Gugliotta, A., Magelli, M., Oresta, I. F., & Zampieri, N. (2019). Study of wheel-rail adhesion during braking maneuvers. *Procedia Structural Integrity*, 24, 680-691.
4. Carter, F.W. (1926). On the action of a locomotive driving wheel. Proc. Royal Society, London, vol. A112, pp. 151-157.
5. Clemente-Lopez, D., Rangel-Magdaleno, J. J., Munoz-Pacheco, J. M., & Morales-Velazquez, L. (2022). A comparison of embedded and non-embedded FPGA implementations for fractional chaos-based random

- number generators. *Journal of Ambient Intelligence and Humanized Computing*, 1-15.
6. Cureño-Osornio, J., Zamudio-Ramirez, I., Morales-Velazquez, L., Jaen-Cuellar, A. Y., Osornio-Rios, R. A., & Antonino-Daviu, J. A. (2023). FPGA-Flux Proprietary System for Online Detection of Outer Race Faults in Bearings. *Electronics*, 12(8), 1924.
 7. Eroğlu, M., Koç, MA, Esen, İ., & Kozan, R. (2022). Train-structure interaction for high-speed trains using a full 3D train model. *Journal of the Brazilian Society of Mechanical Sciences and Engineering*, 44 (1), 48.
 8. Garg, V. (2012). Dynamics of railway vehicle systems. Elsevier.
 9. H. Hertz, "Gesamelte Werke," Vol. 1, p. 155, Leipzig, 1895.
 10. Harmon, M., & Lewis, R. (2016). Review of top of rail friction modifier tribology. *Tribology-Materials, Surfaces & Interfaces*, 10(3), 150-162
 11. Hurtado-Hurtado, G., Morales-Velazquez, L., Valtierra-Rodríguez, M., Otremba, F., & Jáuregui-Correa, J. C. (2022). Frequency Analysis of the Railway Track under Loads Caused by the Hunting Phenomenon. *Mathematics*, 10(13), 2286.
 12. Iwnicki, S., & Iwnicki, S. (Eds.). (2006). Tribology of the Wheel-Rail Contact. Handbook of Railway Vehicle Dynamics (1st ed., pp. 282-291.). CRC Press.
 13. Jáuregui-Correa, JC, Morales-Velazquez, L., Otremba, F., & Hurtado-Hurtado, G. (2022). Method for predicting dynamic loads for a health monitoring system for subway tracks. *Frontiers in Mechanical Engineering*, 1-16.
 14. Johnson, K.L. (1985). *Contact Mechanics*. Cambridge University Press.
 15. Kalker J. J. and H. Goedings, A Program for Three-Dimensional Steady-State Rolling. Internal Report, Delft University of Technology, Delft, Netherlands (1972).
 16. Kalker, J. J. (1967). On the rolling contact of two elastic bodies in the presence of dry friction.
 17. Kalker, J. J. (1979). Survey of wheel-rail rolling contact theory. *Vehicle System Dynamics*, vol. 5, pp. 317-358.

18. Koç , MA (2022). A new expert system for active vibration control (AVC) for high-speed train moving on a flexible structure and PID optimization using MOGA and NSGA-II algorithms. *Journal of the Brazilian Society of Mechanical Sciences and Engineering*, 44 (4), 151.
19. Lee, JS, Choi, S., Kim, SS, Park, C., & Kim, YG (2011). A mixed filtering approach for track condition monitoring using accelerometers on the axle box and bogie. *IEEE Transactions on Instrumentation and Measurement*, 61 (3), 749-758.
20. Lixin , Q., & Haitao , C. (2001). Three dimension dynamics response of car in heavy haul train during braking mode. In *7th International Heavy Haul Conference* (pp. 231-238).
21. Lu, X., Cotter, J., & Eadie, D. T. (2005). Laboratory study of the tribological properties of friction modifier thin films for friction control at the wheel/rail interface. *Wear*, 259(7-12), 1262-1269.
22. Lundberg, J., Rantatalo, M., Wanhainen, C., & Casselgren, J. (2015). Measurements of friction coefficients between rails lubricated with a friction modifier and the wheels of an IORE locomotive during real working conditions. *Wear*, 324, 109-117.
23. Moore, D. F., (1975). Chapter 14 - Transportation and Locomotion, Principles and Applications of Tribology, 302-330.
24. Murat Yucel & N. Ferhat Ozturk (2017): Real-time monitoring of railroad track tension using a fiber Bragg grating-based strain sensor, *Instrumentation Science & Technology*
25. Nielsen, JC, & Johansson, A. (2000). Out-of-round railway wheels-a literature survey. *Proceedings of the Institution of Mechanical Engineers, Part F: Journal of Rail and Rapid Transit*, 214 (2), 79-91.
26. Olofsson, U. (2009). Adhesion and friction modification. In *Wheel-rail interface handbook* (pp. 510-527). Woodhead Publishing.
27. Polach, O. (1999). A fast wheel-rail forces calculation computer code. *Vehicle System Dynamics*, 33(sup1), 728-739.

28. Polach, O. (2005). Creep forces in simulations of traction vehicles running on adhesion limit. *Wear*, 258(7-8), 992-1000.
29. Randall, R. B. (2021). *Vibration-based condition monitoring: industrial, automotive and aerospace applications*. John Wiley & Sons.
30. Roberts, J. J., & Green, S. I. (2021). Experimental study of train sanding. *Proceedings of the Institution of Mechanical Engineers, Part F: Journal of Rail and Rapid Transit*, 235(3), 265-274.
31. Suh, N. P., & Sin, H. C. (1981). The genesis of friction. *Wear*, 69(1), 91-114.
32. Tanaka, H., Matsumoto, M., & Harada, Y. (2016). Application of axle-box acceleration to track condition monitoring for rail corrugation management.
33. Tao, G., Wen, Z., Liang, X., Ren, D., & Jin, X. (2019). An investigation into the mechanism of the out-of-round wheels of metro train and its mitigation measures. *Vehicle System Dynamics*, 57 (1), 1-16.
34. Tsunashima, H. (2019). Condition monitoring of railway tracks from car-body vibration using a machine learning technique. *Applied Sciences*, 9 (13), 2734
35. Vollebregt, E. A. H. (2014). Numerical modeling of measured railway creep versus creep-force curves with CONTACT. *Wear*, 314(1-2), 87-95.
36. Wei, X., Liu, F., & Jia, L. (2016). Urban rail track condition monitoring based on in-service vehicle acceleration measurements. *Measurement*, 80, 217-228.
37. Ye, Y., Zhu, B., Huang, P., & Peng, B. (2022). OORNet: A deep learning model for on-board condition monitoring and fault diagnosis of out-of-round wheels of high-speed trains. *Measurement*, 199, 111268.
38. Zhang, Z., & Dhanasekar, M. (2009). Dynamics of railway wagons subjected to braking/traction torque. *vehicle System Dynamics*, 47 (3), 285-307

Annex A. Result Figures.

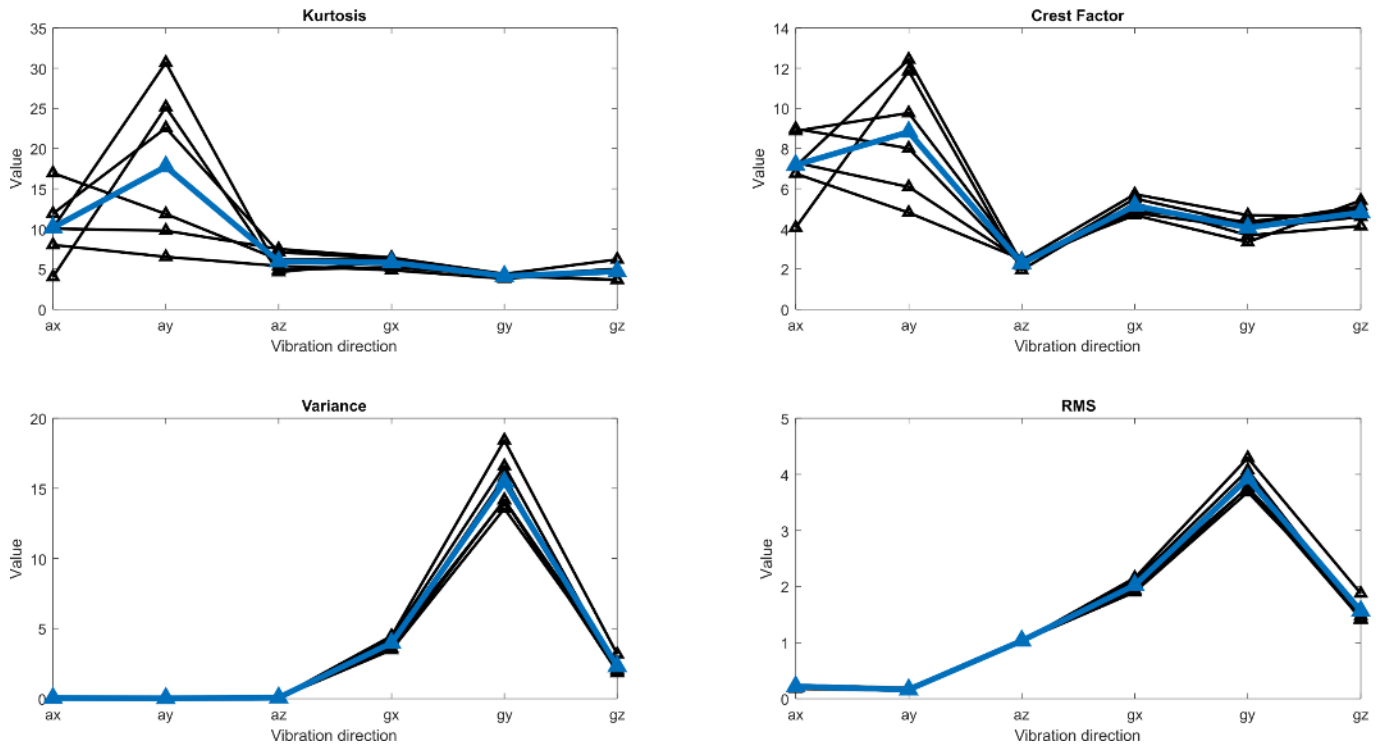


Figure A 1 Greased rails before braking. Black lines are all the 7 test, blue line is the average.

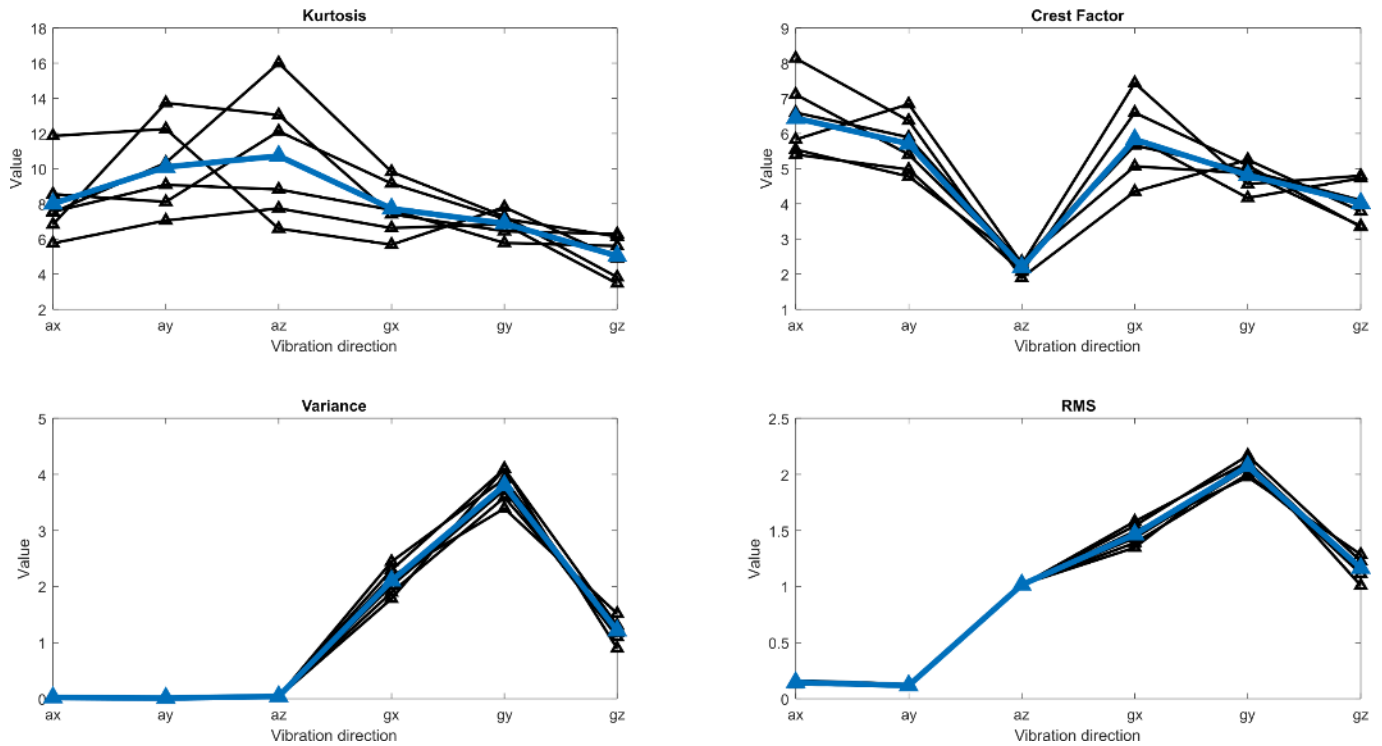


Figure A 2 Greased rails during braking. Black lines are all the 7 test, blue line is the average.

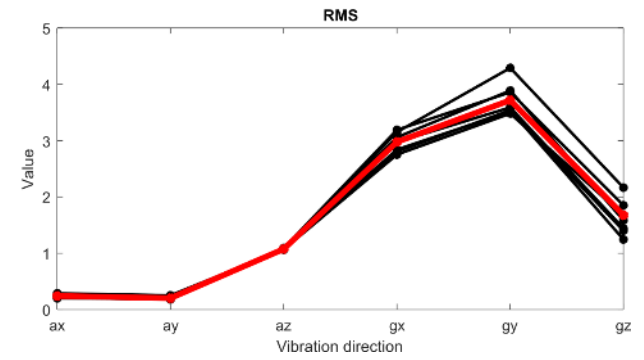
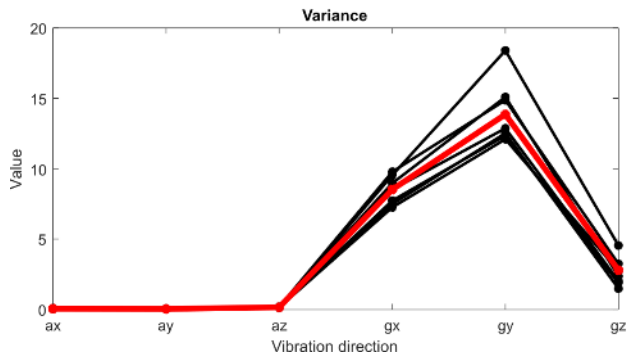
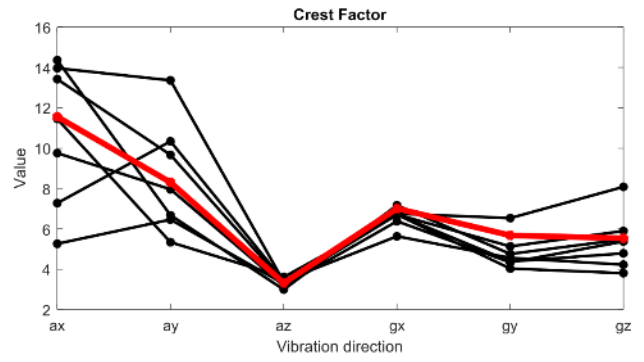
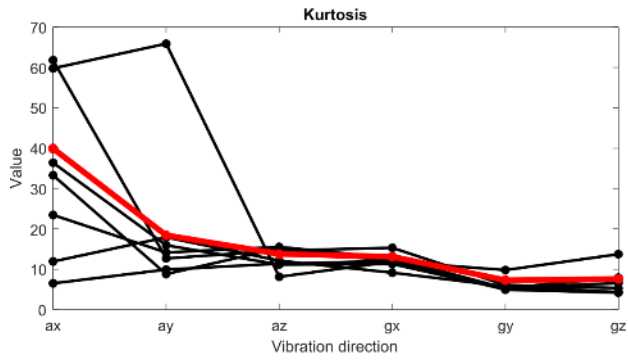


Figure A 3 Clean rails before braking. Black lines are all the 7 test, blue line is the average.

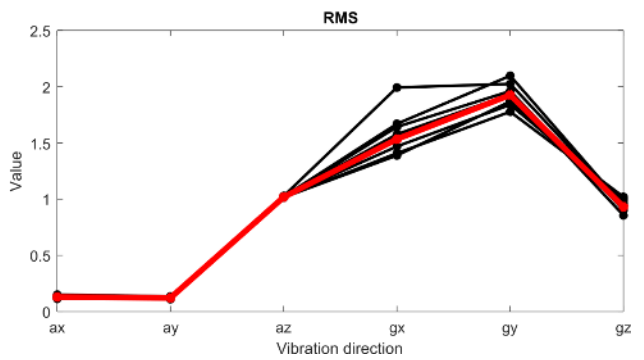
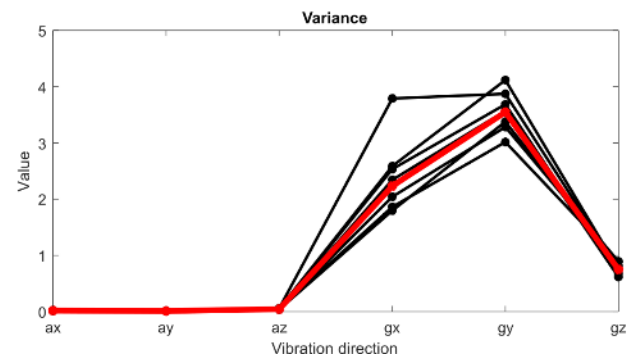
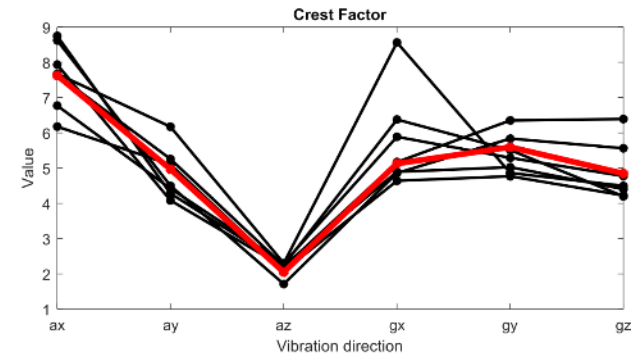
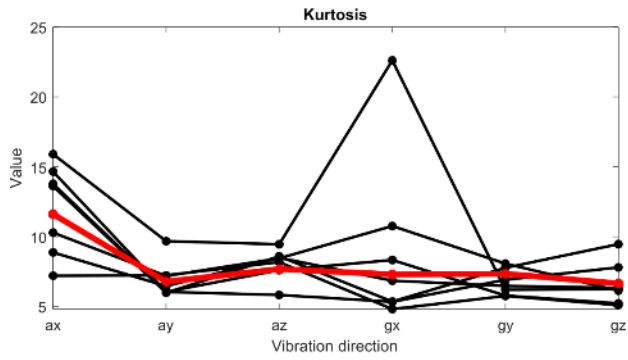


Figure A 4 Clean rails during braking. Black lines are all the 7 test, blue line is the average.

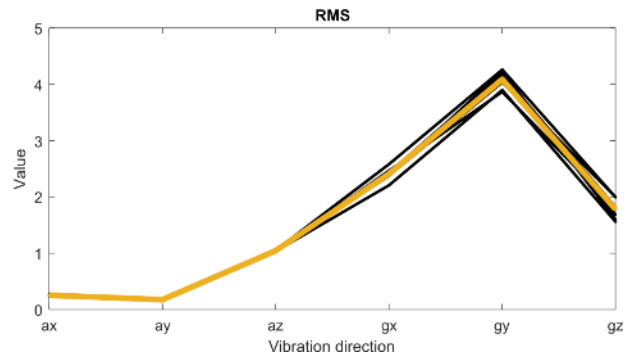
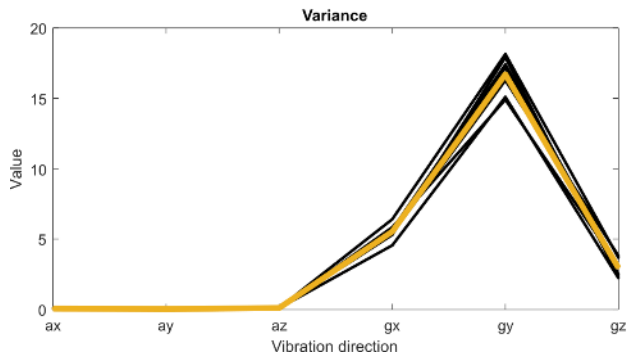
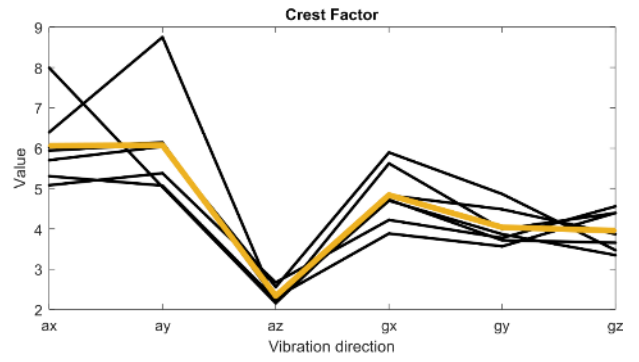
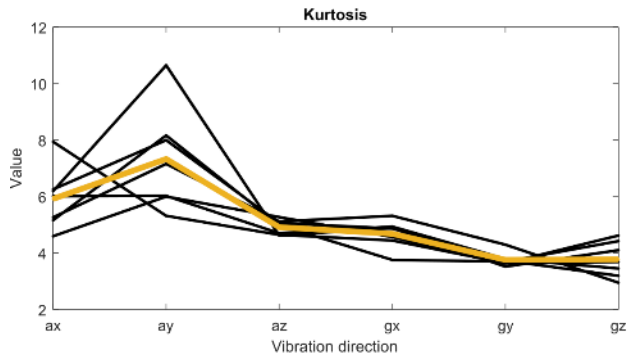


Figure A 5 Soap rails before braking. Black lines are all the 7 test, blue line is the average.

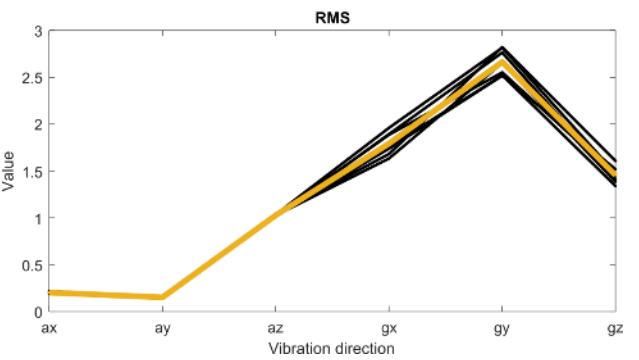
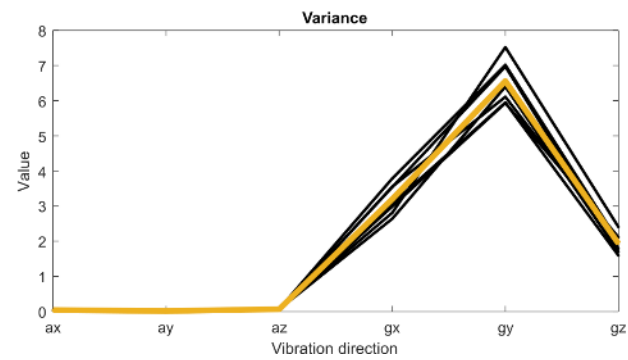
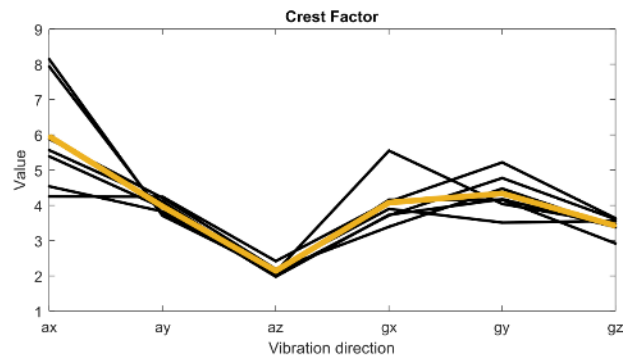
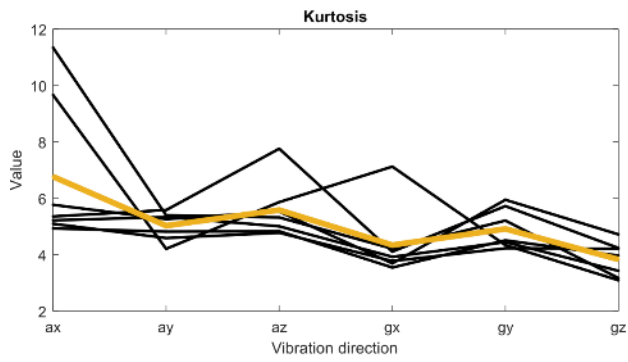


Figure A 6 Soap rails during braking. Black lines are all the 7 test, blue line is the average.

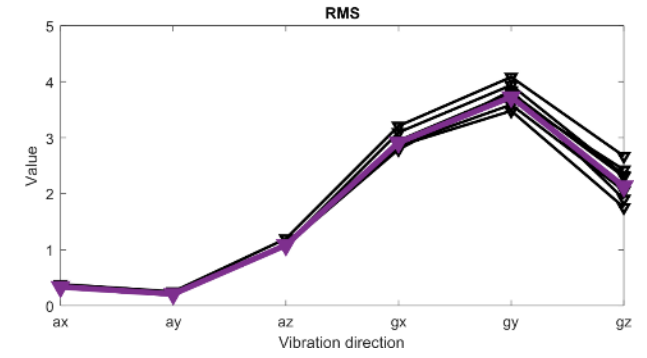
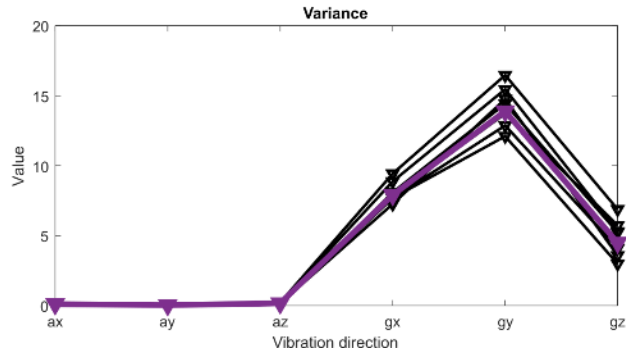
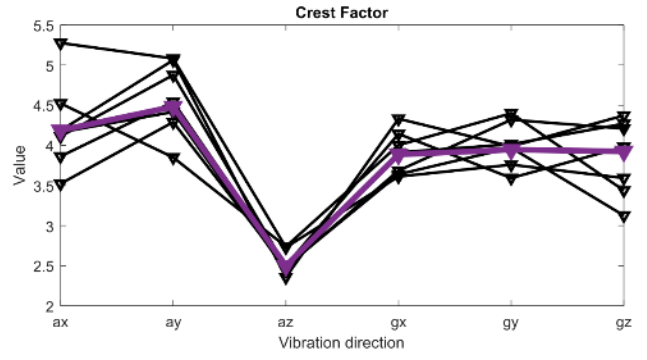
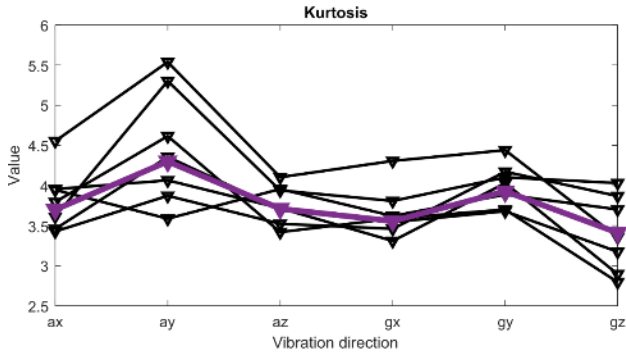


Figure A 7 Sand-scattered rails before braking. Black lines are all the 7 test, blue line is the average.

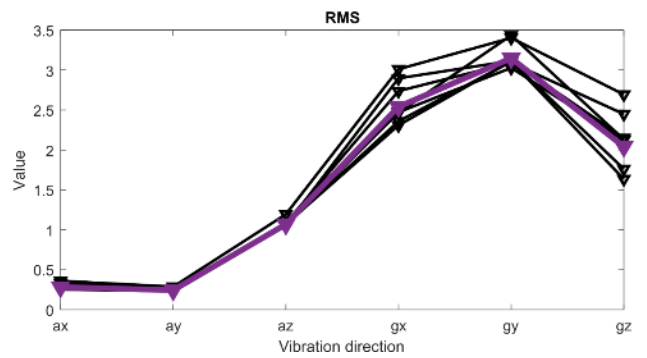
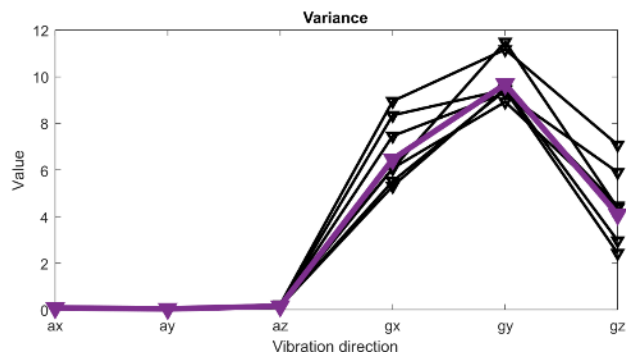
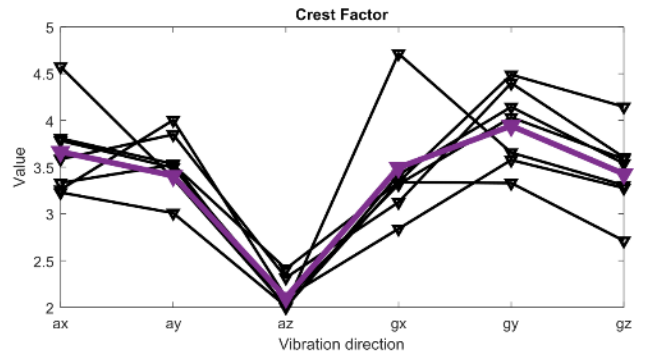
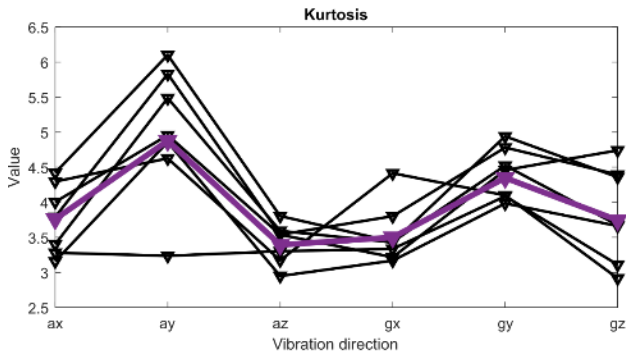


Figure A 8 Sand-scattered rails during braking. Black lines are all the 7 test, blue line is the average.

Annex B. Published papers.

B.1 Frequency Analysis of the Railway Track under Loads Caused by the Hunting Phenomenon

Hurtado-Hurtado, G., Morales-Velazquez, L., Valtierra-Rodríguez, M., Otremba, F., & Jáuregui-Correa, J. C. (2022). Frequency Analysis of the Railway Track under Loads Caused by the Hunting Phenomenon. *Mathematics*, 10(13), 2286.



Article

Frequency Analysis of the Railway Track under Loads Caused by the Hunting Phenomenon

Gerardo Hurtado-Hurtado ¹, Luis Morales-Velazquez ¹, Martín Valtierra-Rodríguez ^{1*}, Frank Otremba ² and Juan C. Jáuregui-Correa ^{3,*}

¹ Faculty of Engineering, Autonomous University of Queretaro, Campus San Juan del Río, San Juan del Río 76807, Mexico; ghurtado09@alumnos.uaq.mx (G.H.-H.); luis.moralesv@uaq.mx (L.M.-V.); martin.valtierra@uaq.mx (M.V.-R.)

² Federal Institute for Materials Research and Testing (BAM), 12489 Berlin, Germany; frank.otremba@bam.de

³ Faculty of Engineering, Autonomous University of Queretaro, Santiago de Queretaro 76010, Mexico

* Correspondence: jc-jauregui@uaq.mx

Abstract: Hunting is a potentially dangerous phenomenon related to the lateral oscillation of the wheels that impacts the rails and causes the wear of the infrastructure's components. Therefore, the analysis and timely detection of hunting can lead to the application of corrective maintenance tasks, reducing damages, and costs and even derailments as a result. In this work, the vibration response of a finite element model of a rail with hunting-induced loads by a single wheel is analyzed in three directions: longitudinal, lateral, and vertical. The contact patch forces are calculated by means of Simpack[®] using the Kalker linear theory and the contact Hertz theory. The system is solved by using the Newmark- β approach. The results of the deflection and vibration analysis, following the proposed methodology, show how the different characteristics of the loads impact the rail.

Keywords: continuous wavelet transform; empirical mode decomposition; finite element method; frequency analysis; hunting phenomenon; mechanical modelling; rail vibrations

MSC: 70J35



Citation: Hurtado-Hurtado, G.; Morales-Velazquez, L.; Valtierra-Rodríguez, M.; Otremba, F.; Jáuregui-Correa, J.C. Frequency Analysis of the Railway Track under Loads Caused by the Hunting Phenomenon. *Mathematics* 2022, 10, 2286. <https://doi.org/10.3390/math10132286>

Academic Editor: Marek Lampart

Received: 20 May 2022

Accepted: 17 June 2022

Published: 30 June 2022

Publisher's Note: MDPI stays neutral with regard to jurisdictional claims in published maps and institutional affiliations.



Copyright: © 2022 by the authors. Licensee MDPI, Basel, Switzerland. This article is an open access article distributed under the terms and conditions of the Creative Commons Attribution (CC BY) license (<https://creativecommons.org/licenses/by/4.0/>).

1. Introduction

Hunting is a wheel lateral oscillation that occurs when the wheelset reaches its critical speed. It is well known that the main factor causing this phenomenon is the semi-conical shape of the threads, as shown in Figure 1. Nonetheless, the conical shape is needed to keep trains on the tracks and able to turn on curves.

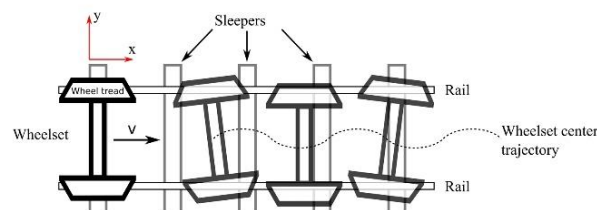


Figure 1. Wheelset hunting.


Hunting limits the stable and safe maximum speed of any railway vehicle. Over the past few decades, numerous authors have made many attempts to understand the

B.2 Railcar Dynamic Response during Braking Maneuvers Based on Frequency Analysis
Hurtado-Hurtado, G., Morales-Velazquez, L., Otremba, F., & Jáuregui-Correa, J. C.
(2023). Railcar Dynamic Response during Braking Maneuvers Based on Frequency
Analysis. *Applied Sciences*, 13(7), 4132.



Article

Railcar Dynamic Response during Braking Maneuvers Based on Frequency Analysis

Gerardo Hurtado-Hurtado ¹, Luis Morales-Velazquez ¹, Frank Otremba ² and Juan C. Jáuregui-Correa ^{3,*} 

¹ Faculty of Engineering, Autonomous University of Queretaro, Campus San Juan del Río, San Juan del Río 76807, Mexico

² Federal Institute for Materials Research and Testing (BAM), 12489 Berlin, Germany

³ Faculty of Engineering, Autonomous University of Queretaro, Santiago de Queretaro 76010, Mexico

* Correspondence: jcjauregui@uaq.mx

Abstract: The dynamic response of a vehicle during braking is influenced by the tangential forces developed at the wheel-rail's contact surface. The friction coefficient affects the load transfer from the wheel's tread to the vehicle. In this work, the vibrations of a scale-down railway vehicle are monitored during braking and their relationship with the friction coefficient between wheel and rail is found out. The vehicle is instrumented with encoders, accelerometers, and is controlled via Bluetooth. The tests are carried out with clean and friction-modified rails. The tangential forces transmitted from the wheel to the railcar's body are visualized in time and frequency using a proposed correlation algorithm based on the outputs of the Continuous Wavelet Transform (CWT). The results demonstrate that tangential forces have a significant impact on railway vehicles under conditions of high friction coefficients and large creep values.

Keywords: railway vibration measurements; vibration signal analysis; wheel-rail tangential forces; railway braking forces; wheel-rail friction coefficient



Citation: Hurtado-Hurtado, G.; Morales-Velazquez, L.; Otremba, F.; Jáuregui-Correa, J.C. Railcar Dynamic Response during Braking Maneuvers Based on Frequency Analysis. *Appl. Sci.* **2023**, *13*, 4132. <https://doi.org/10.3390/app13074132>

Academic Editor: Junhong Park

Received: 20 February 2023

Revised: 22 March 2023

Accepted: 22 March 2023

Published: 24 March 2023



Copyright: © 2023 by the authors. Licensee MDPI, Basel, Switzerland. This article is an open access article distributed under the terms and conditions of the Creative Commons Attribution (CC BY) license (<https://creativecommons.org/licenses/by/4.0/>).

1. Introduction

During braking, tangential forces developed in the wheel-rail contact area have a direct effect on the dynamic response of the railway vehicle. As a result, the vehicle's dynamic response exhibits different frequencies depending on the friction coefficient. Large tangential forces may threaten the stability of the railway vehicles if the braking torque is not applied properly [1], and even damage the train's wheels, engine, and rails, if applied abruptly [2].

If vibrations caused by braking are very strong, they can be transferred to the vehicle's body. Railway vehicle vibrations can cause discomfort to passengers and even cause harmful vibrations in railway structures [3]. Koç [4] addresses this issue by proposing a linear actuator adapted to the secondary suspension to reduce vibrations caused by the train-bridge interaction.

Vibration monitoring is used to find faults in railway components. Accelerometers were installed on the axle-box and bogie by Lee et al. [5] to detect lateral and vertical track irregularities. Tsunashima [6] uses a machine-learning-based algorithm to classify rail failures as either vertical, lateral alignment, or cross-level. Wei et al. [7] installed accelerometers on the vehicle bogies to monitor lateral and vertical vibrations, thereby determining track alignment. Jáuregui et al. [8] used a technique based on empirical mode decomposition (EMD) to find a transfer function, which converts vehicle accelerations into track deformations. Their proposal aims to visualize the evolution of damage in the track and substructures.

The rolling tangential forces that cause vibrations to the vehicle are generated in a relatively small contact area (ellipse-shape) of 1 cm² size [9]. The contact area is separated into traction and sliding regions. The ratio between these two regions determines the

B.3. Method for predicting dynamic loads for a health monitoring system for subway tracks

Jauregui-Correa, J. C., Morales-Velazquez, L., Otremba, F., & Hurtado-Hurtado, G. (2022). Method for predicting dynamic loads for a health monitoring system for subway tracks. *Frontiers in Mechanical Engineering*, 1-16.



OPEN ACCESS

EDITED BY
Shahrul Abdullah,
Universiti Kebangsaan Malaysia,
Malaysia

REVIEWED BY
Rims Janeliukstis,
Riga Technical University, Latvia
Ismail Eser,
Karabük University, Turkey

*CORRESPONDENCE
Juan Carlos Jauregui-Correa,
jc.jauregui@uaq.mx

SPECIALTY SECTION
This article was submitted to Solid and
Structural Mechanics,
a section of the journal
Frontiers in Mechanical Engineering

RECEIVED 19 January 2022
ACCEPTED 24 August 2022
PUBLISHED 14 September 2022

CITATION
Jauregui-Correa JC,
Morales-Velazquez L, Otremba F and
Hurtado-Hurtado G (2022). Method for
predicting dynamic loads for a health
monitoring system for subway tracks.
Front. Mech. Eng. 8:858424.
doi: 10.3389/fmech.2022.858424

COPYRIGHT
© 2022 Jauregui-Correa, Morales-
Velazquez, Otremba and Hurtado-
Hurtado. This is an open-access article
distributed under the terms of the
Creative Commons Attribution License
(CC BY). The use, distribution or
reproduction in other forums is
permitted, provided the original
author(s) and the copyright owner(s) are
credited and that the original
publication in this journal is cited, in
accordance with accepted academic
practice. No use, distribution or
reproduction is permitted which does
not comply with these terms.

Method for predicting dynamic loads for a health monitoring system for subway tracks

Juan Carlos Jauregui-Correa^{1*}, Luis Morales-Velazquez¹,
Frank Otremba² and Gerardo Hurtado-Hurtado¹

¹Autonomous University of Queretaro, Santiago de Queretaro, Mexico, ²Federal Institute for Materials Research and Testing (BAM), Berlin, Germany

This paper presents a method for processing acceleration data registered on a train and determining the health condition of a subway's substructure. The acceleration data was converted into a dynamic deformation by applying a transfer function defined using the Empirical Mode Decomposition Method. The transfer function was constructed using data produced on an experimental rig, and it was scaled to an existing subway system. The equivalent deformation improved the analysis of the dynamic loads that affect the substructure of the subway tracks because it is considered the primary load that acts on the track and substructure. The acceleration data and the estimated deformations were analyzed with the Continuous Wavelet Transform. The equivalent deformation data facilitated the application of a health monitoring system and simplified the development of predictive maintenance programs for the subway or railroad operators. This method better identified cracks in the substructure than using the acceleration data.

KEYWORDS

health monitoring, transfer function, railroad, substructure failures, dynamic loads

Introduction

The railroad substructure absorbs the majority of the dynamic loads. Although there are different ambient dynamic loads (either wind loads or seismic loads), the main load is caused by the train's traffic. There are two types of substructure: on the ground and elevated structures or bridges. The dynamic response of each one is different, and in the case of bridge structures, it depends on the structural design. Recently there have been a few bridge failures, but many of the railroad systems in the world were built a long time ago. Therefore, it is mandatory to predict the bridges' remaining life. Smith (Smith, 2005) described the different fatigue failures in railroads. Although fatigue analysis in railroads is well-known (more than 200 years of research), dramatic accidents still occur. Smith described the various fatigue failures in the wheel-rail interfaces: The failures related to the interface appear in the wheels, the rails, and the rail welds.

The dynamic behavior of the railcar depends on the wheel-rail interfaces. The failures related to the dynamic forces produced by the rotating systems and train velocity appear in the bearings, axles, gearboxes, bogies, suspension, breaks, rail fastenings, track